EVALUATING THE USE OF RECYCLED AND SUSTAINABLE MATERIALS IN SELF-CONSOLIDATING CONCRETE FOR UNDERGROUND INFRASTRUCTURE APPLICATIONS

FINAL PROJECT REPORT

by
Mehran Mazari[1]
Siavash F. Aval[1]
Tonatiuh Rodriguez-Nikl[1]
[1]California State University Los Angeles

Sponsorship
UTC-UTI

For

University Transportation Center for
Underground Transportation Infrastructure
(UTC-UTI)

July 2020

Disclaimer

The contents of this report reflect the views of the authors, who are responsible for the facts and the accuracy of the information presented herein. This document is disseminated in the interest of information exchange. The report is funded, partially or entirely, by a grant from the U.S. Department of Transportation's University Transportation Centers Program. However, the U.S. Government assumes no liability for the contents or use thereof.

1. Report No. UTC-UTI Report 009	2. Government Accession No.	3. Recipient's Catalog No.
4. Title and Subtitle Evaluating the Use of Recycled and Sustainable Materials in Self-Consolidating Concrete for Underground Infrastructure Applications		5. Report Date July 2020 6. Performing Organization Code
7. Author(s) Mehran Mazari (orcid.org/0000-0003-4988-951X) Siavash F. Ava (orcid.org/ 0000-0002-8686-9035) Tonatiuh Rodriguez-Nikl (orcid.org/0000-0001-6227-5083)		8. Performing Organization Report No. UTC-UTI 009
9. Performing Organization Name and Address University Transportation Center for Underground Transportation Infrastructure (UTC-UTI) Tier 1 University Transportation Center Colorado School of Mines Coolbaugh 308, 1012 14th St., Golden, CO 80401		10. Work Unit No. (TRAIS) 11. Contract or Grant No. 69A355174711
12. Sponsoring Agency Name and Address United States of America Department of Transportation Research and Innovative Technology Administration		13. Type of Report and Period Covered Final Project Report 14. Sponsoring Agency Code
15. Supplementary Notes Report uploaded at https://zenodo.org/communities/utc-uti		
16. Abstract Self-Consolidating Concrete (SCC), also known as self-compacting concrete, is a type of hydraulic cement concrete that easily forms around the reinforcement without segregation. The use of recycled fibers in the SCC mix, affect the compressive strength, tensile strength and crack initiation and propagation. The main objective of this study was to investigate the application of novel-fibers reinforcement SCC in transportation infrastructures. The improved mechanical properties of the modified SCCs make them alternative solutions for precast sections for transportation infrastructure applications compared to the conventional concrete. In the first part of this research, the effect of six fibers on SCC properties was investigated and in the second part the hybrid effect of fibers was assessed. According to the results, each recycled fibers has the capability to improve targeted properties whereas the binary combination of fibers has the potential to improve wider range of properties.		
17. Key Words Self-Compacting Concrete, Recycled Fibers, Underground Transportation Infrastructure		18. Distribution Statement No restrictions.

19. Security Classification (of this report)	20. Security Classification (of this page)	21. No of Pages	22. Price
Unclassified	Unclassified	115	NA

Table of Contents

List of Figures

List of Tables

List of Abbreviations

AA: Alkali-Activated
AASHTO: American Association of State Highway and Transportation Officials
AEA: Air-Entraining Admixture
ACM: Alternative Cementitious Materials
ASTM: American Society for Testing Materials
CAC: Calcium Aluminate Cement
CSA: Calcium Sulfoaluminate Belite
CSAB: Calcium Sulfoaluminate-Belite
CSB: Calcium Sulfoaluminate Belite
CVC: Conventionally Vibrated Concrete
CHPP: Center of Highway Pavement Preservation
FA: Fly Ash
GGBS: Ground Granulated Blast-Furnace Slag
HRWRA: High Range Water Reducing Admixture
MDOT: Michigan Department of Transportation
MPC: Magnesium Phosphate Cement
MRWRA: Mid-Range Water Reducing Admixture
OPC: Ordinary Portland Cement
PVC: Polyvinyl Chloride
SCC: Self-Consolidating Concrete
SCM: Supplementary Cementitious Materials
SCRC: Self-Compacting Rubberized Concrete
SEM: Scanning Electron Microscope
SP: Superplasticizers
VMA: Viscosity Modifying Admixture

EXECUTIVE SUMMARY

The main objectives of this research project are the following items:

- Improving fresh and hardened properties of self-consolidating concrete,
- Evaluating the use of recycled fibers to improve the properties of self-consolidating concrete,
- Investigating the use of sustainable materials to reduce the amount of cementitious materials in self-consolidating concrete, and
- Evaluating the crack initiation and propagation related to properties of the self-consolidating concrete

Chapter 1 contains the literature review highlighting the most relevant and pertinent findings in the literature.

This study is consisted of three main phases. Phase I includes a comprehensive information search and review of literature regarding the properties of SCC, materials and its applications.

Chapter 2 explains experimental and laboratory test methodology for fresh, hardened and durability assessments and mixture design.

Chapter 3 consists of primary experimental and laboratory investigations on six different fibers. These include:

- Evaluating the fresh properties of selected SCC mixes to evaluate workability, flow ability and passing ability
- Measuring the hardened properties including compressive strength, split tensile strength and drying shrinkage
- Performing durability tests including water absorption and bulk electrical resistivity

Chapter 4 investigates the individual and hybrid effect of selected recycled fibers.

Chapter 5 contains a list of conclusions and findings from this study and recommendation for future directions.

CHAPTER 1 - INTRODUCTION

1.1 Background

Self-consolidating concrete (SCC) or self-compacting concrete is a concrete mix and is a specially proportioned hydraulic cement concrete which has a low yield stress, high deformability, good segregation resistance, and moderate viscosity. Use of this type of concrete in precast, pre-stressed bridge elements has increased in recent years because of the increased rate of production and safety, reduced labor need, and lower noise levels at manufacturing plants. SCC was conceptualized in 1986 by Prof. Okamura at Ouchi university, Japan, at a time when skilled labor was in limited supply, causing difficulties in concrete related industries. SCC can be used for casting heavily reinforced sections, places where there can be no access to vibrators for compaction and in complex shapes of formwork, which may otherwise be impossible to cast, giving a far superior surface than conventional concrete.

Self-consolidating concrete has been used in a variety of mass construction applications and structural implementation such as tunnels, dams, bridge decks and other such projects. Many studies have been conducted around the world to evaluate the mechanical properties of SCC that are of interest for a variety of reasons. The concern is more so with the application in transportation infrastructures, which require the workability and passing ability of concrete without in-situ vibration. There is also an emphasis on the study of fiber reinforcement in these mixes and the effect on fresh and hardened properties of SCC. Design of an SCC mix is chosen based on either powder-type, viscosity modifying admixture-type, or a mixture of the two types depending on structural and constructional conditions, and availability of materials (Ouchi, 2003). SCC mixes have undergone several alterations and as shown in the literature can have discrepancies between the origin of their applications, specifically in Japan, Europe and the United States where arguably the most amount of research on this subject has been conducted.

An SCC mix is typically characterized by the conventional ingredients that make up regular concrete. The main difference is in the inclusion of admixtures such as viscosity modifying admixture (VMA), and High Range Water Reducing (HRWR) agent as well as superplasticizers (SP). Aside from these, minor differences in aggregates used such as crushed limestone, gravel, sand and other types of materials, coupled with alterations in proportioning, had several varying effects on the properties of SCC. Likewise, some of the studies in the literature evaluated the effects of air entrainment on these mixes, in one study coupling them with the admixtures to display these effects (Khayat and Roussel, 1999).

Normally for SCC with high water-powder ratio and/or low powder content, VMA is added to improve mix stability by enhancing rheological properties and reducing segregation. HRWR is an agent used to reduce water content and produce better flow ability. The properties the agent typically affects are prolonging setting time, slump and air entrainment depending on the dosage used. Such an agent, when used in conjunction with VMA for example, can achieve greater workability for SCC. There are different types of HRWR to address their desired performance goals and correct any shortcomings of the designed SCC. Superplasticizers of poly-carboxylic ether type were also utilized to achieve workability targets; such was used to complement VMA, HRWR or a combination of all. In addition to these three typical chemical admixtures used, air-

entraining admixture (AEA), while not being widely implemented, also serves a role in some SCC mix designs mostly for increasing freezing resistance of the concrete, increasing cohesion, and improving compaction in mixes with lower workability. Table 1.2.1 summarizes the application of different additives in SCC mixes across the literature.

Geopolymer is another specialized type of SCC, which is characterized by alkali-activation to form a binder, which holds the aggregates and other cementitious materials together. Geopolymer SCC has been mostly found to have greater than and equal strength compared to Portland Cement concrete as well as better Sulphate, fire and acid resistance to name a few properties. Such a concrete has been of interest to become a possible stronger alternative to conventional concrete types. The concrete was also reinforced with rebar and fibers in differing publications with related strengths and property changes. The main difference between the Geopolymer and normal concrete would be the need for an alkaline activator solution made up of varying ratios of certain chemicals. This activator reacts with the other component materials to create the paste, which binds the aggregates together.

Both types of concrete were tested in a few rheological and mechanical tests to determine characteristics such as flow ability, setting, cohesion, aggregate segregation, and compressive strength. These tests are divided into the categories of fresh state and hardened state properties. Along with this, attention was paid to aspects such as water-cement or solid ratios across the literature.

1.2 SCC Fresh and Hardened Properties

Aside from the conventional slump flow test, there are a set of specialized tests to evaluate the filling ability, workability and passing ability of SCC. For the slump flow test, many times shown as T_50 or some other variation in the literature, from the initial point of release of the cone to when the concrete ceases to spread outward onto the floor or testing surface the time is measured and recorded (ASTM 1611). More specifically, the J-Ring slump is a rigid ring with 300 mm in diameter and supported 100 mm above the floor or surface by 16 mm wide reinforcement rods. The rods are spaced apart to allow the SCC poured in to pass through and enable the operator to record both change in diameter and height. The change in diameter is in comparison to the results obtained from the J-Ring test (ASTM C 1621) and the slump diameter test. This comparison shows how restrictive the passage of SCC is when put through the rods as opposed to the slump diameter test, which has no objects that congest the flow. The results also display how viscous the SCC is and if aggregate segregation occurs. The change in height comes from measuring the height of the fresh concrete inside of the ring and outside of it. The higher the difference, the lower the passing ability, as the test clearly shows the inability of the concrete to pass through the rods and out of the inner ring (Figure 1.2.1 c).

The column segregation test (ASTM C 1610), gives an estimate of the segregation and resistance exhibited by the mix. With a 203.2 mm diameter, the column is a PVC pipe split up into three sections that are initially clamped together. SCC concrete is poured into the pipe and left for 15 minutes, afterward, which the sections are individually removed, and the concrete washed over a sieve retaining the coarse aggregates. These aggregates are dried and measured by mass for each

section, from which the coefficient of variation is calculated, and the segregation resistance is estimated (Figure 1.2.1 d).

Table 1.2.1 - Admixture and Air Entrainment Characteristics Across the Literature

Author of Paper	Air Entrainment (%)	AEA[1]	VMA[2]	HRWR[3]	SP[4]
Abbasi, et al. (1999)	No	No	Yes	Yes	No
Khayat & Roussel (1999)	5.1, 5.7, 7.1, 7.9 after 60 min 4.8, 4.9, 5.8, 5.9	Yes	Yes	Yes	Yes
Holschemacher & Klug (2002)	>5%	Yes	No	No	Yes
Ouchi et al. (2003)	4.5-7%	No	Yes	Yes	Yes
C. I. Goodier (2003)	No	No	Yes	No	Yes
Corinaldesi & Moriconi (2003)	2.9	No	Yes	No	Yes
P.L. Domone (2005)	No	Yes	No	No	No
Domone (2006)	No	No	No	No	Yes
Ferrara et al. (2007)	No	No	No	No	Yes
Rangan (2008)	No	No	No	Yes	Yes
Pintado & Barragan (2009)	No	No	Yes	No	Yes
Guneyisi (2009)	No	No	Yes	No	Yes
Bamonte & Gambarova (2012)	No	No	No	No	Yes
Khaloo et al. (2013)	No	No	Yes	No	Yes
Singh et al. (2015)	No	No	No	No	Yes
Ramujee & PothaRaju (2016)	No	No	No	No	Yes
Hardjito et al. (2017)	No	No	No	Yes	No

[1]AEA – air entrainment admixture, [2]VMA – viscosity modifying admixture, [3]HRWR – high-range water reducing agent, [4]SP – superplasticizer

The L-box fill test also works to measure passing and filling ability (Figure 1.2.1 b). The equipment is in the shape of an L with a hallow vertical portion that connects to a hallow horizontal portion with a gate opening to allow the fresh concrete to pass through reinforcement bars similar

to those described in the J-Ring test. The concrete, initially poured into the vertical portion, is released and flows through the bars at which point it is timed for when it reaches 200 mm, 400 mm and once it halts motion. From this point, the height at which the concrete stops flowing into the horizontal and that which is left inside the vertical are recorded to produce the blocking ratio. Similarly, the U-type fill test has equipment that is in the shape of a U and has fresh concrete poured into one side of the apparatus. A gate located symmetrically in the middle of the curved bottom portion, which is released and allows the concrete to flow through bars on the other side of the gate. From the point of release, the concrete is timed until it stops flowing into the other side. Heights on either side are taken and the ratio is estimated (European Guidelines 2005). Both tests can also be used to measure segregation in a similar manner to the J-Ring test.

The V-funnel test (Figure 1.2.1 a) is a system, which has a V-shaped funnel that has a small opening at the bottom and is used to evaluate SCC with max aggregate size of 20 mm. The funnel is filled with 12 liters of the fresh concrete and is timed from the point it is released and flows out of the funnel. It is then refilled, this time with the concrete being allowed to set for 5 minutes and timed in the same manner. The comparison of the times displays whether there is segregation in the mix as well as paste viscosity (European Guidelines 2005).

Hardened properties are tested after the fresh concrete is compacted and cast into cylinders, prisms or some other standard-specific geometric shape for later testing. Curing for SCC cylinders undergoes the similar procedure described for conventional vibrated concrete (CVC) (Morcous, 2016). It is therefore characterized by placement into plastic or similar material cylinders that can assure there is no water evaporation from the fresh concrete after finishing. These are stored afterward and allowed to set for either 24 +/- 8 hours, 20 +/- 4 hours for prolonged setting mixes or determined by ASTM C403/C403M. After this setting and subsequent hardening, they are removed and cured at 23 +/- 2 degrees Celsius either in a misting room, water tanks or some other sort of system to maintain surface moisture of the specimens. The first 48 hours they are to be cured in a non-vibrating environment and depending on the specifications or criteria of the experimenter left until they are to be tested.

The hardened properties that were examined in the literature range from compressive strength values to flexural and splitting tensile strength to modulus of elasticity or a combination of all these. The compression strength results were of particular interest and taken at 28 days. However, it could also be seen that some authors took results at even wider ranges, for example at 7, 14, 21, 56 and even 91 days (Ouchi 2003). The compression test is comprised of loading cylinders, blocks or other concrete sample shapes into a machine that with or without proper capping procedures presses vertically into the specimen loading it gradually. The loading continues until the specimen fails and results are recorded. The splitting tensile strength test also works in a similar system with primarily a cylinder being loaded sideways into a metal mold in the shape of a triangle with a base plate and a long rectangular piece of plywood or other material spanning the length of the specimen. The rectangular portion compresses into the cylinder until failure in the form or cracking or the specimen being split in half. The studies in the literature gave some correlation between mix compositions to the recorded properties of the SCC specimens and observed some trends with proportioning and/or inclusion of additional materials such as admixtures or fibers.

Figure 2 summarizes the properties of SCCs across the literature. Water-Cement ratio is one of main factors that affect the compressive strength of the SCC. Reviewing the information across the literature showed that a ratio of 0.4 is more common in the SCC mix design. A few other studies showed that the ratio of 0.5 or in some cases 0.2 was used for the mix proportioning. The distribution 28-day compressive strength of SCC samples also showed that majority of the studies in the literature reported a compressive strength of 40 MPa or more. However, it seems that adding fibers to the mix and in some cases, using recycled non-cementitious materials (i.e. fly ash or blast furnace slag) improved the hardened properties in terms of compressive strength.

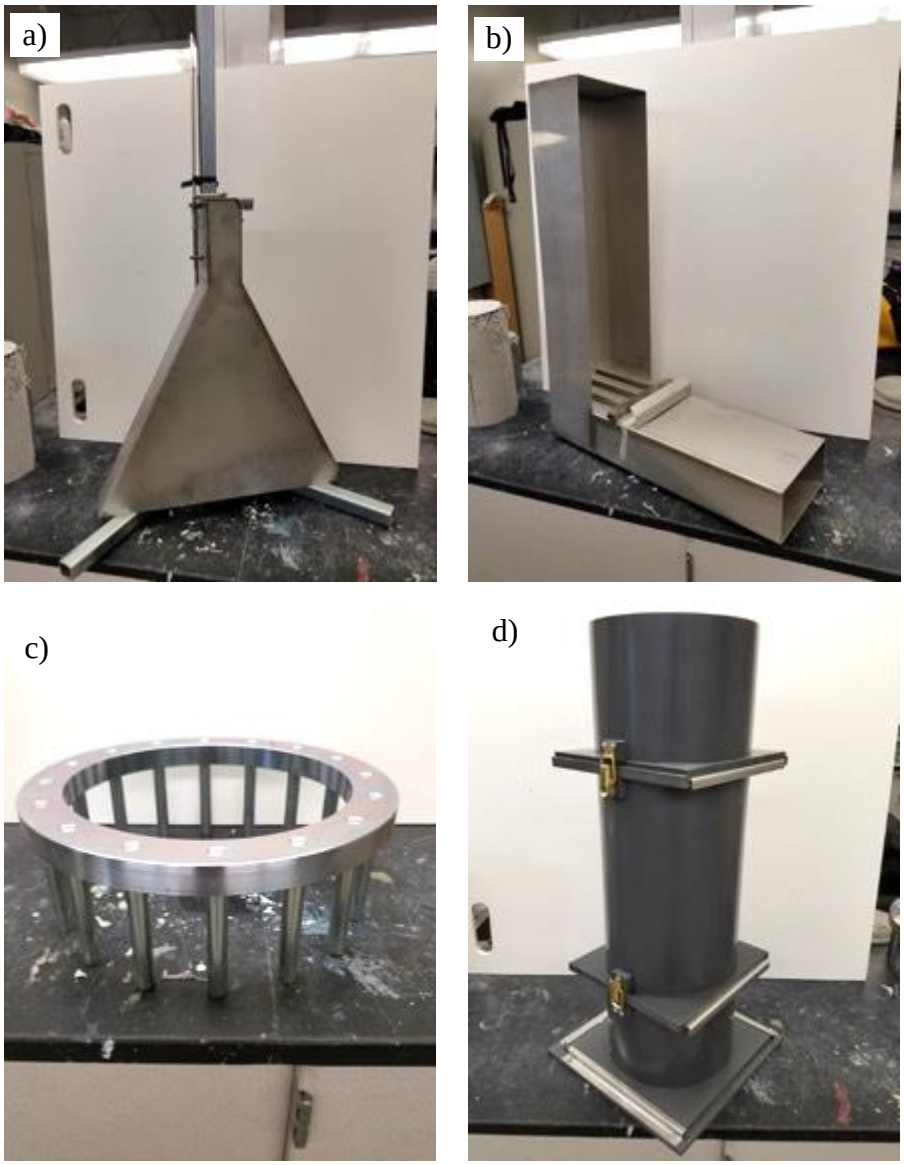

Figure 1.2.1 Tests for estimation of SCC fresh properties, a) V-Funnel, b) L-Box, c) J-Ring, and d) Segregation Column

1.3 Application of SCC and Fiber-Reinforced SCC in Transportation Infrastructures

Fiber-reinforced SCCs have been evaluated in a number of studies in the literature. It also has been implemented and evaluated in some transportation infrastructure applications. The following sections summarize the relevant studies in the literature.

Boulekbache et al. (2010) investigated in the flow ability of fiber-reinforced concrete and the effect of fibers on mechanical properties of SCC. In general, adding fibers to the mix decreases the drying shrinkage and propagation of micro cracks while enhancing fatigue and impact resistance. They used a fluid model to simulate and estimate the orientation and distribution of fibers in the mix. However, based on the experimental work in that study, the addition of fibers slightly decreased the compressive strength of the SCC mixes. On the other hand, the ductility and flexural strength were improved in the fiber-reinforced SCC. Also, the fiber orientation seemed to impact the flexural capacity in terms of initiation and propagation of micro cracks.

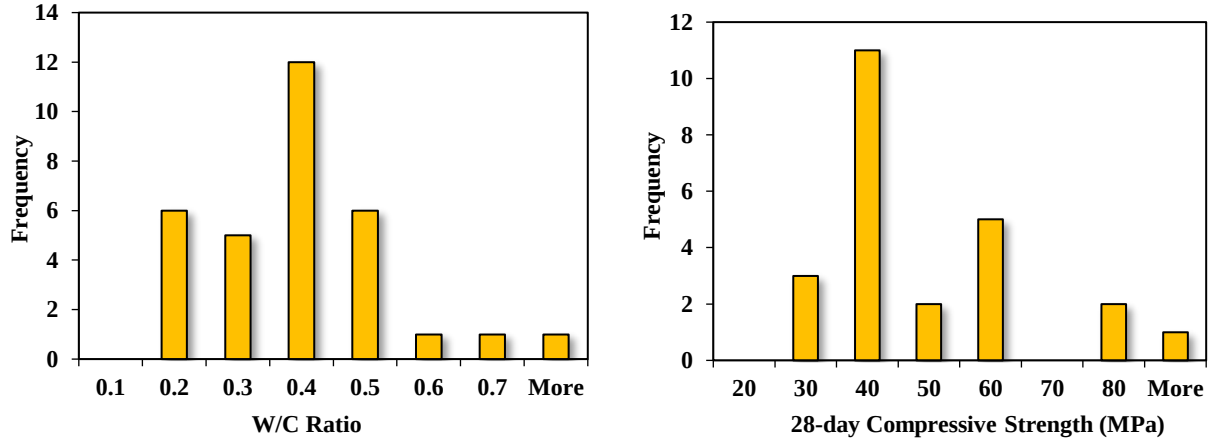

Figure 1.3.1 – Distribution of a) W/C ratio and b) 28-day compressive strength for SCC mixes across the literature

Khaloo et al. (2014) studied the performance of fiber-reinforced SCC using steel fibers. They have performed a series of laboratory tests to evaluate the fresh and hardened properties of SCC mixes containing different dosage of steel fibers. The addition of 2% fiber by volume of the mix, decreased the workability and passing ability through the J-ring rebars. It also slightly decreased the compressive strength by about 2% compared to the SCC mixes without fibers. However, both split tensile strength and flexural strength of the fiber-reinforced SCC were increased compared to the plain samples. The flexural toughness also increased by increasing the volume of fibers in the SCC mix.

Figure 1.3.2 compares the finished surface condition of two tunnel lining elements constructed with conventional concrete (Figure 1.3.2 a) and self-compacting concrete (Figure 1.3.2 b) as documented in Hulin et al. (2011). Two types of SCC mixes using polypropylene and steel fibers were designed and proportioned for this study. The higher workability, passing ability and flowability of the SCC mixes were beneficial to produce a smoother surface for liner segments while achieving a high compressive strength (Hulin et al. 2011).

Schumacher (2006) studied the rotation capacity of tunnel liners constructed with steel fiber-reinforced SCC. That study found that using SCC prevents localization of cracks in structural elements. The addition of steel fibers increased the confinement capacity and tension stiffening of

the pre-cast liner elements. For bending members with steel fibers in the mix, the load bearing capacity observed to be higher compared to conventional concrete.

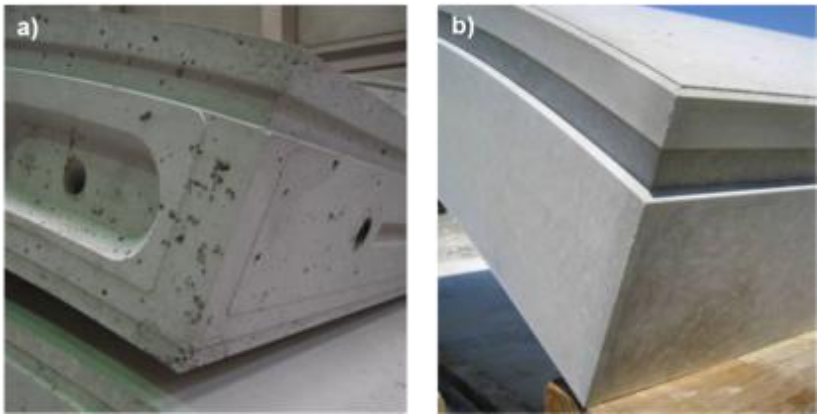

Figure 1.3.2 – Comparison of finished concrete surface for a tunnel liner element for a) conventional concrete, and b) self-compacting concrete (Hulin et al. 2011)

1.4 Materials in SCC

The basic components for the mix composition of SCC are similar to those used in conventional concrete. SCC mixtures generally have some combination of lower total aggregate content, greater amount of fine aggregate relative to coarse aggregate, and smaller maximum aggregate size. SCC can be produced with a wide range of aggregate sources; the optimization of aggregate characteristics can result in improved flow properties and reduced demand for cementitious materials, water, and chemical admixtures. The key characteristics include but are not limited to shape, angularity, texture, grading and micro fines characteristics. In SCC a higher proportion of ultrafine materials and the incorporation of chemical admixtures and effective superplasticizer are necessary to meet the properties of SCC. Different types of powders / filler materials are used such as fly ash, limestone powder, blast furnace slag, silica fume, and quartzite powder.

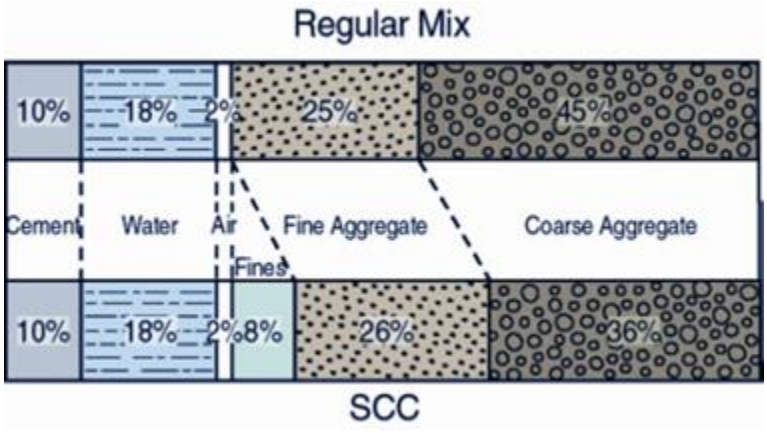

Figure 1.4.1 – Difference between CVC and SCC in their mix proportions and aggregates

1.4.1 Aggregates

Coarse aggregates

In SCC the most commonly used size of aggregates is in range of 10 to 20 mm. Grading curve for the coarse aggregates is provided by the equation from Funk and Dinger (1994). P(d) is the cumulative passing fraction at a sieve with opening maximum aggregate diameter is dmax. dmin = 0.075 mm q = 0.25 (Brouwers and Radix, 1997) q = 0.50 (Ferrara, 2007) for Fiber-Reinforced (FR) SCC.

Fine aggregates

resists segregation

sand percentage is inversely proportional to the density of fresh concrete, higher air content, and less compressive strength, suggested percentage was 50% or more (Sugár and Takács, 2013)
SU et al., (2001) suggested sand percentage 50% - 57%

Fines (filler)

The highest packing density generally will take place when the fines content is about 15% (Kwan et al., 2014). A study done by Moutassem (2016) tries to develop an analytical model for determining maximum packing density in concrete. Packing density is an important indicator of flowing ability (rheology) and segregation resistance of fresh concrete. For hardened concrete, a higher packing density improves concrete durability. The study assesses nine packing density models for predicting maximum packing density of aggregates while considering three compaction methods: loose, rodding, and vibration. Maximizing packing density will improve workability and it is also more economical since less binder material is required. Minimizing the porosity of the dry mix by, minimizes the amount of binder needed. This is done by reducing the free water content and maximizing solids.

The slump cone test can be used to maximize the aggregate packing density. This test includes filling an inverted cone to see how much of each type of aggregate can fill the cone. The total mass added is then used to calculate the individual mass & volume of each type of aggregate. These values are plugged into three equations to find maximum packing density and void content.

1.4.2 Binders

Cement

SCC often has higher cementitious materials content than conventionally placed concrete in order to achieve adequate flowability. The potential negative consequences of high cementitious materials content include higher cost, higher heat of hydration, and increased susceptibility to shrinkage. All standard types of Portland cements are generally acceptable for SCC. Admixture performance can be strongly dependent on cement characteristics. All Portland cements that conform to the requirements of AASHTO M 85 can be used for the production of SCC for cast in place bridge components. Types IP (Portland - Pozzolan cement), IS (Portland blast furnace slag

cement), and PLC (Portland-limestone cement) can be used. When types I, II or III cements are used, replacements with supplementary cementitious materials (SCMs) and fillers are recommended as they enhance the fresh and hardened SCC properties.

Alternative Cementitious Materials (ACM)

Research was compiled from Georgia Institute of Technology where they studied the comprehensive and systematic investigation of novel alternative cementitious materials (ACMs) for applications in transportation infrastructure. The ACMs that were studied in the report were calcium aluminate cement (CAC), calcium sulfoaluminate (CSA), calcium sulfoaluminate belite (CSB or CSAB), magnesium phosphate cement (MPC), and alkali-activated (AA), and carbonate-binder systems which all bring advantages over the traditional portland cement. Some of the advantages are the reduction of embodied energy, greenhouse gases and even performance enhancement.

Concrete is one of the most used constructions materials which also accounts for 4.8 percent of global anthropogenic carbon dioxide emissions. When cement is manufactured, it results in 830 kg of carbon dioxide per metric ton of clinker. The table below shows the quantity of carbon dioxide that can be reduced with the use of ACM binders. A big problem in transportation infrastructure is the ongoing construction such as when you build a single bridge for 100 years it will produce less carbon dioxide instead of rebuilding the bridge with a 50-year life span.

Table 1.4.1 – Environmental Impact of ACMs

Binder System	Grams of $C0_2$ Per Gram of Cement	Percent of CO_2 Using OPC
OPC	0.55	100%
CSA	0.28	51%
CSAB	0.46	84%
CAC	0.29	53%
MPC	0.30	55%
AA	Emissions result from manufacture of alkali solutions and transportation only. Precursor materials were assumed to contribute no CO_2 as they are byproducts of other industries	44-64%

In the table above basic ACM information is provided which is used in different states around the United States.

Site 1: Dublin, GA where there is full-depth chemically activated binder concrete which were placed originally in 2008 and remained in service until 2013 which were in great shape with minimal cracking, and no evidence indicated salt scaling or delamination.

Site 2: Los Angeles, CA where Caltrans has used rapid setting AM binders since the 1990s. The first area investigated was at the 60W to the 71S which was constructed in 1997 being an ACM with 85% CSA and 15% Portland cement. When observing this area, the pavement was in very good condition with some small spalls noted at the joints and some evidence of surface abrasion.

The 2nd area investigated was 60E to the 71N where it was constructed in 1991 with a 100% CSA binder which the pavement was in great condition. The 3rd location was at the interstate 10 where it is CSA binder that is present that was placed in 1999 and this site did show significant more damage than the other sites in Los angles. There was also some cracking and mid panel separation. The 4th area was constructed in 2012 between the SR5 and I-605 where 100% CSA binder was used at this site there was some spalling at the joints, extensive longitudinal cracking, and corner cracking in several areas.
Site 3: Dalton Highway, AK in 1991 the Alaska Dot took on a major project to rehab 18 bridges in which MPC was used to facilitate rapid deck replacement. After more than 20 years of service it was seen to be some cracking in the joins due to torsional loading from bridge loading.
Site 4: Interstate 90/ I-94 N, Chicago, IL CAC concrete was used in 2009 to replace pavements near downtown Chicago where the pavement has been holding up well.
Site 5: Treat Island, ME there has been research going on at the U.S. Army Engineer research and development center where they have been testing beams on a pier made of a fly-ash based geopolymer a slag-based geopolymer, and a CSA cement. The beams appeared to show deterioration, scaling, cracking, and expansion. While the ACM samples showed no signs of the such.

The research showed that there indeed is a growing interest in the use of ACMs for large transportation infrastructure construction in the United States in which mainly CAC, CSA, and AA products have been used. ACMs were mainly to be used in large urban areas where there is a need for transportation and where there needs to be rapid setting and high early strength of these materials contributed to minimal road closure time. The most common use of MPC is on small road and joint constructed. There will be further testing in CSA cements which one is a blend of CA and Portland cement while the other is a belite cement, as well as two AA cements.

Table 1.4.2 – Properties of Different ACMs

Literature Review Topic	CAC	CSA	CSAB	MPC	AA	Carbonate Systems
Water to Cement Ratio	0.30-0.40	0.20-0.70	0.40-0.70	0.10-0.52	0.28-1.10	n/a
Comprehensive strengths (lbs/in2)	3000-4200 @ 3 hrs 6500-7900 @ 28 days w/ 0.38 w/c	87-3800 @ 3 hrs	1200 @ 28 days (for 0.8 w/c) 5000 @ 28 days	2900-7300 @ 3 hrs	2000 @ 3 hrs 10000-20000 @ 28 days	9000 @ 24 hrs
Time to initial set at 23°c with no admixtures	2-6hrs	8-22 min	10-15 min	9 min	35 min	Only available as precast conc

Supplementary Cementitious Materials (SCM)

High-performance self-consolidating concrete could be developed using binary, ternary, or quaternary binders with up to 70% of cement replaced by fly ash, slag, and/or silica fume (El-Chabib and Syed, 2013). 70% slag and 30% cement exhibit better fresh performance as well as higher early compressive strength compared to SCC made with only cement. Fly ash enhances the workability and the late compressive strength. Up to 10% silica fume in the ternary and quaternary blends enhance the compressive strength of the SCC but reduce its workability. Adding high contents of SCM to SCC in general, reduces permeability as well as unrestrained shrinkage.

1.4.3 Pozzolanic Materials (FA and GGBS)

Fly Ash (FA) – Class C and Class F

Khatib (2008) – influence of Fly Ash on compressive strength, absorption and shrinkage of SCC. Using high percentage of FA up to 60% could produce SCC with strength as high as 40 N/mm2. Absorption of the SCC increase with the increase in FA content. Increasing the amount of FA in SCC reduces the drying shrinkage.

Ground Granulated Blast-Furnace Slag (GGBFS)

Slag typically replaces cement in concrete in order to improve its sulfate resistance and workability. Concrete containing GGBS develops higher strength over a longer period, leading to reduced permeability and better durability (DMI, 2017). SCC containing GGBFS exhibited higher drying shrinkage than SCC containing Class F fly ash (Morcous, 2016). Mixtures with GGBFS exhibited the highest surface resistivity (low penetrability) compared to conventionally vibrated concrete mixtures (Morcous, 2016). Morcous (2016) also found that SCC mixtures with crushed limestone aggregate and GGBFS required a higher dosage of HRWRA than those with natural gravel aggregate and fly ash to achieve the same workability targets. GGBFS shall meet the requirements of AASHTO M 302.

1.4.4 Fibers in SCC

In the world of rapid urbanization, the demand for natural construction materials is increasing day by day which has created a necessity for alternative construction materials. Reusing of materials is a conceivable method for fulfilling the intense lack of materials. Significant work has been done in the range of self-compacting concrete by halfway substitution of coarse aggregates (CA) with recycled coarse aggregates (RCA) obtained from construction and demolition debris. Recycled aggregates were obtained from a demolished residential building in the adjacent locality, were treated as construction waste, and were crushed to obtain suitable sizes for being used in SCC. Fibers were added in the ratio of 0.5%, 0.75%, and 1%, respectively. Crushed red brick is also used from broken bricks in SCC. Some other examples of used recycled aggregates are recycled steel fibers and recycled carbon fiber.

The addition of steel fibers resulted in increase in the flexural strength and split tensile strength. It was studied that the addition of 30% brick bats and 1% steel fiber yielded a compressive strength of 30.11 N/mm² and the corresponding mixture proportions were considered as the ideal mix proportion. Moreover, the addition of steel fibers reduced the crack width considerably. Also it was observed that due to adequate curing the problem of cracks due to shrinkage was totally eliminated. It was observed that all the constituent materials were spread uniformly in the concrete

matrix including the steel fibers. At optimum content of steel fibers, the compressive strength for the RSCC mixes with steel fibers; improved by 11.3% and 31.8% for the mixes with crushed ceramic and crushed red brick, respectively with respect to control mix. Also, the tensile strength and the flexural strength for the mixes were improved. The recycled aggregates show higher water absorption compared with conventional normal aggregates and have low specific gravity. It is observed that in 28-day test SCC achieves required compression strength at 30% replacement with recycled aggregates.

1.4.5 Fiber Types

Fiber types used in concrete are steel, glass, synthetic, and natural fibers. Steel fibers are the most commonly used fiber in concrete. It is manufactured in many different shapes and sizes. It can be used to improve the flexural strength, but its disadvantage is that it can rust if exposed on the surface of the concrete and reduces workability of fresh concrete. The second type of fiber is glass fiber. Its advantages are that it is an insulator, alkali resistant, and can help reinforce concrete. Synthetic fibers can be developed specifically for the concrete used in the project. They are more durable, but need to be greatly researched. Carbon, nylon, polypropylene, polyester, and polyethylene are common types of synthetic fibers. Natural fibers can be jute, bamboo, coconut, etc. They do not need a lot of energy to extract, but they are not resistant to alkaline.

Manufactured Fibers

Fibers can be used to reinforce concrete by improving its mechanical properties such as strength, durability, and ductility. These properties are valuable since it may prevent cracking and allow for a lighter concrete design. Manufactured fibers used in concrete can be made from plastic, carbon, glass, steel, natural, synthetic, and recycled materials. The type of manufactured fiber selected in the concrete depends on what properties are more valuable in the design. For example, fiber reinforced concrete used for fireproofing may want to contain polypropylene instead of steel fibers because polypropylene is more chemically inert. Manufactured fibers may come in different sizes, lengths, and shapes, which have their own unique advantages. Each type of fiber will have recommended batching percentages in the concrete design. This is to prevent the fibers from clumping together, uneven distribution, segregation, or decreasing the workability of the fresh concrete mix.

Nylo-mono fibers

Nylo-mono fibers is 100% virgin nylon fibrous monofilament intended to reduce the formation of shrinkage cracks prior to initial set and to reduce settlement shrinkage. They are Non-corrosive, chemically inert, and resistant to alkali attack. Typically, the characteristics of these fibers are lower than the Polyvinyl alcohol and steel fiber. (Banyhussan, 2016)

Recycled Fibers

The recycled fibers will be compared to manufactured fibers to see if they could be a plausible alternative in the future. Recycled carbon fibers, recycled plastics, recycled titer textiles, and recycled tire steel fibers are some example of recycled fibers.

Another type of recycled fibers can be made from rubber tires. These fibers have great potential in more versatile SCC applications since the rubber may increase the toughness and durability of concrete. According to Bignozzi (2006), a self-compacting rubberized concrete (SCRC) may require slightly higher amount of superplasticizer than SCC to reach self-compacting properties. Compressive strength and stiffness decrease with increasing amount of rubber phase in the mix. Significant concrete deformability before failure and capability to withstand post-failure loads with some further deformations are exhibited by SCRC due to the tire rubber waste presence. significant amount of rubber phase negatively affect porosity in comparison with that of ordinary SCC.

Steel Fibers

Adding fibers to the concrete mix increases the splitting tensile strength. The addition of steel fiber volume fraction of 0.5% to 2% resulted in an increase of the flexural strength from 4.1% to 46% (Khaloo, 2014). Similar results were shown for beam samples, where steel fiber volume fractions of 0%, 0.5%, 1%, and 2% resulted in higher maximum bending stress by 22.6%, 24.6%, 21%, 26.8%, and 15.5%, respectively (Khaloo, 2014). Based on Khaloo's research, a 2%. fiber volume fraction is recommended to optimize the ductility of concrete. Steel fibers as a secondary reinforcement for concrete are also sometimes manufactured in a wavy/crimped texture. This texture helps the steel fibers anchor into the concrete. Another thing to consider is that the addition of textured steel fibers will require different spacing compared to straight steel fibers. As a result, the workability, tensile strength, and bending strength will vary.

Carbon Fibers

Carbon fibers can be used in concrete. They have a higher flexural strength and stiffness compared to steel. Carbon fibers used in concrete are coated with resin to prevent corrosion and to help the fibers bond to concrete. They are a lightweight alternative to steel fibers. A lower volume percent of carbon fiber in concrete is shown to have a lower compressive strength, but a higher impact toughness and compressive toughness compared to steel fibers according to a research by Song (2016). Carbon fibers may be preferred over glass fibers since they improve the compressive strength but may be more expensive.

Carbon fibers can improve flexural and tensile strength and control drying shrinkage of cement based composite materials. (Akihama, Suenaga, & Banno, 1986; Chen & Chung, 1993; Chung, 2000; Park, Lee, & Lim, 1991; Toutanji, El-Korchi, & Katz, 1994). Hossain and Awal (2011) investigated the effect of carbon fibers on composite cement mortar. Their mixture contained 0.5, 1.0 and 1.5% carbon fibers with the length of 3 and 6 mm. According to the test results, using combination of both sizes (hybrid fibers) resulted in superior bearing capacity in deflection and higher elastic modulus.

Graham et al. (2013) studied the effect of micro and meso carbon fibers on the composite cement mortar. Noting here that the average meso length was 6.31 mm, they concluded that the higher aspect ratio will result in less workability and higher porosity. However, on the hardened properties investigations, the macro fibers showed higher tensile strength. Therefore, they recommended the idea of using hybrid fibers for improvement of both rheology and hardened properties.

Later, in a paper from Shu et al. (2015), 2% and 4% carbon fibers with the length category of micro, macro and combination of both were used to make composite Portland cement mortars. The result indicated that first, the mixtures with micro fibers had lower air content compared to the macro fibers. Second, the incorporation of micro fibers in hybrid mixture assisted the dispersion of the macro fibers and finally, the pre-peak load tensile performance and fracture resistance was the highest in mixtures containing hybrid fibers.

Li et al. (2015) worked on the hybrid effect of 0.1, 0.2 and 0.3 % carbon fiber and 5, 10 and 15% $CaCO_3$ whiskers in oil well composite cement mortar. Authors showed that not only the mixtures consisting individual fibers were able to increase the compressive, splitting tensile and flexural strength but also combination of both fibers outperformed all other mixtures showing denser structure and higher ductility.

Literature review of previous researches reveals that carbon fibers add significant values to the property of composite cement materials. Moreover, the hybrid effect of carbon fibers has shown superior performance compared to its individual effect. Despite all these benefits, the economic aspect of cement based composite material containing carbon fibers has been under question for many years. In a study performed by Chen and Chung (1993), a concrete mixture containing 0.5% virgin carbon fiber (by weight of cement) had 39% increase in the total price of the concrete.

In an effort to reduce the costs of the composite materials containing carbon fibers, Howarth et al. (2014) modeled the mechanical recycling energy consumption of carbon fiber and they concluded that the energy required for recycling process is 2.03 MJ/kg compared to 200 MJ/kg embodied energy of virgin carbon fiber. Additionally, Wood (2019) in an article about reclaimed carbon fiber, mentioned that the recycling cost can be at around 70 percent of the virgin production cost. Therefore, reclaiming carbon fibers despite the impurities may be still beneficial for industrial grade products. As an example, the incorporation of recycled carbon fiber composite materials in concrete can lead to some properties enhancement. There are three common methods for recycling carbon fiber: (1) Mechanically recycling, (2) Thermal recycling (Pyrolysis) and (3) Chemically recycling method. (Liu, Farnsworth, & Tiwari, 2017; Oliveux, Dandy, & Leeke, 2015)

Saccani et al. (2019) used shredded epoxy coated carbon fibers without any chemical reaction or temperature treatment in order to make cementitious based composites. In the virgin material, the epoxy was used to bind the carbon fibers matrix. According to their results, a decrease in workability was observed without any change in air voids but, slight increase in compressive strength, significant increase in flexural strength and a transition from brittleness to semi-ductile behavior was reported.

In another study, Rangelov et al. (2016) used low energy mechanically processed carbon fiber composite material in different sizes and volumes in reinforcing pervious concrete. According to their results, the incorporation of cured carbon fiber composite materials (CCFCM) increased the workability of the mixtures while decreasing the porosity as opposed to the previous literature reported on the regular cement mortar. The other observed effects were increasing infiltration rate, compressive strength and module of elasticity.

The reason that the researchers persist to use the mechanical recycling method is mainly because of the cost and energy efficiency. However, there has not been yet any study providing a detailed comparison between the cost and performance impact of mechanically, pyrolysis and chemically recycling carbon fibers in concrete or cement mortar. Those who using chemically recycled and

purified carbon fibers, believe that it is a more environmental friendly approach since epoxy -the bonding material in carbon fiber composite in mechanical recycling - is difficult to recycle or depolymerize in the environment after mixing with concrete. (W. Li et al., 2019) However, the literature on the incorporation of pyrolysis or chemically recycling carbon fibers in composite cement materials is very rare to widely verify actual benefits and life cycle cost analysis. In order to better understand the gap in this segment, it is required to investigate other methods than mechanically recycling of carbon fibers.

Glass Fibers

Table 1.4.3 - Properties of Fibercast 500 Fibers by Propex

Absorption	Acid/Salt Resistance	Alkali Resistance	Electrical Conductivity	Fiber Length	Ignition Point	Melting Point	Specific Gravity	Thermal Conductivity
Nil	High	Alkali Proof	Low	0.25-2 inches	759.2°F	320°F	0.91	Low

This fiber is composed of 100 % virgin homopolymer polypropylene fine fibers excluding olefin materials. Addition of fibers shouldn't require any additional water or mix design changes and should be added during and/or after the other materials have been introduced and mixed for an interval of time. Five minutes should suffice to allow a uniform distribution of these fibers into the mix. This fiber is compatible with all concrete admixtures and modifying chemicals. Commonplace applications of these fibers include precast, stucco, walls, septic, hazardous waste storage and general storage tanks, shotcrete, agricultural and marine products.

Benefits derived from the use of these fibers include increased early strength, cohesion and toughness in hardened state; reduced segregation, plastic shrinkage, settlement cracking, freeze damage, water mitigation, rebound and material waste; reinforces against shattering forces and abrasion; reduces/manages intrinsic cracking.

This fiber follows the guidelines set forth by the European Standard EN 14889-2:2006, ASTM C 1116/C 1116M, and ICC AC 032.

Recycled Tire Textiles

Scrap tire is a state that vehicle's tire reaches its end of life. The scrap tire loses its ability to provide enough friction with road surface. Sometimes damages cause early retirement of the tires such as leaking holes caused by sharp objects. Although the tire reaches its end of service life as a vehicles tire, there are plenty applications that it still meets for the requirements. U.S. Tire Manufacturer Association (USTMA) names key markets that utilize scrap tires in the United States. As an example, Tire-Derived Fuel (TDF) is used to fuel cement kilns and boilers. The advantages of the TDF over coal are higher heat production and less greenhouses emissions. The next market is Ground Rubber Application where grinded rubbers participate in manufacturing new rubber products, landscaping, sport fields, playgrounds and paving industries. Another market is dedicated to civil engineering applications such as landfilling constructions, variety form of walls and dampers. Considering these three major markets and all other industries together, it is

estimated that 81.4% of scrap tires are reclaimed in different forms. However, still 18.6% of the scrap tire is land disposed every year which is about 39.46 million tires or 646.78 thousands of tons. (USTMA, 2017) In concrete technology, scrap tire can be converted to several forms such as: (1) Ground tire rubber, (2) recycled tire steel fibers and (3) recycled tire fibers. A tire contains 4% of textiles as a structural component. Recycled tire textile can be used in concrete as a fiber mesh.

Polypropylene fibers

The polypropylene fiber is one of the most widely used fibers in industrial or common life, in geotextiles, fishing nets, packing bags, raincoats, overcoats, protective suits, curtains or tablecloths. In fact, waste polypropylene fiber fabrics constitute a large quantity of waste fiber fabric. Polypropylene-fiber-reinforced is used in many applications such as tunnel or ground slab and in pavement construction. Different fiber size can be used. Generally, macro fiber has a length of 50 mm and a diameter of 0.3 mm, and for microfibers they have a length of 12 mm and a diameter of 0.05 mm. At early ages of concrete, polypropylene microfibers are highly responsive to potential cracks. Small displacements adjacent to the fiber resulting from cracking activates the fiber strength and prevents the cracks spreading. This efficiency is enhanced further by the fact that certain types of polypropylene fiber are fibrillated and therefore extremely well embedded, even in a poorly compacted, low-adhesion matrix such as very early age concrete. However, the low Young's modulus of these synthetic fibers decreases their efficiency as the concrete matures. Consequently, cracks will be much larger in older, cracked structures which use concrete with macro-synthetic fibers than in concrete with steel fibers. (El-Newihy et al., 2018)

Polyvinyl-alcohol fibers

Polyvinyl alcohol (PVA) fibers are monofilament fibers that disperse throughout the concrete matrix, creating a multidirectional fiber network, providing shrinkage control, abrasion resistance, and protection from thermal expansion and contraction. When used at certain loading rates, PVA Fibers can be used as primary reinforcement. PVA reinforced concrete is tremendously ductile, or flexible. The concrete part will bend considerably before it breaks, as opposed to experiencing sudden catastrophic failure. These fibers are used in high-performance and ultra-high-performance fiber-reinforced concretes. (Banyhussan, 2016)

Properties of Fiber

Aspect ratio (length/diameter)

The aspect ratio of fibers is the ratio of its length to diameter. The recommended aspect ratio ranges from 30 to 80 according to Xu (2018). A higher aspect ratio resulted in increased load bearing capacity and flexural strength (Hameed, 2009). This is due to the fact that longer fibers can better bridge across cracks. Also according to Hameed, fiber ratios should be selected depending on maximum aggregate size to reduce cracks.

Shape

Steel reinforcing fibers come in many varying shapes. The different types of steel fibers are straight, hooked ends, crimped, and twin-cone shapes. The advantage of these shapes is to bridge cracks in the concrete and to resist pullout forces. Shaped fibers performed better than straight steel fibers after debonding from the concrete during loading tests. The pullout loads taken by the concrete reinforced with curvy fibers were all higher at lower displacements for curly fibers according to a study by Breitenbucher (2014). This is because the curvy shaped fibers provide more anchorage and can straighten out before failing. Future studies can be performed to analyze how fiber shape will affect workability of the fresh concrete for use in self-consolidating concrete.

Fiber Dispersion and Orientation

Other important properties of reinforcing fibers in concrete are fiber dispersion and orientation. Typically fibers are not expected to increase the strength, but to reduce cracking from shrinkage. Since shrinkage occurs throughout concrete, especially on the surfaces due to changes in temperature and moisture loss, the fiber dispersion has to be evenly distributed to yield the best results in concrete. The fiber orientation also affect the properties of concrete. According to Breitenbucher (2014), higher inclination angles of steel fibers resulted in earlier rupture and the recommended inclination angle of the fibers are between 35 to 45 degrees. When there was a higher fiber inclination angle, the localized stress increased to cause rupture at a lower displacement.

1.4.6 SCC Admixtures

The key admixtures used to produce SCC are Super-plasticizers (SP), High Range Water Reducing Agent (HRWR/HRWRA), and Viscos\ity-Modifying Admixture (VMA). Other admixtures such as air-entraining admixtures and set-modifying admixtures can also be used successfully in SCC. Chemical admixtures are mainly used in SCC for cast-in place bridge components to reduce water content, provide air entrainment, improve viscosity, and enhance workability retention. In special circumstances, other chemical admixtures are used to accelerate strength development, retard setting time, reduce drying shrinkage, and protect against reinforcement corrosion. The performance of chemical admixtures depends on the types and proportions of constituent materials, temperature, and compatibility among different admixtures.

Super-Plasticizers (SP)

SP of poly-carboxylic ether type are utilized to achieve workability targets. In modern concrete systems, usually powder content is high and mixing water content is low. Depending on the level of flow and aggregate grading, a third generation PCE based superplasticizer might encounter bleeding and segregation.

High- and Mid-Range Water Reducing Agent (HRWRA or MRWRA)

HRWR is an agent used to reduce water content and produce better flow ability. The properties the agent typically affects are prolonging setting time, slump and air entrainment depending on the dosage used. Such an agent when used in conjunction with VMA for example can achieve greater workability within the concrete. There are different types of HRWR, each capable of achieving the desired performance goals and correct any shortcomings of the designed SCC.

Viscosity Modifying Agent (VMA)
Normally for SCC with high water-powder ratio and/or low powder content, VMA is added to improve mix stability by enhancing rheological properties and reducing segregation.

1.5 SCC Test Methods

SCC tests constitutes of fresh, hardened and durability properties assessment. Test methods developed for the fresh properties of SCC are typically slump test, J-ring test, V-funnel test, L-box test, penetration test and column test. The test methods for hardened properties are typically compressive strength test, flexural strength test, density test and split tensile test. In durability assessment, following test methods can be mentioned: water absorption test, bulk electrical resistivity test and length change. In the next chapter, the test methods will be explained in details.

1.6 Applications of SCC

Findings for large scale construction were that SCC is useful in improper reach for formwork, congested reinforced concrete, thin-layer concreting and other similar situations; water/cement ratio must be above 0.4 for reducing loss of workability from time, but requires no change for increasing the actual workability; sand has lower finesse modulus; total volume, max size, and average diameters of aggregate and sand grading are very important; SCC requires more curing to reduce plastic shrinkage, strength loss, and cracking; SCC is fine aggregate, cement amount, mineral additive of filler, and HRWR sensitive; SCC requires more strength and non-leaking formwork in construction.

Underground Transportation Infrastructures

Precast Tunnel Liners with SCC
Injection tests, which has SCC filled into a mold from the bottom of it while the mold is in a vertical position. Pouring in this way avoids segregation from happening, which is an issue with pouring in the mold from the top. Segment innovative method utilizes a horizontal mold position for installing rebar cage, side walls, and stripping the segment after setting and curing; a vertical position for the SCC injection test and preventing air bubbles, angle for the mold is determined by positioning the vent horizontally and after the injection waterproofing close the vent cover. A full scale mold was designed and created with an economic body frame to have tests performed on it at a construction site by three mix designs for standard, polypropylene and steel fiber reinforced concrete with a rebar cage and welded mesh panels included. The purpose of the test was to measure the molds ability to be filled with SCC and agreeing with the homogeneity, density and facing aspects; identify the type of concrete that was compatible along with appropriate test specifications; analyze the molds usefulness and areas for improvement.

Application of SCC in Shotcrete, Grouting, Patching, and Waterproofing

During rehabilitation of tunnels ventilation arch walls were replaced, the original design used SCC and formwork for the replacement. This alternative design used self-bearing shotcrete for the ventilation arch wall and provides a freestanding arch to extend the underground portion of a tunnel to outside. This method allows all hangers to be removed once the demolish stage begins without needing replacement. It provides greater flexibility, reduced construction risk and time during ventilation arch wall installation and does not require hangers. The original design using SCC included demolishing and renovating the ventilation arch walls with concrete embedded u-shaped steel beams and radial hangers, which would be reinforced with welded wire fabric and curved steel formwork forming the cast-in- place arch. While having high performing flow ability the SCC exerted high hydrostatic stresses which has risk of rupturing formwork and concrete blowouts requiring costly custom formwork and causing elongation of project time which was further elongated due to needing to replace hangers.

CHAPTER 2 – EXPERIMENTAL PROGRAM

This chapter includes four parts. Part one is about materials used in the mixtures and their properties. Part 2 demonstrates SCC and mortar mixture proportions. In part 3, mixing procedure is explained and finally in part 4, all test methods are described.

2.1 Materials

SCC mixtures consist of cement, fly ash (FA), fine and coarse aggregate, water, super plasticizer (SP), viscosity modifying admixture (VMA) and fibers.

Portland cement type II complying with ASTM C-150 (2019) was used in this research. The specific gravity of the cement was 3.14. Fly ash class F with specific gravity of 2.32 was utilized as a partial cement substitution. 23% of total binder was replaced by fly ash. Table 2.1.1 shows the chemical composition of fly ash.

Table 2.1.1 Chemical composition of fly ash

Quartz	SiO_2	59.9%
Calcium Oxide	CaO	11.5%
Iron Oxide	Fe_2O_3	4.8%
Aluminum Oxide	Al_2O_3	14.3%
Sulfur Trioxide	SO_3	1.1%
Sodium Oxide	Na_2O	0.6%
Potassium Oxide	K_2O	0.4%
Moisture Content	-	0.2%
LOI	-	2.4%

Washed coarse sand with maximum aggregate size of 4.75 mm used as fine aggregate and washed washed gravel with maximum aggregate size of 9.5 mm was used as coarse aggregate. For mortar mixtures, fine aggregate with maximum aggregate size of 1.18 mm was used.

A polycarboxylate-based high-range water reducer used as Super plasticizer (SP) to increase the flowability of the mixtures. Viscosity-modifying admixture (VMA) was used to enhance the stability and prevent segregation.

Seven different fibers were used in this study are as followings: Recycled tire steel (RTS), recycled tire textile (RTT), recycled carbon fiber (CF), monofilament polypropylene micro-fiber (MFP), polypropylene / polyethylene synthetic macro-fiber (MSF), homopolymer polypropylene fibers (HPF) and steel hooked fiber (SHF). Table 2.1.2 shows the properties of these fibers.

Table 2.1.2 Properties of fibers

Type of fiber	Length (mm)	Aspect ratio	Shape	Tensile strength (MPa)
Steel Hooked Fiber	30	65	Hooked end	1100
Recycled Carbon Fiber	5	150	straight	3 500
Polypropylene Micro-Fiber	12	140	straight	300
Macro synthetic Fiber	56	74	flexible	600
Recycled Tire Steel	34	60-135	irregular	NA
Recycled Tire Textile	10	30	irregular	NA
Homopolymer polypropylene	6	NA	straight	660

Figures shown in the following demonstrates the fibers image in different magnifications.

Figure 2.1.1 Steel Hooked Fibers

Figure 2.1.2 Recycled Carbon Fibers

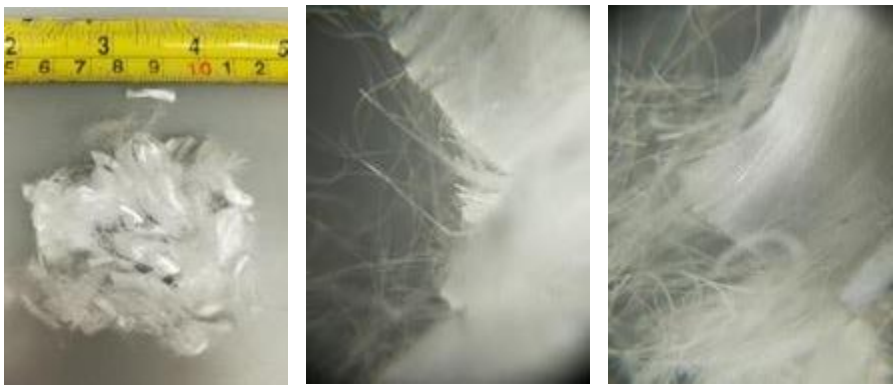

Figure 2.1.3 Polypropylene Micro-Fiber

Figure 2.1.4 Macro synthetic Fiber

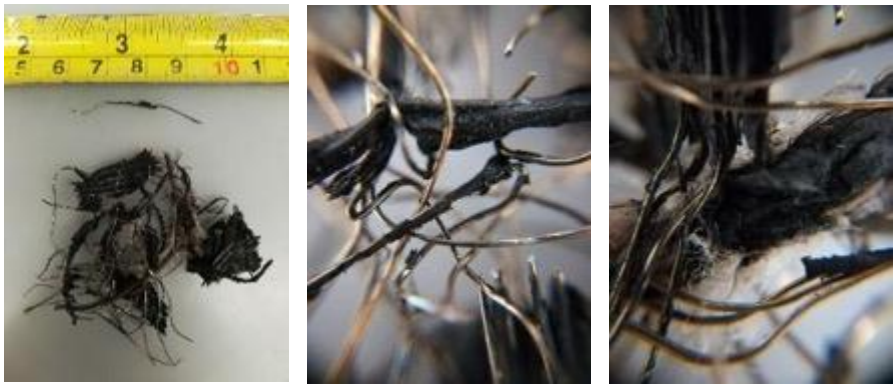

Figure 2.1.5 Recycled Tire Steel

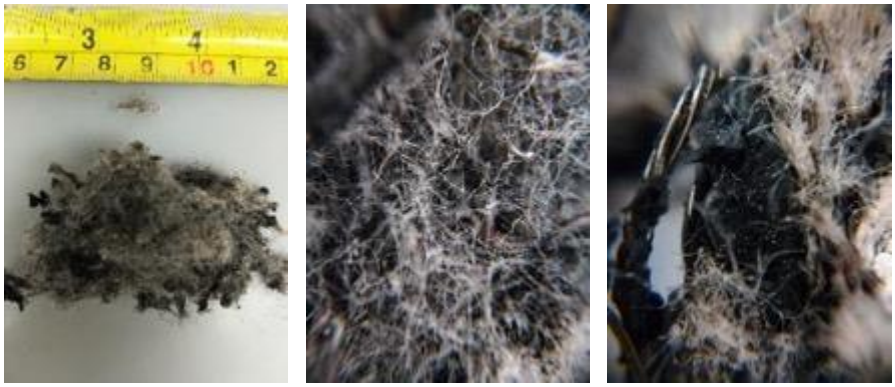

Figure 2.1.6 Recycled Tire Textile

Figure 2.1.7 Homopolymer polypropylene Fibers

2.2 SCC Mixture Proportions

The procedure followed for the SCC mix design is discussed in this section.
The mixes are made up of Type II/V Portland cement, Class F Fly Ash, course aggregates (3/8" gravel), fine aggregates (sand), water, high range water reducer and viscosity modifying admixture which are materials typically used in SCC mixes. A 0.49 water to cement ratio was used. Table 2.2.1 shows the SCC mixture proportions.

Table 2.2.1 SCC mixture proportions

	Cement (kg/m^3)	Fly Ash (kg/m^3)	W/C	Water (kg/m^3)	Coarse Agg. (kg/m^3)	Fine Agg. (kg/m^3)	Air Voids %	SP	VMA
	422.8	**126.8**	**0.49**	**207.2**	**541.2**	**718.8**	-	-	-
% by weight	21.0	6.3	-	10.3	26.8	35.6	-	0.90*	1.02*
% by volume	14.1	5.5	-	20.7	21.8	28.0	10.0	-	-

*% by weight of cementitious materials

Based on the available equipment, the length change measurement could be performed only on mortar mixtures. Therefore, a mortar version of above SCC mixture was developed. To maintain the similarities, the coarse aggregate proportion was replaced by fine aggregate and a slight adjustment was applied to the other materials to obtain flowability. The mortar mixture is labeled as Self Consolidating Mortar (SCM). Table 2.2.2 shows the mixture proportions for SCM.

Table 2.2.2 SCM mixture proportions

	Cement (kg/m^3)	Fly Ash (kg/m^3)	W/C	Water (kg/m^3)	Coarse Agg. (kg/m^3)	Fine Agg. (kg/m^3)	Air Voids %	SP	VMA
	468.4	**-**	**0.5**	**234.2**	**-**	**1309.9**	-	-	-
% by weight	23.2	-	-	11.6	-	65.0	-	1.80%*	0.63%*
% by volume	15.6	-	-	23.4	-	50.9	10.0	-	-

*% by weight of cementitious materials

In the following Table 2.2.3, mixture labels containing different fibers and their proportions are described.

Table 2.2.3 Fiber proportions* and mixture labeling

Label	Recycled Tire Steel	Recycled Tire Textile	Recycled Carbon Fiber	Homopolymer Polypropylene Fibers	Macro Synthetic Fibers	Monofilament Polypropylene	Steel Hooked Fibers
CTRL	-	-	-	-	-	-	-
RTS	0.05%	-	-	-	-	-	-
RTT	-	0.05%	-	-	-	-	-
CF	-		0.05%	-	-	-	-
HPF	-			0.05%	-	-	-
MSF	-	-	-	-	0.05%	-	-
MFP	-	-	-	-	-	0.05%	-
SHF	-	-	-	-	-		0.05%
CF+RTT	-	0.025%	0.025%	-	-	-	-
CF+RTS	0.025%	-	0.025%	-	-	-	-

*All percentages are based on the total mass of the concrete mixture.

2.3 Mixing Procedure

To make SCC mixtures, high range water reducing admixture was dissolved in the water, first. Then half portion of the solution was mixed with coarse and fine aggregates for 1 minute. All other components placed in the mixture in the following order: cement, fly ash, water solution, and VMA and mixed for 5 minutes.

Immediately after mixing, fresh property tests were performed and then the concrete mixture was molded for hardening properties and durability tests.

Since SCM mixtures required less quantities, a smaller mixer was used to produce the mortar and slight adjustment was made in the order of combining materials. The procedure started with mixing fine aggregate and cement together for 1 minute. The high range water reducing admixture was added to the water and mixed with the solid components. Then VMA was added and the whole mixing process from the moment that water solution was added took 5 minutes.

2.4 Test Methods

In this part, fresh properties, hardened properties, and durability test methods will be explained.

J-ring test was the first test performed immediately after mixing. J-ring can measure the passing ability of the mixture. This test was in accordance with ASTM C1621. While slump cone is used, the penetration apparatus can be utilized to assess the static segregation resistance of the mixture based on ASTM C1712. Figure 2.4.1-(a) and 2.4.1-(b) show J-ring setup and penetration test apparatus, respectively.

Figure 2.4.1 (a) J-ring setup and (b) penetration test apparatus

To complete the J-ring test, slump flow test is required. This test method is based on ASTM C1611. Figure 2.4.2 shows the slump test apparatus.

Figure 2.4.2 Slump test apparatus

The next test is L-box test. L-box apparatus evaluates the filling ability, passing ability and segregation resistance. The test method used is a guidelines provided by BS EN 12350-10 (2019).

Figure 2.4.3 L-box test apparatus

The last test in fresh properties part is V-funnel test. V-funnel measures the time that took for the whole concrete to flow out of the funnel. The measured time could be an indication of segregation resistant. V-funnel test method was performed based on BS EN 12350-9 (2010). Figure 2.4.4 shows the V-funnel apparatus.

Figure 2.4.4 V-funnel test apparatus

100 × 200 mm cylindrical SCC specimens were made and cured in moisture room at room temperature for 7 and 28 days based on ASTM C192 (2018). These specimens were used for compressive test in accordance with ASTM C39 (2018). Additionally, specimen were capped by sulfur to provide flat surface on top and bottom of the specimens. The approach for capping is described in ASTM C617 (2015).

Split tensile strength test is an indirect test method for tensile strength evaluation. For this purpose, cylindrical specimens with 100 mm diameter and 200 mm height were made and cured for 28 days. The test method was performed based on ASTM C496 (2017).

Length change test is a durability test to determine the shrinkage of cement paste, mortar or concrete specimens during time. The guidelines are followed by ASTM C490 (2017) to perform this test. Figure 2.4.5 shows the apparatus measuring the change in length of a prismatic specimen.

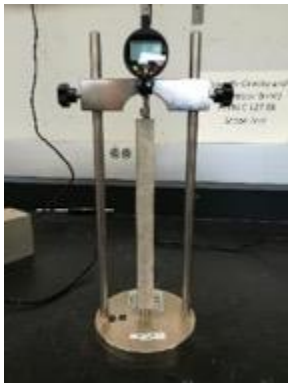

Figure 2.4.4 V-funnel test apparatus

CHAPTER 3 – RESULTS AND DISCUSSION

3.1 Fresh properties

3.2 Compressive Strength

Figure 3.2.1 provides compressive strength of mixtures containing different fibers at 7 and 28 days. The label values show the average of three specimens. According to the results, all specimens at the age of 7 days showed higher compressive strength compared to the control specimen. The range of strength varies from 8% for RTT mixture to 40 % for CF mixture. While the cement hydration process is still ongoing at early ages, the fibers could have helped the matrix structure to enhance the compressive strength. At 28 days, all specimens' strengths fell below the average control strength. The lowest value was measured for CF mixture with 16% less strength, followed by HPF and MFP mixtures for 15% and 13%, respectively. Alhozaimy et al. (1996) performed one- way analysis of variance on 28 days compressive strength of concrete specimens made with polypropylene fibers by up to 0.3% volume fraction. They reported that the polypropylene impact was not statistically significant at 95% confidence level. Song et al. (2005) reported that the compressive strength of concrete mixtures consisting of 0.6 kg/m^3 polypropylene fibers increased the 28 days compressive strength up to 6%. Another study supported the positive impact of coarse monofilament and staple polypropylene fibers.on compressive strength of concrete at 9 kg/m^3 and 0.6 kg/m^3 respectively. (Hsie et al. 2008). In a study conducted by Karahan, O., Duran Atis, C. (2011), the effect of propylene fibers investigated on different cement proportions and they showed that the fiber effect can vary from positive to negative based on cement paste content. Therefore, it is understandable that both fiber content and concrete proportions have major impact on the mechanical properties of concrete.

The one-way analysis of variance with $\alpha = 0.05$ showed that the there is no significant difference between fiber reinforced mixtures at 7 days. But when they were compared to control mixture, there was significant difference. At 28 days, statistically there were significant differences among fibers reinforced mixtures and fibers reinforced – control specimens.

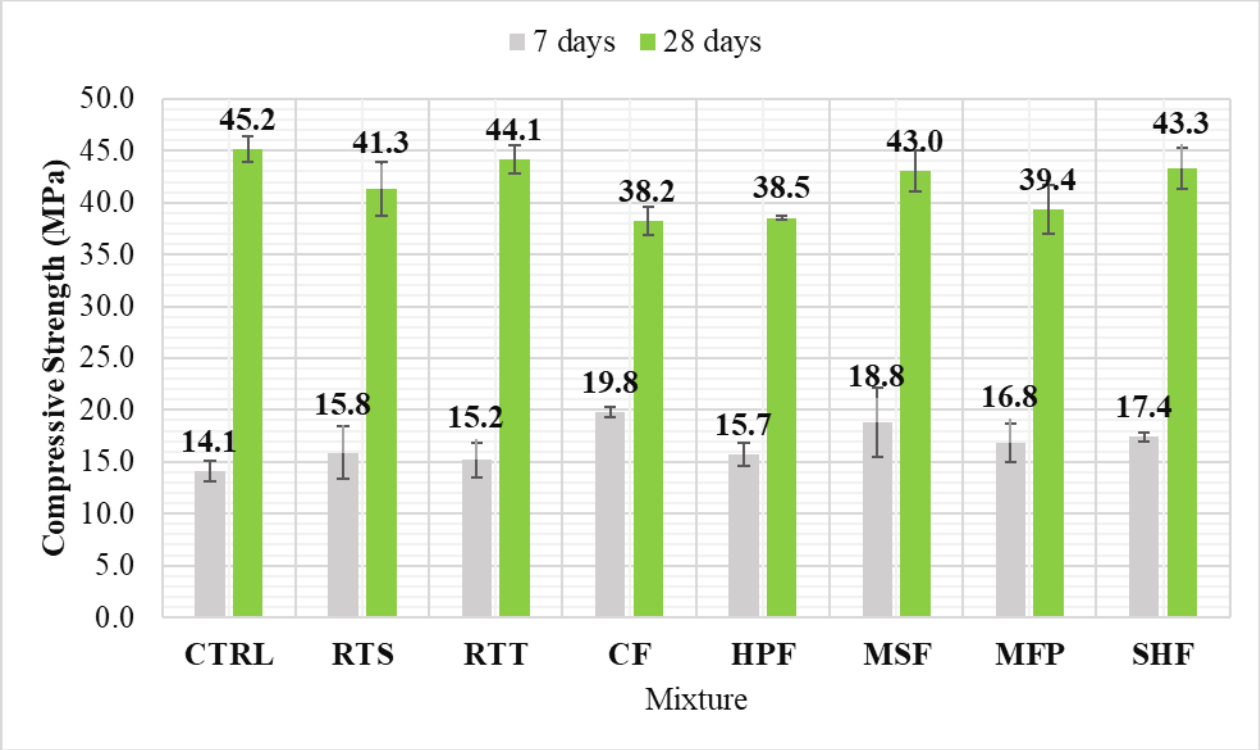

Figure 3.2.1 The comparison of compressive strengths at 7th and 28th days

Figure 3.2.2 shows the deviation of compressive strength at both 7 and 28 days from the control mixture. The closer the results are to the zero dashed line, the less impact the fibers have on the compressive strength of the SCC. Based the results, RTT is the closest data set to the zero dashed line at both 7 and 28 days. It shows that recycled tire textile has lowest contribution to the compressive strength compared to the other fibers. On the other hand, CF mixture showed the highest contribution to the compressive strength, the highest strength gained at early age and the highest strength loss at 28 days. By looking at the right side of the Figure 3.2.2, it is noticeable that mixture at 7 and 28 days follow predictable pattern. The mixture with lowest strength gain at 7 days, showed lowest strength at 28 and vice versa.

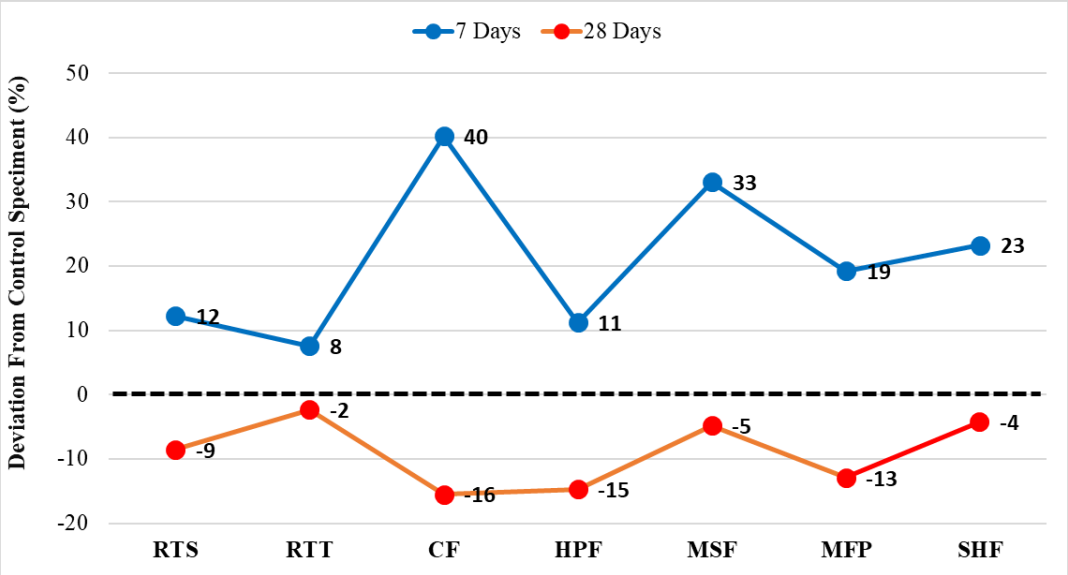

Figure 3.2.2 The deviation of compressive strength from control specimen (%).

3.3 Split Tensile Strength

SCC cylinders with 100 mm diameter and 200 mm height were made to test split tensile strength of mixtures. Figure 3.3.1 shows the result split tensile strength of three specimens for each mixture at age 28th day. Despite the steel fibers exist in the RTS mixture, the strength was 22% lower than control specimen. One reason could be because of the impurity of the recycled tire steel containing ground tire rubbers. Ground tire rubber can decrease the tensile strength up to 25%. (Eldin & Senouci, 1993; Huang, Li, Pang, & Eggers, 2004; Khatib & Bayomy, 1999) RTF mixture showed 30% lower split tensile strength which is the lowest amount among all other fibers. Recycled carbon fiber increased the split tensile strength by 6%. After CF mixture, MSF mixture had the highest split tensile strength compared to other mixtures but almost equal to the control mixture with 1% difference. A one-way analysis of variance showed that the P-value is equal to 0.0008 at 95% confidence level. Therefore, statistically there is significant difference between fibers impact on the result of split tensile strength. In literature, there are controversial conclusions on the impact of the fibers. Several researchers have demonstrated that the addition of fibers usually improve the split tensile strength. (Song et al. 2005; Hsie et al. 2008) However, these results are highly dependent on the mixture proportions including aggregate and cement paste ratio.

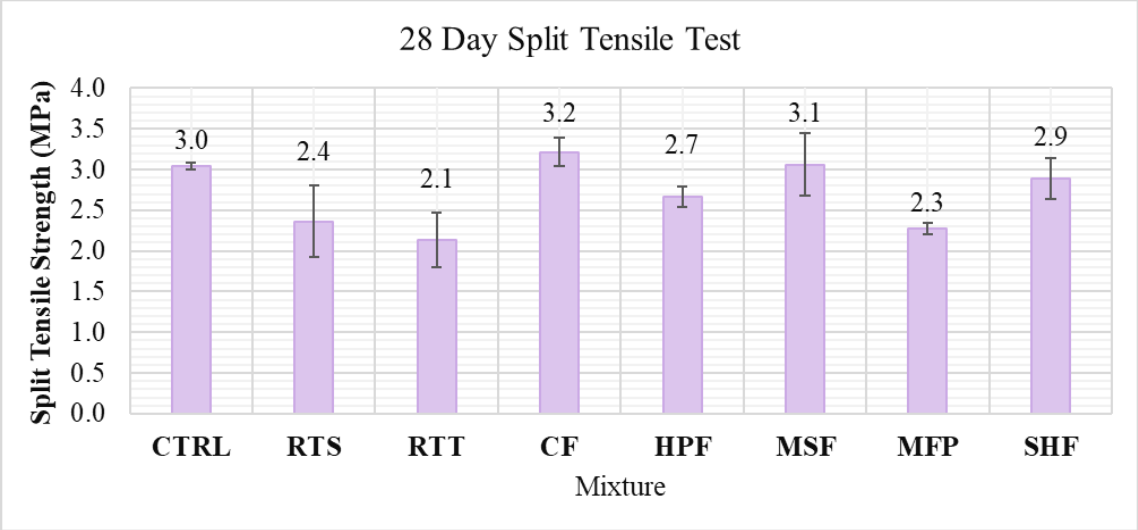

Figure 3.3.1 The result of split tensile test for SCC mixtures

3.4 Density

The air content of SCC mixtures versus compressive strength is demonstrated in Figure 3.4.1. MSF and MFP mixtures had the highest air content and RTS, RTT and control mixtures had the lowest air content. Although the lowest air content resulted in higher compressive strength, but the higher air content did not lead to lower strength. It can be concluded that there are other parameters than air content affecting the compressive strength of SCC mixtures. To further investigate the parameters, the relation between bulk density and compressive strength is plotted in Figure 3.4.2.

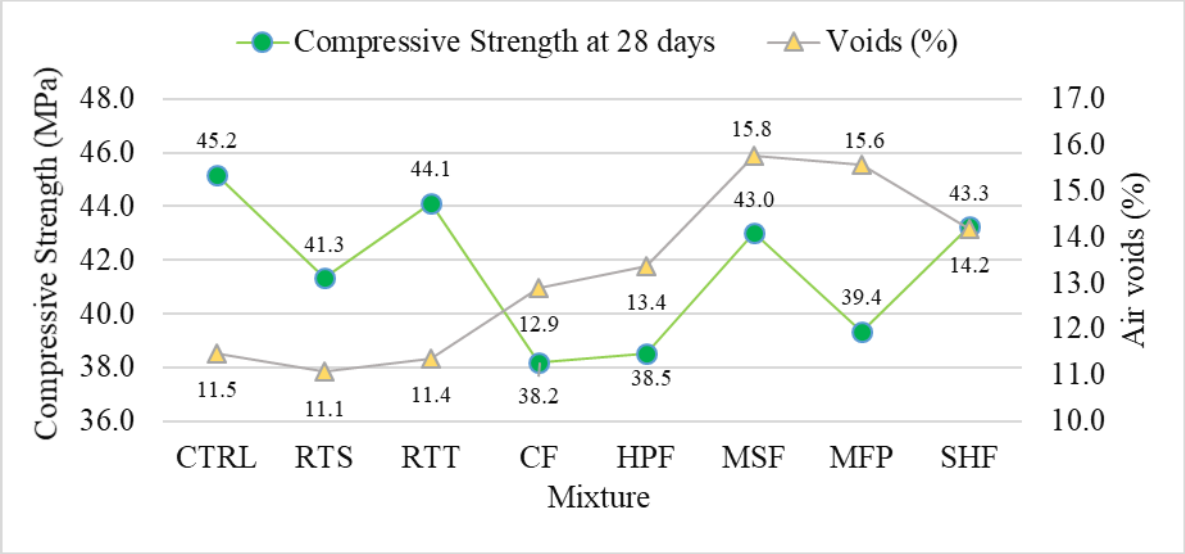

Figure 3.4.1 The relation between air voids and compressive strength of SCC mixtures

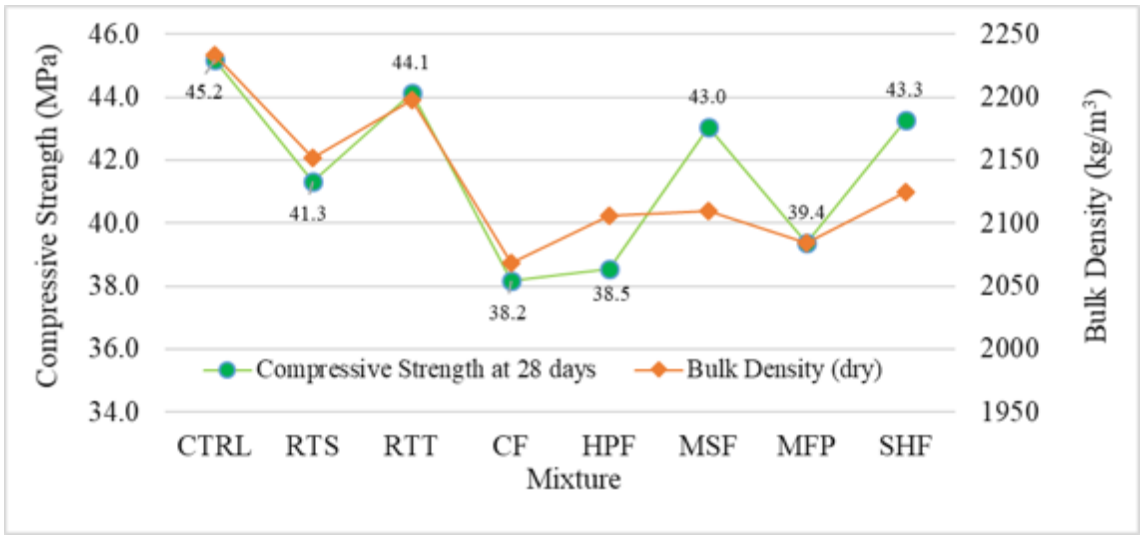

Figure 3.4.2 the relation between bulk density and compressive strength of SCC mixtures

According to Figure , bulk density has similar trend to the compressive strength of SCC mixtures. After control specimen, RTT, MFP, and SHF specimen showed high strength which is correlated with their higher bulk density. Following the correlation trend, CF and HPF with the lowest compressive strength had lower bulk density compared to the other specimens.

3.5 Water Absorption

In Figure 3.5.1, water absorption after 48 hours of immersion and water absorption after 5 hours of boiling condition are demonstrated. On the right axes, air voids (%) is added to investigate the correlation with water absorption. Among all specimens, RTS and RTT had similar water absorption level ab both 48 hours immersion and boiling condition. The water absorption for CF specimen at 6.5% did not changed before and after boiling condition. Among all specimens, MSF had the highest water absorption rate before boiling. However, after boiling, MSF and MFP showed similar rate of 7.5%. Although in 48 hours immersion, SHF had lower absorption rate compared to CF specimen, later after boiling condition, it showed 0.2 % higher absorption rate. All values are based on the average of three specimens for each mixture type. Figure 3.5.1 shows that the higher rate of air voids could be the reason for higher water absorption experimentally.

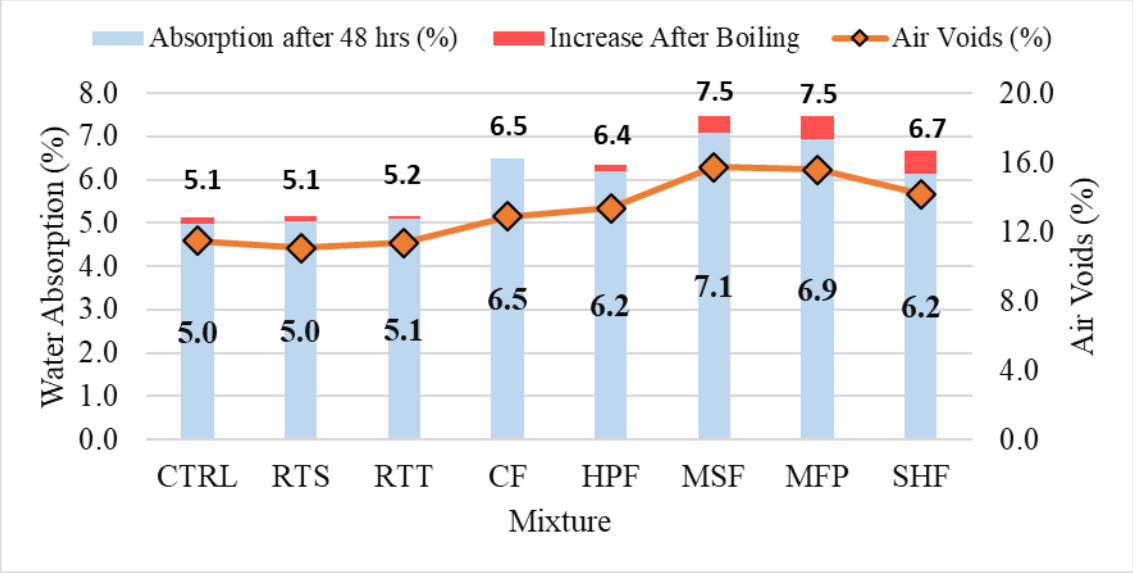

Figure 3.5.1 Water absorption and air voids of mixtures containing different fibers

3.6 Length change

In figure 3.6.1 the length change of mortar mixtures containing recycled carbon fiber and recycled tire textile are demonstrated for 45 days period. During the first 15 days, CF specimens followed similar amount of length change to the control mixture. After 15 days, the CF specimens started to deviate from the control mixture and at the 45th days the length change in the CF specimens was 16% lower than the control specimens. On the other hand, the RTT mixture improved the early age length change by 16% and at the end of the period, the specimens showed 20% less changes in length compared to the control mixture.

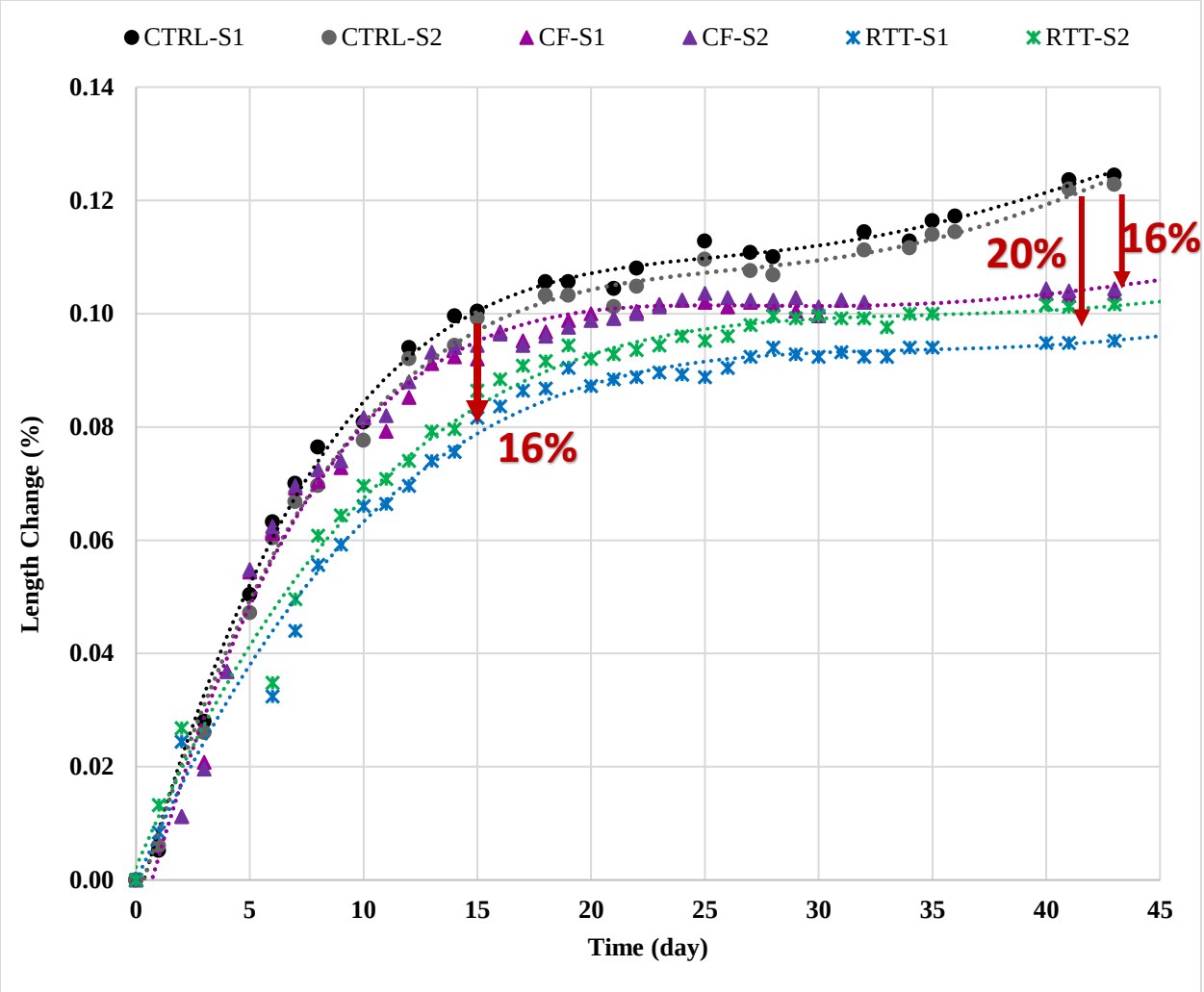

Figure 3.6.1 Length change of SCM mixtures

CHAPTER 4 – BINARY MIXTURES

4.1 Fresh properties

4.2 Compressive Strength

To understand the hybrid effect of carbon fibers, recycled tire steels and recycled tire textiles in SCC, cylindrical specimens were made and tested at 7 days and 28 days. Figure 4.2.1 shows the average value and standard deviation of three specimens for each mix. All fibers improved the early strength at 7 days, individually. This trend continued in the hybrid mixtures of both CF+RTT and CF+RTS. At 28 days carbon fiber had negative impact on strength gain. The hybrid effect at 28 days showed that this negative impact would not change by the addition of recycled tire textile but can be neutralized by recycled tire steel.

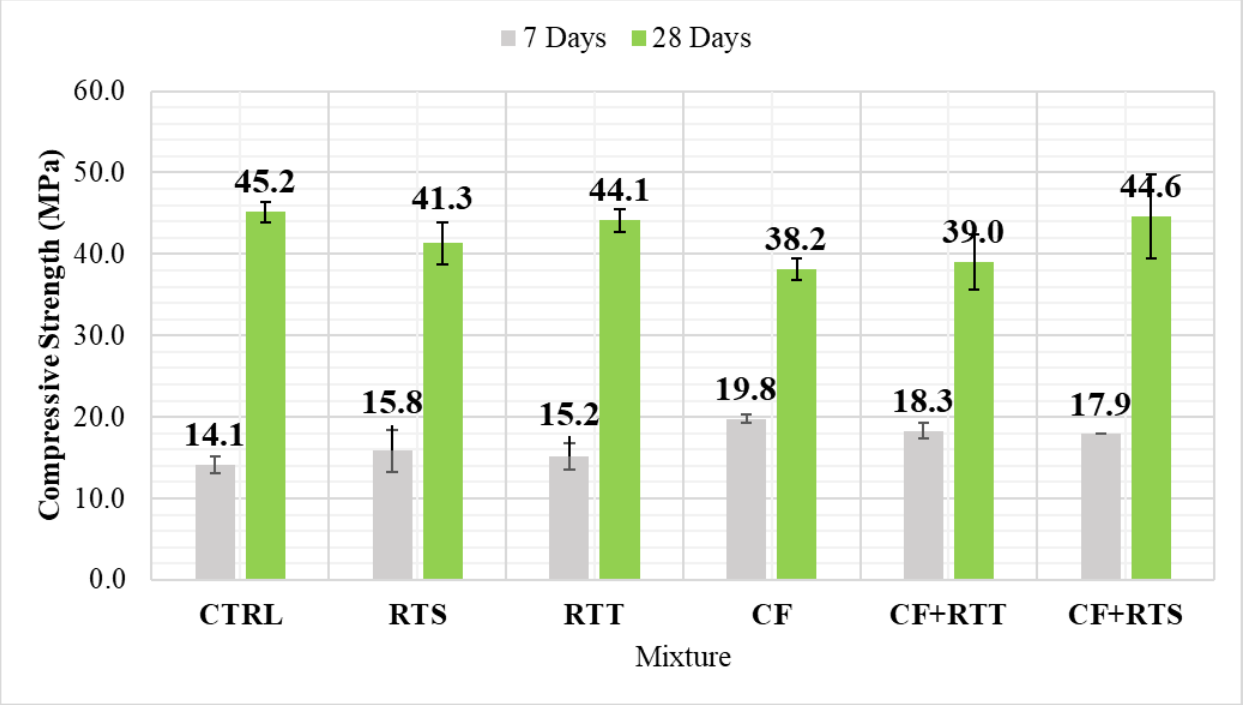

Figure 4.2.1 The comparison of compressive strengths at 7th and 28th days

Mortar compressive strength test result shown in Figure 4.2.2 indicates that there is a reverse trend in compressive strength gain compared to concrete specimens. CF mixture showed 6% and 18% less strength at 7 and 14 days but at 28 days gained 10% more strength compared to the control specimen. RTT mixture had equal strength at 7 days and 6% less strength at 14 days. Then at 28 days the strength raised to 8% above control specimen.

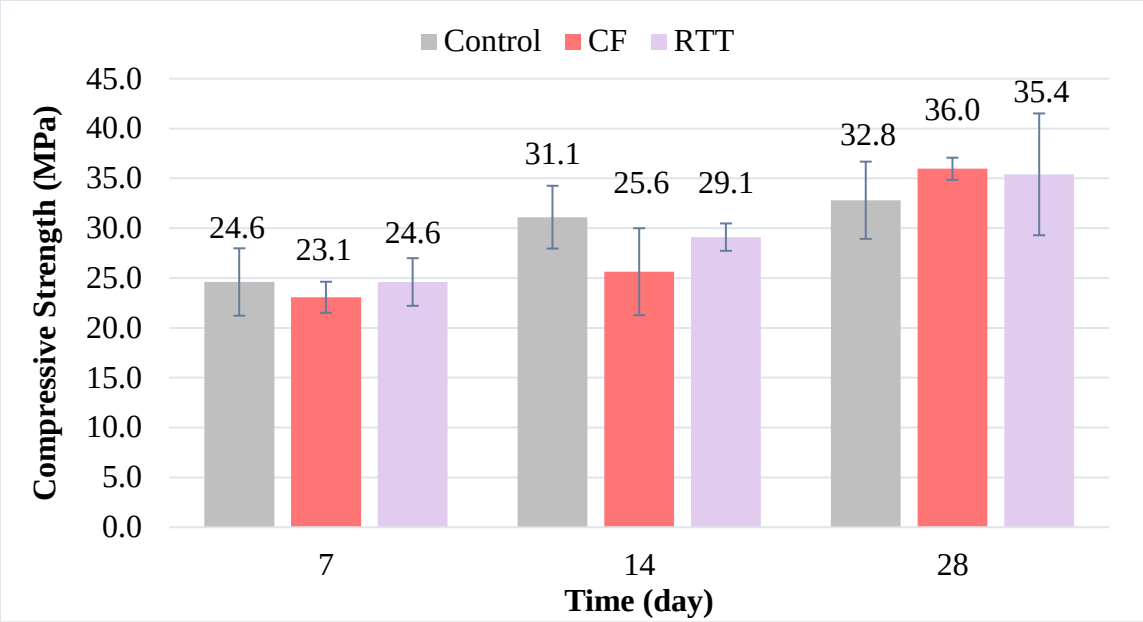

Figure 4.2.2 Mortar compressive strength at different ages

4.3 Split Tensile Strength

As discussed in chapter IV, the addition of recycled tire textile and recycled tire steel reduced the split tensile strength of SCC specimens while mixture containing recycled carbon fiber showed 6% strength enhancement. Now, the question raises whether carbon fiber can help RTT and RTS mixtures to compensate a portion of lost strength? According to the results shown in Figure 4.3.1, hybrid effect of carbon fiber and recycled tire textile had 25% improvement in split tensile strength compared to the RTT mixture. Also, addition of recycled carbon fiber to the recycled tire steel improved the split tensile strength by 27% achieving 5% higher than control mixture.

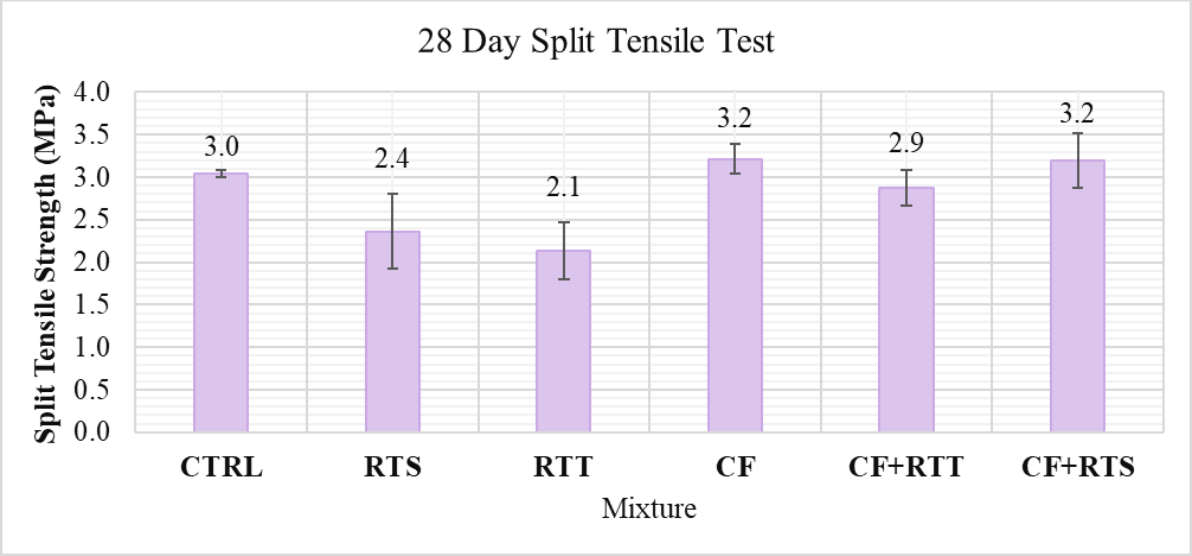

Figure 4.3.1 Split tensile strength for individual and hybrid mixtures

4.4 Density

The plot in Figure 4.4.1 shows the correlation between air voids and compressive strength of individual and hybrid mixtures. As the plot shows, recycled carbon fiber increases the air voids in the mixtures. This effect can be seen in both individual and hybrid specimens.

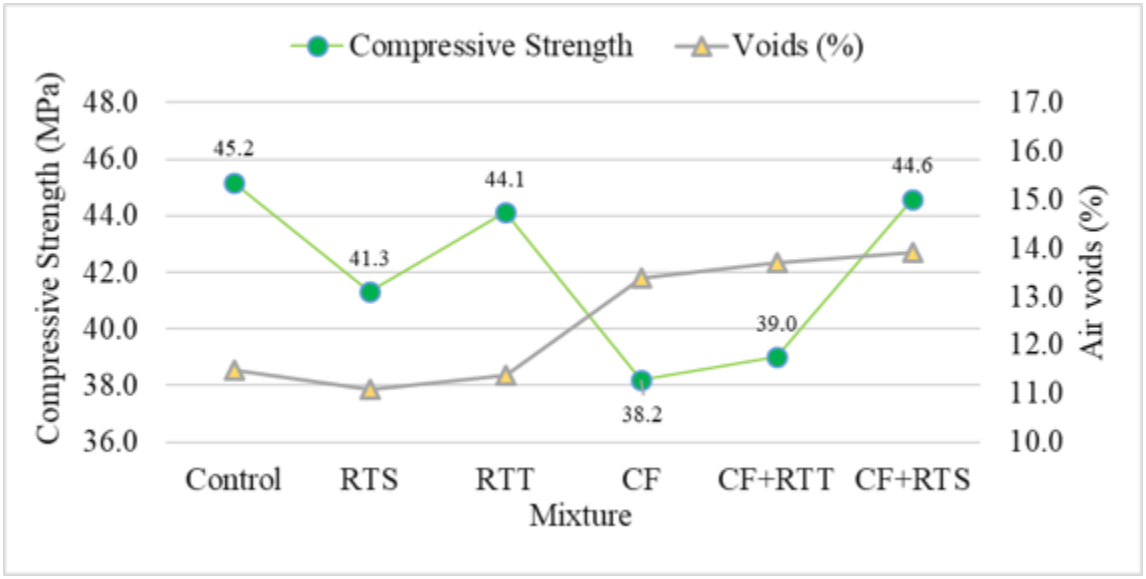

Figure 4.4.1 The relation between air voids and compressive strength of hybrid mixtures

Figure 4.4.2 represents the correlation of the bulk density to the compressive strength. Similar to the part 3.4 in previous chapter, the bulk density shows closer correlation with compressive strength compared to the air voids.

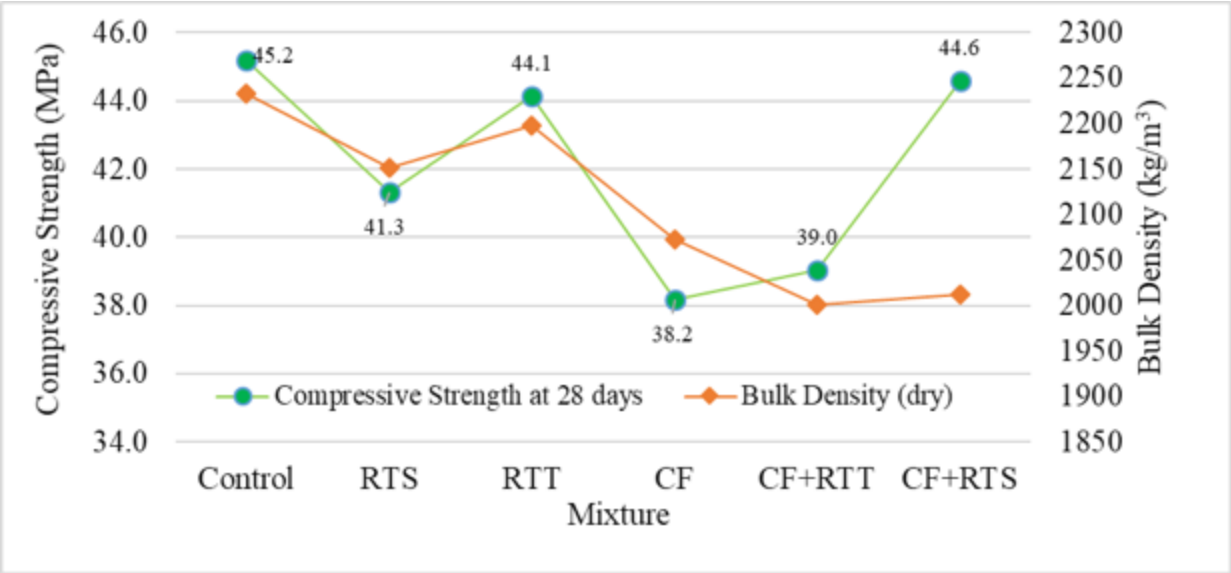

Figure 4.4.2 The relation between bulk density and compressive strength of hybrid mixtures

4.5 Water Absorption

Figure 4.5.1 represents water absorption and air voids of mixtures containing individual and hybrid fibers. In individual mixtures, recycled carbon fiber had increased air voids of the mixture and hence the water absorption had a higher rate compared to the recycled tire steel fibers and textiles. The water absorption rate in hybrid mixtures was also affected by the recycled carbon fiber.

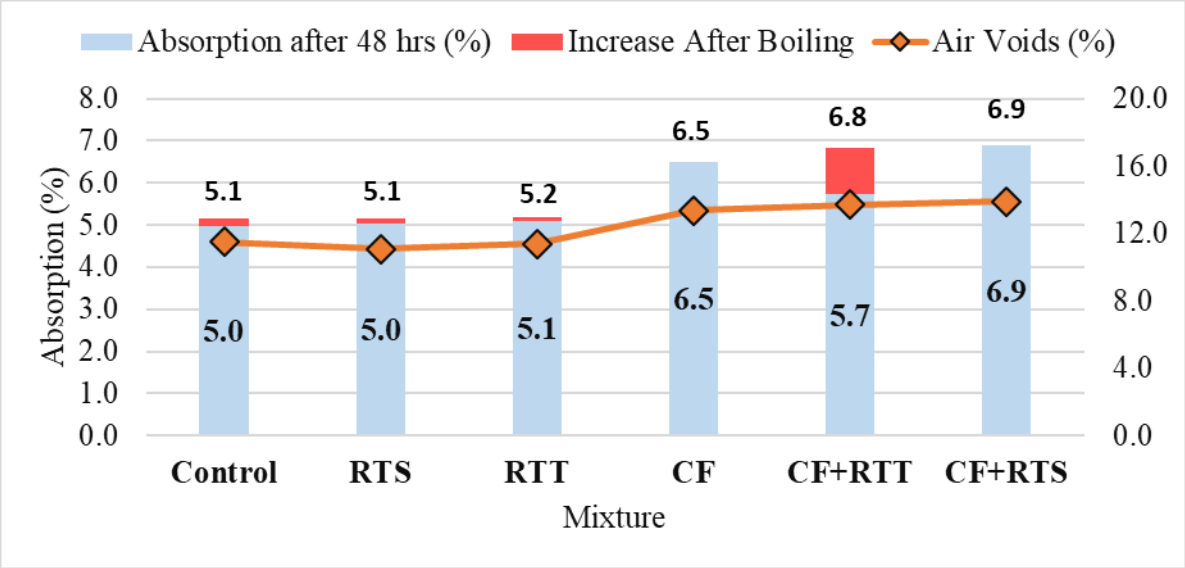

Figure 4.5.1 Water absorption and air voids of mixtures containing individual and hybrid fibers

Recycled tire textile in the hybrid mix reduced the negative impact of carbon fiber on water absorption from 6.5% to 5.7% and during the 48 hours immersion. However, after 5 hours of boiling condition, the absorption rate increased to 6.8%. The hybrid mixture containing recycled tire steel had the highest absorption rate of 6.9%. RTS and CF specimens reached their maximum absorption rate before boiling condition.

4.6 Bulk Electrical Resistivity

Figure 4.6.1 shows a radar graph of bulk electrical resistivity for CTRL, RTS, RTT, CF and CF+RTT mixtures. The RTS mixture showed lower electrical resistivity compared to the other mixtures. The main reason for this behavior is the existence of steel fibers increasing the conductivity. Even though the air content and water absorption values showed similar results between RTT and control mixtures, the electrical resistivity was 17% improved when recycled tire textile was used. In CF and CF+RTT mixtures, addition of recycled carbon fiber extremely increased the electrical resistivity of the hardened samples. This behavior suggests that recycled carbon fiber can improve the durability of the concrete by reducing the ion penetrations. Additionally, it can be concluded that the lower content of recycled carbon fiber at 0.25% can be as effective as the higher dosage at 0.5%.

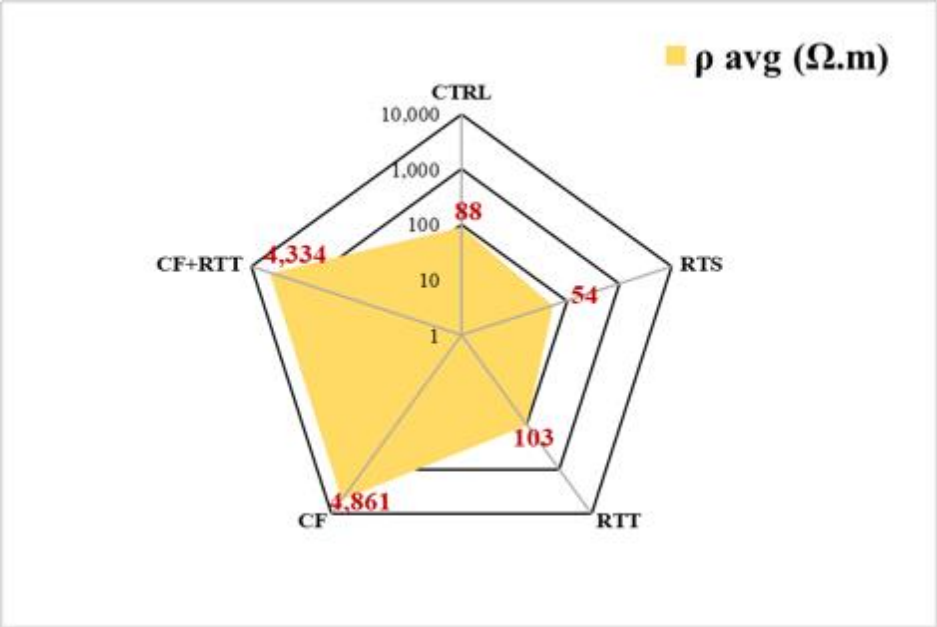

Figure 4.6.1 Bulk electrical resistivity of individual and hybrid mixtures.

CHAPTER 5 – SURFACE DISPLACEMENT MEASUREMENT

5.2 Introduction

The application of computer-based image correlation and analysis has been gaining popularity with increasing availability of advanced optical devices. Programs have been developed to follow movement by detecting key features in the image and comparing frame-by-frame images to track the features of interest. Those programs can benefit researchers to improve on existing inspection methods and structural health monitoring processes. Currently there are numerous applications for image-based analysis such as deformation monitoring of bridge elements, pavement surface crack detection, and crack identification on tunnel lining surfaces. Improvements being made for these applications and as challenges hindering, more practical image capturing methods such as unmanned aerial systems, can be pursued.

The image correlation algorithms can also be employed for evaluating the hardened property measurements of concrete specimens in the laboratory conditions and further applied in the field. Currently strain gauges are used to collect displacement data for compression testing. However, they require high-precision linear variable transducer connected to a data acquisition system to record the specific points on interest on the specimen surface. These measurements are usually localized and limited to a specified surface area. The need for a non-contacting strain measurement for concrete surfaces is highly sought after for both laboratory applications that could be further calibrated and expanded to field applications. These methods allow for unlimit ed tracking on any visible point on the captured image of the concrete surface and can produce a more in-depth analysis of the surface deformations.

The main objective of this study was to develop a method for utilizing video recordings of concrete specimen surface in the laboratory to estimate the surface displacement and strain. Several concrete cylinder samples were prepared and analyzed during both compression and splitting tensile strength tests to evaluate the preliminary results. There are various factors that contribute to the ability of the algorithm to accurately detect features and analyze them. An optimal test setting will be achievable upon availability of different testing conditions and refinement of the developed algorithm.

5.3 Background

There has been a growing interest for non-contact test methods for evaluating the health and performance of structures throughout the literature. Concrete is a common material used in construction and understanding its properties ensure the safety and durability of structures. The recent techniques that utilize image correlation and analysis, such as Speckle statistics, are being tested to eliminate the need for conventional methods. (Sadana et al., 2015) Speckle statistics is a form of digital image correlation in which speckle patterns, with random intensity distribution, are compared during before and after images to evaluate displacement and deformation. The surface

of a specimen is illuminated by a laser light to generate a speckled appearance. The speckled appearance is compared between frames and images to determine correlations between those patterns through superimposition. The displacement of the surface can then be measured by tracking the speckle patterns over time (Leendertz, J. A., 1970). The setup requires a Diode-Pumped Solid-State laser, positive lens, screen, and a high-resolution video camera. The captured images were then processed for strain calculations and compared with results from three compression tests. Overlaying graphs from the two methods demonstrated that the results were fairly accurate with a 5.6 percent average uncertainty, making this method a fairly reliable technique for measuring strain. That study established the potential of speckle statistics for measuring strain (Leendertz, J. A., 1970).

Another technique is Digital Image Correlation (DIC) which compares before and after images to measure deformation of an object surface. Introduced in the 1980s, DIC algorithms focus on increasing correlation speed and accuracy. DIC is highly sensitive to lighting conditions, requiring a specific setup in order to maintain consistent results during testing. Correlation between images is determined by tracking matching pixel subsets. An image has a constant dimension size that is represented by number of pixels in the vertical and horizontal directions. Subsets are determined within this region and tracked throughout the deformation process. Recently DIC has been implemented to aid in problems such as fracture mechanics investigation and high temperature deformation analysis (Zhang, K., 2014). Developing strain and displacement measurement techniques that are accurate and cost effective are highly desirable. Studies on DIC attempt to achieve this by providing a method that is simple and practical for laboratory and field applications (McCormick, N., Lord, J., 2010) Although there are other techniques, such as laser shearography and speckle interferometry, DIC is simpler to apply in field conditions since required equipment is mainly an image capturing device. However, there are still challenges with accuracy due to effects from the environment and potential changes to surfaces being observed. Studies have demonstrated the potential applications of DIC but further work required to produce a method that is reliable for field conditions (Zhang, K., 2014).

Deformation on concrete structure surfaces leads to crack formation which is an indication of failure thus requiring a monitoring system to ensure durability. Image correlation techniques can be applicable to this situation to reduce manual inspections and improve detection rates. The validity of these techniques was investigated in a study reviewing 50 papers to evaluate the quality of image processing for crack detection and potential use in field conditions (Mohan, A. and Poobal, S., 2018). Typically, those studies have used image correlation and analysis methods following the procedure of capturing images, pre-processing, image processing, feature detection, and parameter estimation. Various methods were investigated such as DIC, morphological approach, speckle statistics, photogrammetric technique, and reconstruction technique to name a few. Each study attempted to measure various features of cracks on surfaces with varying results. The range of accuracy was between 70 to 95 percent with a few cases achieving higher than 95 percent accuracy. That review study demonstrated the potential that image analysis techniques have for practical use as well as shortcomings that need to be improved to increase accuracy (Mohan, A. and Poobal, S., 2018).

Other applications of optical techniques include measurements of deformation in bridge elements. A study utilizing moiré photography and photogrammetry demonstrated the potential benefits of applying image analysis compared to existing monitoring and testing methods. A destructive load test on a bridge structure was measured and compared to the conventional technique (Forno, C., et al., 1991). The method required the surface be covered in dotted patterned paper. Sequential images were then collected with various cameras, using a point of intersection to calculate the position of feature being focused. Displacements in the x and y directions could then be measured by comparing images. Limitations of that method were target recognition and measurements of positions. Further development in that technique can lead to simpler evaluation and monitoring methods for structures while increasing accuracy (Forno, C., et al., 1991).

The image correlation process is generally broken down into two parts, the detector and the descriptor. The detector process is meant to consistently detect interest points such as corners, blobs, and T-junctions. The ability of the detector should be robust with respect to changes in viewpoint. The neighborhood of the selected features is represented as feature vectors or descriptors. Ideally, captured sections should represent the most distinctive features. The descriptor is then compared and matched with different images. There are various algorithms that achieve this with varying results. Some algorithms process the images quickly (i.e. lower computational cost) with low accuracy while others require higher computation power but are more reliable.

The main objective of this study was to develop a preliminary algorithm to detect and track features in sequential images (or frames) of a concrete surface in laboratory conditions to estimate the surface displacement and deformations. The initial algorithm was evaluated with different image resolution and quality under different lighting conditions and various surface annotation. The optimum algorithm was then partially validated using a digital strain gauge during a compression test. The following sections include the details of algorithm development as well as discussion of preliminary results.

5.4 Methodology

For this research Speeded-Up Robust Feature (SURF) combined with and Binary Robust Invariant Scalable Keypoints (BRISK) methods were employed in order to achieve a robust algorithm for multiple applications. The initial detector-descriptor algorithm was SURF which is based on the Hessian matrix concept. Utilizing integral images, computation time can be reduced. Although the detector implements the Hessian matrix, computation is improved by utilizing the determinant of the matrix for the scale and location. The descriptor is then composed of a distribution of Haar-wavelet responses within the neighborhood of the interest point. The Haar-wavelet is a rescaled sequence of square-shaped wavelets utilized by SURF to detect contrast in dark and light pixels from left to right, and top to bottom (Herbert et al., 2006). The BRISK algorithm utilizes a scale-space key point detector, key point descriptors, and matching algorithm for feature detection. The BRISK sampling patterns are concentric circles used to construct pairwise brightness comparison which help in increasing processing speed (Leutenegger, S., et al., 2011). Attempts to improve image quality through better lighting impacted the results of SURF and BRISK methods due to

changes in lighting contrast. The algorithm utilizes the Hessian matrix H(x, σ) to determine instance in images where there is a change in lighting. Given a point x = (x, y) in an image I, the Hessian matrix H(x, σ) in x at scale σ is defined as follows (Herbert et al., 2008):

$$H(x,\sigma) = \begin{bmatrix} L_{xx}(x,\sigma)\, L_{xy}(x,\sigma) \\ L_{xy}(x,\sigma)\, L_{yy}(x,\sigma) \end{bmatrix} \quad (1)$$

where $L_{xx}(x,\sigma)$ is the convolution of the Gaussian second order derivative $\frac{\sigma^2}{\sigma_x^2} g(x)$ with the image *I* in point x, and similarly for $L_{xy}(x,\sigma)$ and $L_{yy}(x,\sigma)$.

Assuming that the reference pixel in the original frame is located at (x_0,y_0) and the point of interest at the location of (x_i,y_j), after deformation and displacement of the concrete surface, these two point will be relocated to (x'_0,y'_0) and (x'_i,y'_j), respectively. The correlation between the aforementioned points can be expressed as follows (Jin, H., et al., 2008):

$$x'_i = x_i + \alpha(x_i, y_j) \quad (2)$$

$$y'_j = y_j + \alpha(x_i, y_j) \quad (3)$$

where α and β are the displacement mapping or shape functions. Assuming a rigid body transition, the following equations can be used to represent the deformed location of the interest points in terms of $\Delta_x = x_i - x_0$ and $\Delta_y = y_j - y_0$ (Gongkang, F., and Moosa, A. G., 2002):

$$\alpha_2(x_i, y_j) = a + a_x\Delta x + a_y\Delta y + 0.5a_{xx}\Delta x^2 + 0.5a_{yy}\Delta y^2 + a_{xy}\Delta x\Delta y \quad (4)$$

$$\beta_2(x_i, y_j) = b + b_x\Delta x + b_y\Delta y + 0.5b_{xx}\Delta x^2 + 0.5b_{yy}\Delta y^2 + b_{xy}\Delta x\Delta y \quad (5)$$

where *a* and *b* are directional displacement components of the reference interest point in *x* and *y* directions, respectively. The first and second order gradients of the reference are denoted as subscript of *x* (or *y*) and *xx* (or *yy*), respectively. Figure 5.4.1 shows a schematic of the BRISK algorithm.

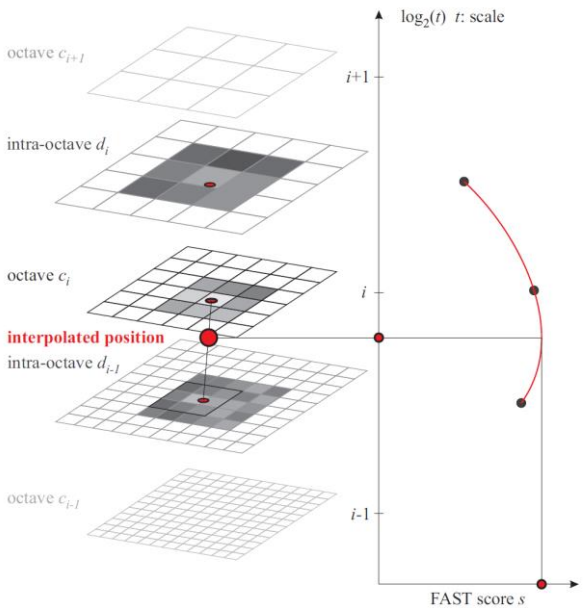

Figure 5.4.1 Detection and tracking of the interest point between image octaves using Binary Robust Invariant Scalable Keypoints (Erkel, A., Pattynama, P., 1998).

In this study, an algorithm was developed to detect and extract the features of interest from a series of images to estimate the surface displacement on a cylindrical specimen undergoing compression test. This algorithm deconstructs the video into individual images (frames) that are later scanned and checked for feature detection. Black dots on the surface of each sample were designated features to be detected. The surface area of the concrete sample was painted white to reduce the color distortion caused by concrete surface cavities and texture. Black dots were then marked on the painted surface to use as reference features for tracking during testing. Different detection methods, such as gridded dots and speckle patterns, were explored. Gridded dots consisted of a collection of hand drawn black dots in a specified matrix form with varying spacing size. Speckle patterns were sprayed on using a spray can and the speckles were randomly applied on the specimen surface. Figure 5.4.2 illustrates examples of speckled and gridded dot surfaces prepared for the image acquisition process.

(a)

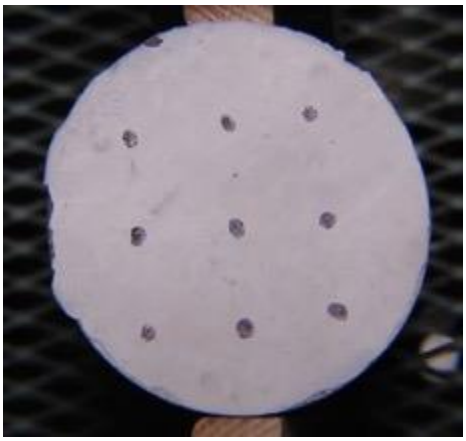

(b)

Figure 5.4.2 Preparing the surface of concrete sample: (a) Speckle paint, and (b) Matrix format.

For testing purposes, optimal environment settings were set to increase the ability to detect features. A digital camera capable of recording 30 frames per second at 1080p quality were used in this study to ensure that the number of pixels available for analysis are optimized. Stability is required to reduce the effect of noise in measuring displacements, however minor ground motion was inevitable. Optic Lens was utilized to further focus on the specimen at a safe distance in order to avoid damaging the camera during compression test while increasing size of focused image. The lens assists in optimizing the number of pixels available per frame. Lighting is controlled throughout the process with an LED source to ensure consistency. Placement of lighting source was at an angle to reduce reflection off the concrete sample surface which negatively effects the detection process. Figure 5.4.3 shows the laboratory setup for image capturing process.

Once the video is recorded, it is divided into individual frames for analysis. The algorithm then compares before and after images to determine the surface displacement and deformation by tracking the points of interest in the consequent images. The images would be cropped to focus on the interest area to reduce the number of false feature detection. A false detection could occur at edges where light and dark contrast are significantly higher. A base frame was analyzed to determine the initial locations of each feature on the specimen surface to create a matrix of interest points. Upon completion of the analyses, the strain along x and y directions were calculated and visualized in either a graph or a heatmap format. The image capturing process was performed at a frequency of 30 frames per seconds.

Figure 5.4.3 Setup for image capturing process.

5.5 Data Processing and Analysis

Data was collected from cylindrical concrete samples prepared in the laboratory. Upon preparing the concrete surface for gridded or speckled marking, the specimens were capped and undergone a compression test at a constant loading rate. The imaging apparatus was setup to capture consequent images of the testing process for further analyses. Upon completion of the test and retrieval of images, the initial feature detection algorithm was performed on the series of captured images. Figure 5.5.1a illustrates the results of an initial feature detection process that was performed on a frame during testing. Figure 5.5.1b shows a series of features that were located and annotated by the algorithm on one of the initial frames. An area of interest was identified by the user to focus the feature detection and tracking within a specified area of the sample surface. One of the advantages of this algorithm over conventional strain measurement devices is that the user is able to track the movement of many specified points on the surface during the test. Figure 5.5.2 shows the images extracted from different stages of the compression test at different focus settings. The algorithm was able to plot a movement trajectory for all the point of interest on the specified images. This features enables the user to track and monitor the surface displacement at almost every point on the specimen surface during testing. The plots of accumulated strain in x-direction at 9 points of interest on the surface were illustrated in Figure 5.5.3. This could be due to false detection of features between some frames during the analysis period. Improving the lighting conditions and better preparation of surface before testing will reduce the possibility of false positives.

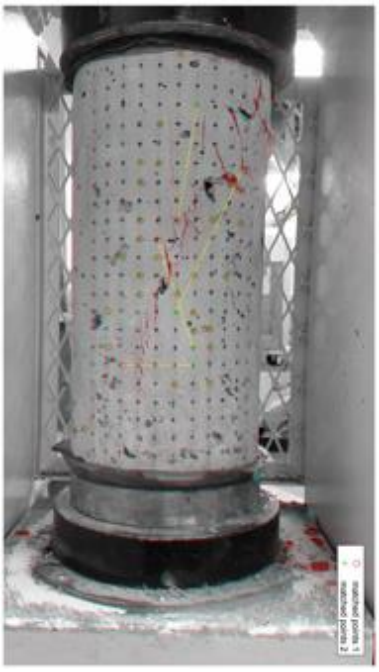

(a)

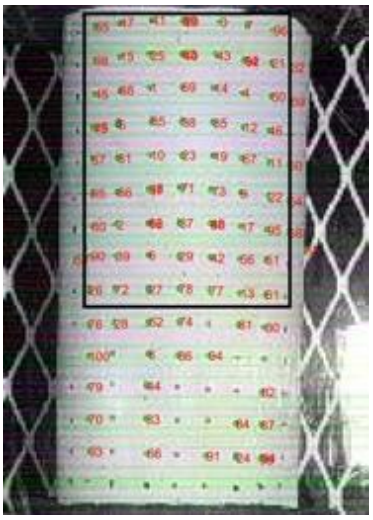

(b)

Figure 5.5.1 (a) Detection and matching the image features, and (b) Annotating points of interest and cropping the selected section for displacement monitoring.

Figure 5.5.2 Trajectory of detected features on the concrete surface.

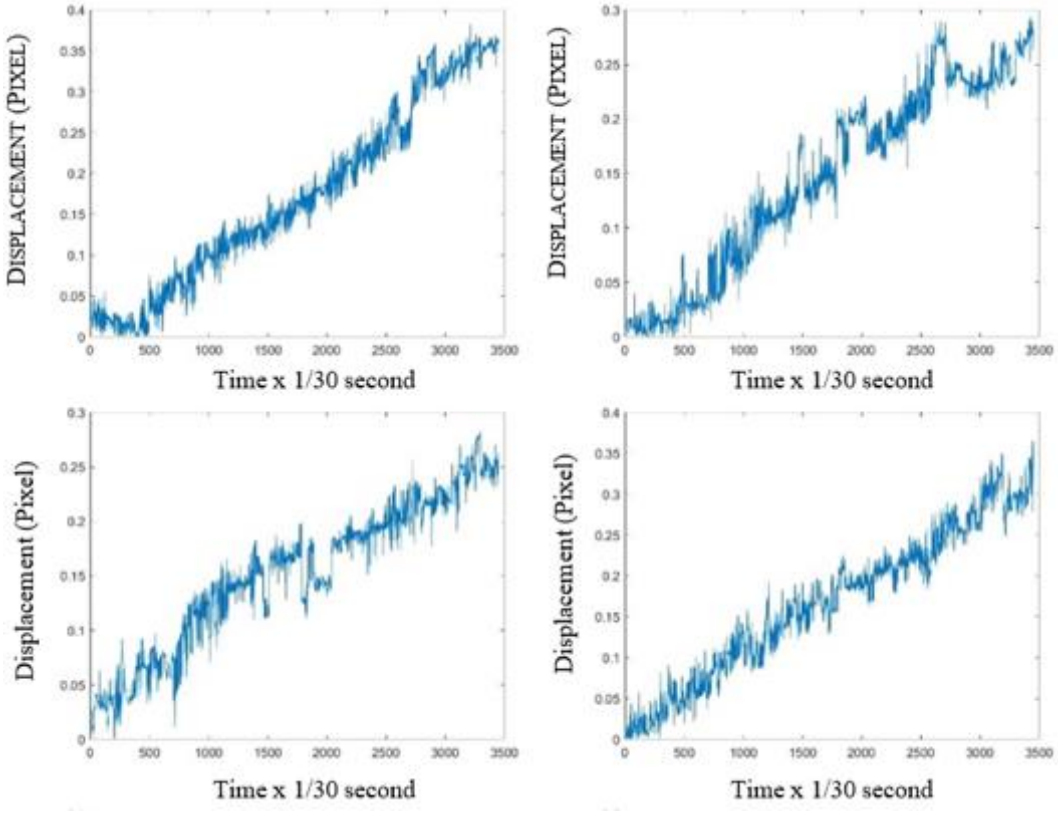

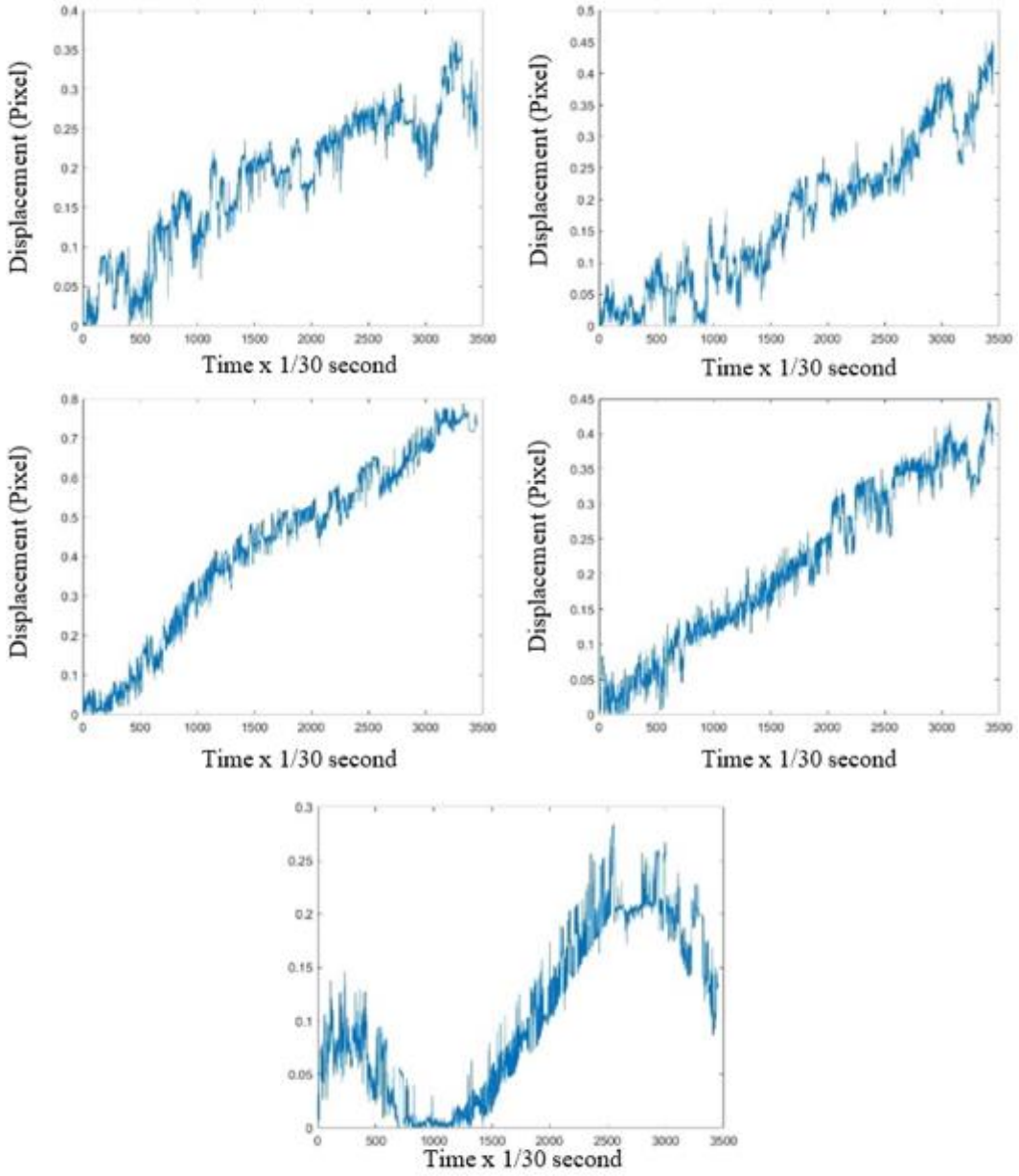

Figure 5.5.3 Accumulated strain along x-direction for different points of interest on specimen surface. (Y axis: displacement in Pixel, X axis: Time x 1/30 of second)

The displacement signal obtained from the initial analyses of the images also reflect some noise due to the missing features or proximity of pixels during the analysis. These noisy signals could be smoothened using a moving average or other smoothing algorithms to produce a more uniform response.

To better represent the trend of developing displacements and surface deformations from the image correlation algorithm, a nested interpolation of strain data was performed on the specimen surface that was captured during imaging process. Superimposing the contour plots of surface

deformation during the testing period, generates an animated representation of strain development on the sample surface in form of a heatmap. Figure 5.5.4 illustrates a screen captured of the animated strain heatmap during the compression test. The lighter areas in these figures represent higher strains and in some locations cracking of the specimen surface. A higher resolution of this heatmap enables the user to extract meaningful information regarding the crack initiation and propagation on the concrete surface under loading conditions.

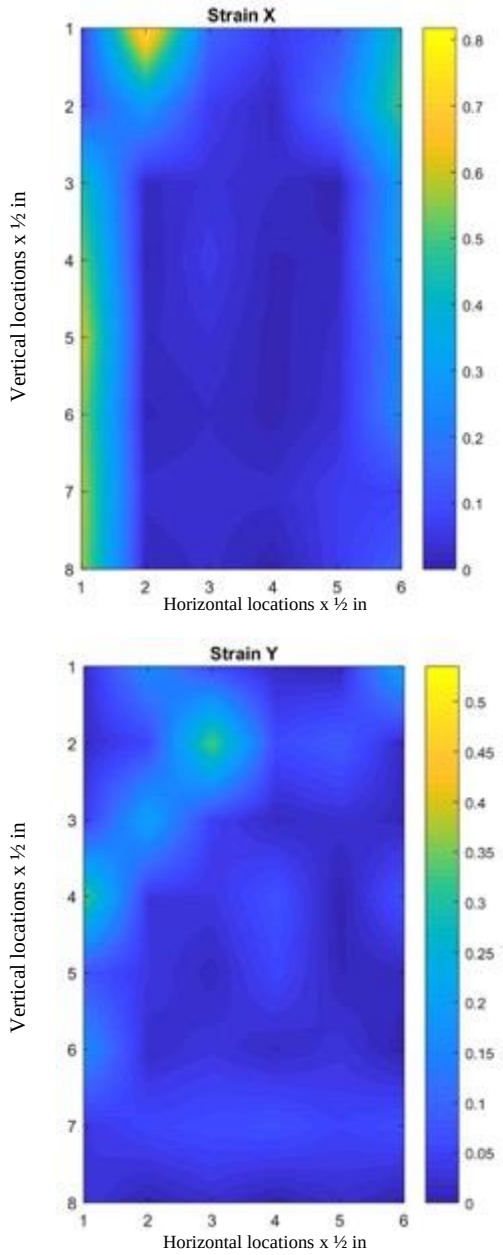

Figure 5.5.4 Heatmap of strain measurement in the x- and y-directions.

The next step in this study was to partial validate the results of image correlation algorithm with measured deformations using mounted local strain gauges. To perform the validation process, two linear strain gauges were installed on a frame around the cylindrical specimen to measure the extension and compression of the sample during the compression strength test. At the same time, the image capturing device was setup to acquire images of the sample during the testing process. The strain values calculated from both image correlation algorithm and strain gauge data were plotted on a stress-strain graph to compare the results. Within a reasonable accuracy range, the results of strain measurements from image correlation algorithm are comparable to those captured by digital strain gauges. Figure 5.5.5 shows the results of this partial validation. A more in-depth validation and calibration process are undergoing. The discrepancy between measured and estimated displacements in these figures is mostly due to the unmatched timing of the image capturing process and the unsynchronized frequency of data collection between the gauge and image correlation algorithm. The more in-depth validation of the results from this algorithm is undergoing.

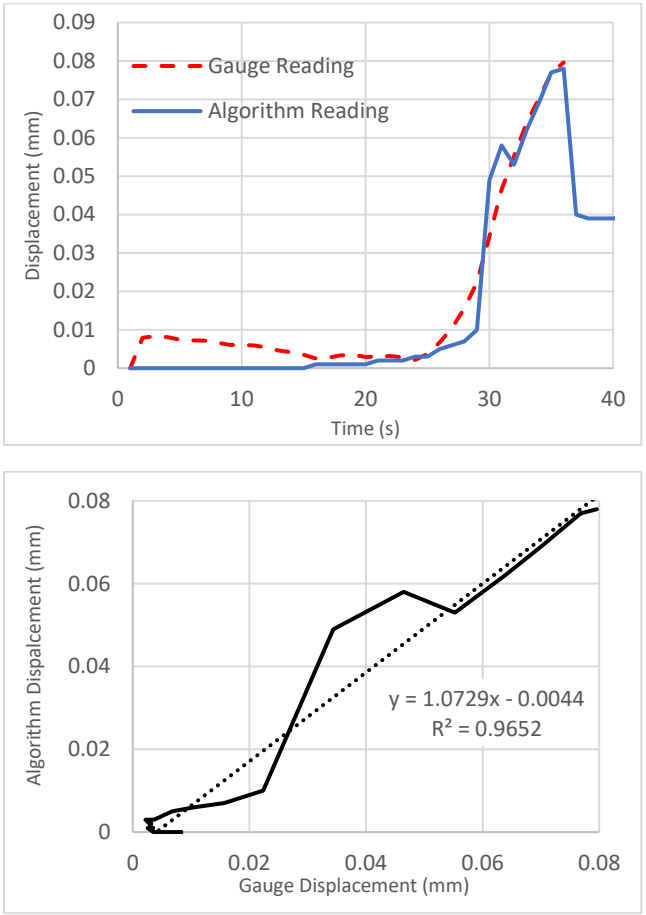

Figure 5.5.5 Displacement measurement comparison between gauge reading and algorithm calculation.

A preliminary version of an image correlation algorithm was developed to capture the surface properties of concrete samples in the laboratory conditions. The accuracy of the developed algorithm is dependent on the stabilization of the image capturing device, lighting source and preparation of surface for proper feature detection. The preliminary results show potential of using this non-contact method to estimate the surface deformation and displacement of concrete samples. Based on current version of the algorithm, it can be observed that the strain measurements are relatively close to those measured from a digital gauge. Further improvement is being explored in terms of increasing accuracy and speed of calculations. Further investigation into factors that can improve detection of features will improve accuracy of the algorithm.

CHAPTER 6 – AN OPTIMIZED IMAGE PROCESSING TECHNIQUE FOR DETECTION OF CONCRETE SURFACE DEFECTS

6.2 Introduction

Crack initiation and propagation can reduce bearing capacity and durability of concrete structures. It is crucial to inspect the condition of a structure over its life cycle to ensure the structural health and avoiding costly repairs. Digital Image Processing is one of the non-contact methods that can measure features of a crack without the subjective variability of direct measurement by human (Gastineau, A., et al. 2009). Additionally, this approach allows to investigate parts of structural elements, which can be difficult to access (such as underwater structures and bridges) (Structural Health Monitoring Solutions, 2019). Automated crack detection techniques can also save time and costs compared to the traditional visual inspection methods (Abdel-Qader, I., et al., 2003). Despite the convenience that digital image processing provides, it has been associated with challenges regarding the crack detections mainly because of the complexity of the process and the required accuracy level. The following section provides a summary of literature relevant to various image processing algorithms that have been used for crack and defect detection.

6.3 Background

Crack initiation and propagation can reduce bearing capacity and durability of concrete structures. It is crucial to inspect the condition of a structure over its life cycle to ensure the structural health and avoiding costly repairs. Digital Image Processing is one of the non-contact methods that can measure features of a crack without the subjective variability of direct measurement by human (Gastineau, A., et al. 2009). Additionally, this approach allows to investigate parts of structural elements, which can be difficult to access (such as underwater structures and bridges) (Structural Health Monitoring Solutions, 2019). Automated crack detection techniques can also save time and costs compared to the traditional visual inspection methods (Abdel-Qader, I., et al., 2003). Despite the convenience that digital image processing provides, it has been associated with challenges regarding the crack detections mainly because of the complexity of the process and the required accuracy level. The following section provides a summary of literature relevant to various image processing algorithms that have been used for crack and defect detection.

Background

Abdel-Qader et al. (Abdel-Qader, I., et al., 2003) compared 4 crack detection techniques: Sobel, Canny, Fast Haar Transform (FHT) and Fast Fourier Transform (FFT). The Sobel operator (Duda, R., Hart, P., 1973) uses two 3×3 convolution matrices in order to magnify the difference between edges in gradient intensity image. As Equations 1 and 2 describe, the first matrix convolves in x direction to detect vertical edges and the second one in y direction to detect horizontal edges:

$$G_x = \begin{bmatrix} -1 & 0 & +1 \\ -2 & 0 & +2 \\ -1 & 0 & +1 \end{bmatrix} * A \qquad (1)$$

$$G_y = \begin{bmatrix} -1 & -2 & -1 \\ 0 & 0 & 0 \\ +1 & +2 & +1 \end{bmatrix} * A \quad (2)$$

where A is the source image.

Each matrix has two effects: smoothing and central difference effect. The smoothing effect, smoothens the perpendicular direction that matrix is applied and the central difference, bolds the edge in the derivative direction. Equations 3 and 4 represent these two effects:

$$h(-1) = 1, h(0) = 2, h(1) = 1 \quad (3)$$

$$h'(-1) = 1, h'(0) = 0, h'(1) = -1 \quad (4)$$

As a result, the convolution matrices (kernels) convert the whole image into distinguishable edges. 'Canny' is another edge detector with more complexity which initially uses Gaussian mask to remove noise and then using the intensity gradient of the image, applies non-maximum suppression with double threshold and final suppression to remove unwanted edges that are not connected to the strong edges (Canny, J., 1986). In Abdel-Qader et al.'s paper (Abdel-Qader, I., et al., 2003), two types of images were compared together: images containing cracks vs non-crack images. They used a threshold value, which was calculated based on the average intensity value of all pixels of the crack images. Based on the results, the 'Sobel' edge detection was only able to detect 68% of the cracks mainly because of the unsmooth surface of the concrete elements. They recommended that the algorithm needs improvement to be able to be accounted as a reliable crack detection method. On the other hand, the 'Canny' technique had 76% accuracy which was attributed to the noise reduction filter. It is can be concluded that 'Sobel' operator needs to be combined with noise reduction filters to achieve higher accuracy levels.

In 2010, Fujita and Hamamoto (Fujita, Y., Hamamoto, Y., 2011) published an automatic crack detection method for concrete surfaces based on two pre-processing and two processing steps. Initially, the pre-processing step included subtraction process in two different ways: One could receive two images as input and subtract one from another. In the other approach, one image was considered as the only input and a constant value was subtracted from all the image's pixels (Fisher, R., et al. 2019). Fujita and Hamamoto (Fujita, Y., Hamamoto, Y., 2011) used the single image subtraction and then multi-scale line filter was coupled with the Hessian matrix to help with line detection, induced blebs and stain removal effects. In the processing part, probabilistic relaxation and locally adaptive thresholding used for labeling purposes and crack detection improvement, respectively. The algorithm was applied to more than 60 images of concrete surface. Then, Receiving Operating Characteristic (ROC) analysis was utilized in order to evaluate the pre-processing steps. ROC is able to compare different tests in order to rank their accuracy based on a target value (Erkel, A., Pattynama, P., 1998). The targets in their study were sensitivity and specificity defined by Equations 5 and 6:

$$T_p = \frac{N_{td}}{N_c} \quad (5)$$

$$F_n = \frac{N_{fd}}{N_b} \quad (6)$$

where T_p is the true positive fraction equal to the ratio of detected crack pixels over the total number of crack pixels. F_n is the false negative fraction equal to the ratio of detected pixels that are not in the crack region to the total pixels that are considered true background. The authors concluded that the proposed method of combination of two steps in pre-processing has higher Area Under Curve (AUC) value compared to the scenario in which only one of the steps were used. Additionally, by using ROC sensitivity or specificity, the authors were able to compare the combination effect of probabilistic relaxation and adaptive thresholding versus global thresholding.

Similar to previous study, Hoang (Hoang, N., 2018). proposed a crack detection method in two steps of pre-processing and processing. The study emphasized that an image enhancement is necessary because the brightness of the environment can change at different locations and the surface texture of the concrete is not typically free from noises. The developed technique was introduced as Min-Max Gray Level Discrimination (M2GLD) to prepare the image as a pre-processing step. M2GLD changes the gray intensity of the crack and non-crack pixels. Then Otsu algorithm is used to binarize the image followed by two other cleaning steps. The cleaning process consists of removal of the objects with lower number of pixels and an Axis Ratio Index (ARI) which ranges from 0 (elongated object) to 1 (circular shaped object). The Otsu method (Otsu, N., 1979) is a technique that allows extracting objects from their background by using a gray scale histogram. The histogram is made of probability as the y-axis and the intensity as the x-axis. A threshold value categorizes pixel intensities in two classes in a way that if all pixels in the first class turn into a similar intensity and all pixels in the second class turn into another similar intensity, then the objects are still distinguishable.

If class one and two have variance of σ_0^2 and σ_1^2 respectively and the probabilities of these two classes are ω_0 and ω_1, then, Otsu algorithm searches for a threshold value (t) that minimizes the within class variances (Equation 7):

$$\sigma_\omega^2\,(t) = \omega_0(t)\sigma_0^2(t) + \omega_1(t)\sigma_1^2(t) \quad (7)$$

Simultaneously, maximization of the Equation 8 can result in the same threshold value (t):

$$\sigma_b^2\,(t) = \sigma^2 - \sigma_\omega^2(t) = \omega_0(t)\omega_1(t)[\mu_0(t) - \mu_1(t)]^2 \quad (8)$$

Where μ_0 and μ_1 are mean values of each class. Finding the threshold value not only binarize the image, but also magnifies the edges and helps with the object detection. In Hoang's research (Hoang, N., 2018). , cracks in four images were accurately detected and the comparison to the standard 'Otsu' method showed that the proposed pre-processing has a critical role in improving the accuracy of the algorithm. However, in this approach, the user must deal with four manually defined parameters in pre-processing and image cleaning process. These values will change from one material to another and then, empirical adjustment is required.

Lou et al. (Lou, Q., et al. 2019) presented an approach for automatic crack detection to eliminate the parameter dependency and reducing the processing time. They designed a Finite State Machine (FSM) operator that can search for features of a valley in grayscale curve of an image. Sudden changes such as a valley is attributed to the cracks. Similar to the 'Otsu' method, this technique relies on a threshold value (H) which is the minimum height of the valley and the height of both starting and ending points which must be greater than H value in order to be considered as a crack. Along with H value, finding the exact starting and ending point is crucial for an accurate crack detection. The authors compared sensitivity, precious and computation time of the proposed approach with M2GLD and Lee's Otsu (Lee, B., et al. 2013) approaches. According to their result, M2GLD and Lee's Otsu have high sensitivity but low accuracy and accordingly higher time-consuming process. In contrary, FSM had lower sensitivity but higher accuracy and speed. As a limitation of this approach, the authors mentioned that the dirtiness of the surface can result in false crack detection due to the lower sensitivity compared to Lee's Otsu and M2GLD approaches.

Li et al. (Li, L., et al., 2018) used local-binarizing algorithm to detect cracks on a concrete surface when aggregates are exposed. Local binarization is based on Otsu binarization method. In this technique, an image is converted to multiple windows and for each window, a threshold is calculated separately rather than using an overall threshold of the image. Following the local thresholding, extraction of cracks conducted by searching for pixels with only one pixel connection and the eight pixels in isolation condition in a 3×3 table. Finally, morphological operation applied to the processed image to thin the extracted cracks with one pixel width. Then from the thinning operation, it was possible to identify terminals and branches on each crack based on the number of nonzero pixels. According to the results, the proposed method was able to ignore the effect of aggregates on the surface of the concrete. The size of the windows was recommended to be two to three times of the maximum crack's width to obtain optimized results. However, in some cases, the cracks were less visible. Thus, the authors recommended to combine algorithm parameters such as smaller local threshold and window size to increase the sensitivity.

Review of literature indicate that each proposed method has its own advantages and disadvantages. From the accuracy level to the computation speed and the simplicity of the algorithm or the required equipment, all can be manipulated by using different filtering operators, edge detectors and object detectors. Despite the advancement of the methods, there is not yet any algorithm that being achieved 100% accuracy level in crack recognition (Mohan, A., Poobal, S., 2018). That implies the necessity of continuous algorithm development in order to improve the previous efforts. To achieve this objective, this research has proposed a simple yet efficient method which requires minimum user effort to reach acceptable crack detection accuracy. In the following sections, the methodology of the algorithm is described.

6.4 Methodology

The proposed method consists of four main steps: image acquisition, preprocessing, processing and crack feature extraction. Figure 6.4.1 shows the flowchart of this method. In the following parts, the details of each step are explained.

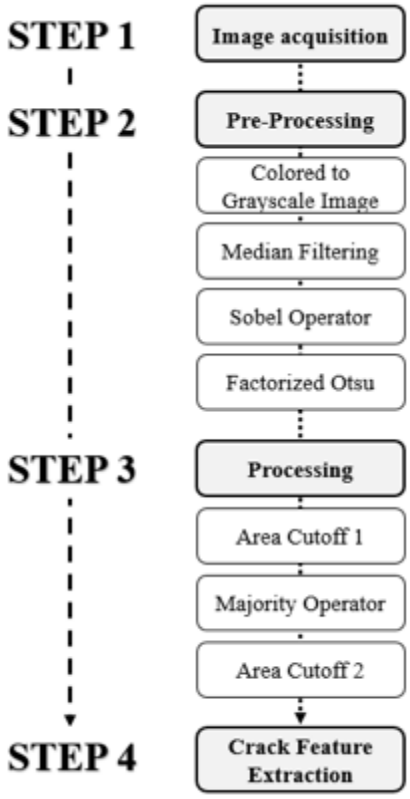

Figure 6.4.1 Flow chart of the proposed method.

6.4.1 Image acquisition

In order to assess any crack detection algorithm, it is necessary to find elements that are already containing cracks or capture images during crack propagation. In this study, cylindrical samples made from Self Consolidating Concrete (SCC) were monitored during compressive strength test. (ASTM C39/C39M, 2018) The camera used in this study is a Canon EOS Rebel T6. A constant setup position including a fixed height and distance were considered for all image acquisitions to ensure the consistency of the tests. The acquired pictures were cropped manually to focus on the sample rather than the environment.

6.4.2 Preprocessing Steps

6.4.2.1 Grayscale and median filtering

The first step in image preprocessing is to convert colored images to grayscale images composed of 256 different levels of gray. Then, the median filtering used to initially smooth the texture and eliminate holes, different shades of gray and non-cracked abnormalities. Median filtering also known as “salt and pepper noise remover”, is very effective when the purpose is edge preservation. (MathWorks, 2019)

6.4.2.2 Edge detection

A comparison test was then conducted between two edge detectors, Sobel and Prewitt operators to develop the most accurate algorithm. Prewitt operator uses the same concept similar to Sobel

operator but with slightly different convolving matrices. Equation 9 and 10 represent the convolving matrices in x and y directions:

$$G_x = \begin{bmatrix} -1 & 0 & +1 \\ -1 & 0 & +1 \\ -1 & 0 & +1 \end{bmatrix} * A \tag{9}$$

$$G_y = \begin{bmatrix} -1 & -1 & -1 \\ 0 & 0 & 0 \\ +1 & +1 & +1 \end{bmatrix} * A \tag{10}$$

These two matrices show that Prewitt operator has less smoothing effect compared to Sobel operator and that makes it more sensible to the texture noises.

6.4.2.3 Image thresholding

In the next step, Otsu thresholding technique is utilized to binarize the grayscale image and differentiate background and foreground pixels. To find the threshold value, a global threshold T is extracted from the grayscale image (named ‘’edge’’), using Otsu's method. The returned scalar T is a value between 0 and 1. Then, the grayscale image turns into a binary image. Figure 6.4.2 is an example of using Otsu thresholding method. Although the binary image visually looks fine and the cracks are apparent, the problem shows up when the image is zoomed in. It can be clearly seen that most of the crack lines are not connected. The proposed method factorizes T-value in order to achieve a strong connection between crack line in a way they were connected on the sample. This factor is represented by parameter a in the following equation:

$$BW(x;y) = \begin{cases} 0 \; if \; I(x;y) < a * T \\ 1 \; if \; I(x;y) \geq a * T \end{cases} \tag{11}$$

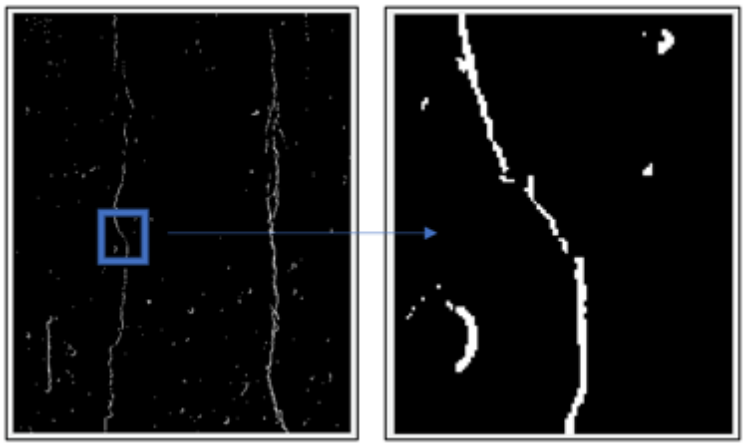

Figure 6.4.2 Unconnected crack when using T

After achieving desired results by applying this technique, it is only required to use morphological operations to reduce the overall noises.

6.4.3 Processing step

One of the major problems in automatic crack detection is classification between cracks and other linear patterns on concrete, such as member edges, background lines, paint or oil stains etc. Therefore, to separate cracks from irrelevant objects, multiple techniques are utilized as following:

6.4.3.1 Area cut-off 1

At this point, images may have small patterns due to the surface unevenness. To remove these patterns, an area threshold was applied on the binary image. First, a matrix containing the objects found in the binary image is created. Then, the 'Area' property is estimated. The number of pixels for each object was calculated and the area of each object was estimated. The objects with an area less than 200 pixels would be added to the background pixels. Figure 6.4.3 shows the results on a sample image.

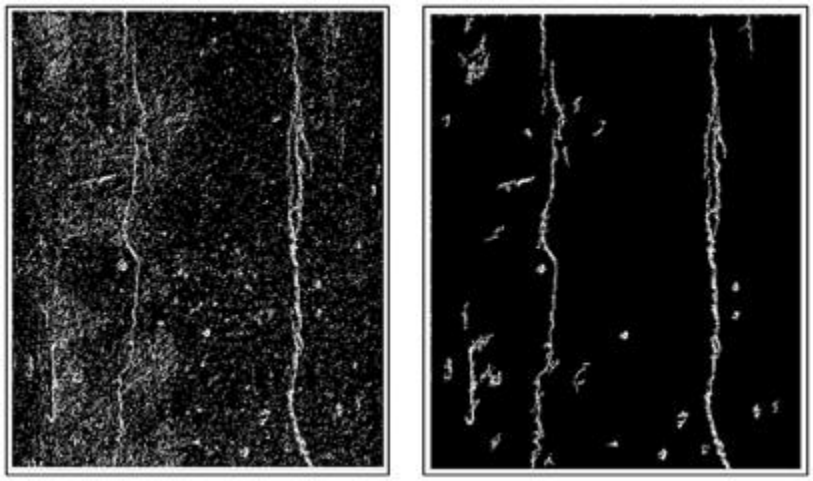

Figure 6.4.3 Area cut-off 1, before (left) and after (right)

6.4.3.2 Margin Remover

Since the algorithm may detect margins of the image as a crack, it is necessary to find a solution to remove these false detections. Cracks do not appear as a straight line on a concrete surface. Therefore, by using "Orientation" property, any object with orientation of 0, -90 and 90 are identified and added to the background.

6.4.3.3 Crack connectivity

Using all previous operations including preprocessing steps can discretize or change the cracks connections. To address this issue, another morphological operation "majority" is applied. It uses a 3 × 3 pixels structure going through the picture. If 5 or more pixels in the 3 × 3 structure element have the value of 1 (target pixel), the pixel in the center of the mask is set to 1. Otherwise, the code

sets the value to 0 (background pixel). This majority operation is repeated until the current resultant image is the same as the previous resultant image.

6.4.3.4 Area cut-off 2

To remove the last unwanted objects from the morphological operations, a manual area cut-off input box appears on the screen and the user can select the desired number of pixels in which an object will convert to the background pixels.

6.4.3.5 Crack detection

Crack detection has been done in two steps. The first step was tracing the margins of each crack in a binary image and returning a cell array of boundary pixel's locations. In this case, the cell array is named "blobs" and the pixel locations are sets of coordinates. Then, the plot function is used to plot outline over the blobs (Figure 6.4.4).

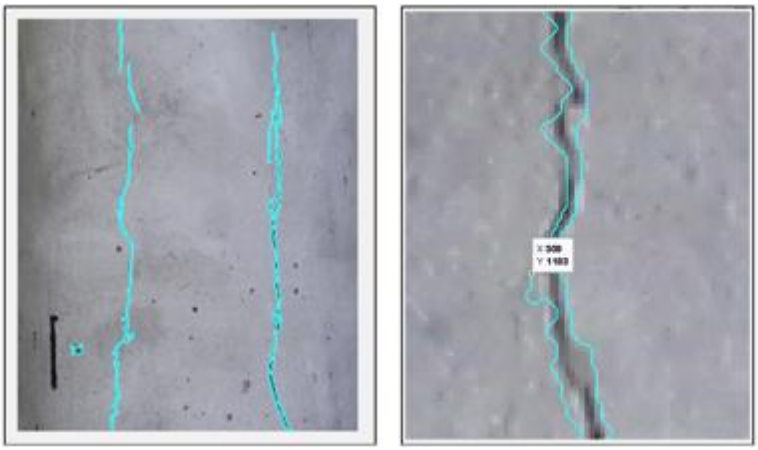

Figure 6.4.4 Plotted borders of all cracks

6.4.3.6 Crack labeling

Figure 6.4.5 shows 8 cracks that have been detected with different colors. To avoid the scenario where a color would be used twice, the cracks were labeled with numbers.

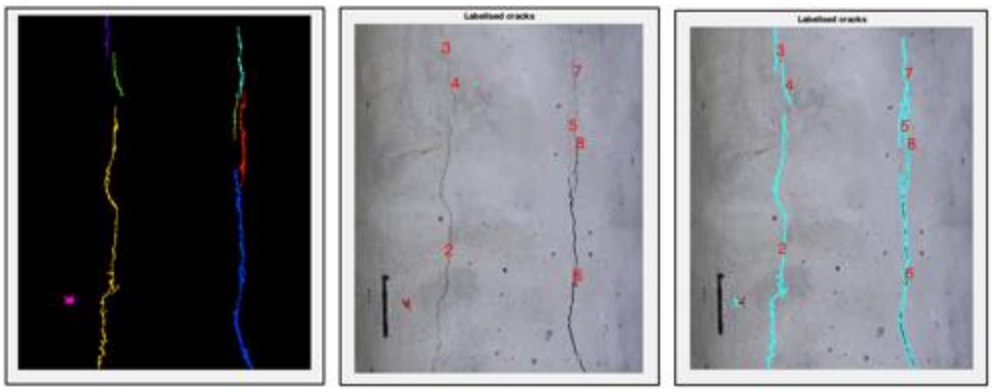

Figure 6.4.5 Crack labeling with colors and numbers

6.4.4 Crack features extraction

Before having crack properties in the international system of units, these properties should be measured in pixels. Indeed, pixel is the unit used while working on image processing.

6.4.4.1 Measuring the actual length

To evaluate the accuracy of the automatic length calculations, the actual length of the cracks were manually measured by retrieving the location of several pixels on each crack. Then, the maximum length is calculated based on the previous part.

6.4.4.2 Measurements of the area

The area of each crack has been calculated by returning measurements for the set of properties specified by "properties" for each object in the binary image, BW.

6.4.4.3 Calculating the average width

The width of a crack is not a constant value along the crack propagation. Therefore, it was only possible to obtain an average value for each crack. To calculate the average width, the Equation 13 was utilized:

$$averageWidth = {}^{surface}/_{MaxDistance} \quad (13)$$

6.4.5 Calibration function

Since the data are stored as pixels, it is necessary to convert them to distances and calibrate the conversion method based on a known distance. To convert pixels to millimeters, a spatial calibration is required. If the length of an element on the sample is known, it can be compared to all other elements by a factor. A reference line with pre-measured length was drawn on the bottom left side of the all samples. Then by manually drawing a line over this mark, the factor that converts the number of pixels to mm can be obtained. In order to check the accuracy of the pixel selection during drawing a line, a comparison is performed between zoomed condition versus non-zoomed image.

6.4.6 Receiver Operating Characteristic (ROC)

To find out the most accurate factor, receiver operating characteristic curve (ROC) was utilized. ROC can show how a classifier system can change by adjusting the thresholds and selecting different operating points. The ROC space consists of false positive rate (FPR) also known as (1-specificity) on the x-axis and true positive rate (TPR) also known as sensitivity on the y-axis. The perfect classification is on the top left corner of the space. It means that the closer to the top left corner, the better the method is. Now, let's focus on TPR and FPR and how these values are found. (Equation 14 and 15)

$$TPR\ (sensitivity)\ =\ \frac{TP}{TP + FN} \tag{14}$$

$$FPR\ =\ \frac{FP}{FP + TN} \tag{15}$$

To solve Equations 1 and 2 in order to plot the ROC curves, four different values are needed. These values are defined as following:

- TP (or T+) is true positive. It means that a crack exists on the sample and that it has been successfully detected by the algorithm.
- TN (or T-) is true negative, also known as correct rejection. It means that the algorithm has successfully identified a part of the sample as a non-existing crack.
- FP (or F+) is false positive, also known as false alarm. It means that the algorithm has detected a crack that does not exist on the sample.
- FN (or F-) is false negative. It means that a crack exists, but it has been unsuccessfully identified by the algorithm. It is what the code missed to detect.

6.5 Results and discussion

6.5.1 Preprocessing results

Sobel's mask tends to accentuate the contrast slightly more than Prewitt operator. Therefore, as it is shown in Figure 6.5.1, the cracks are slightly brighter and more connected after applying Sobel mask (right) compared to Prewitt mask (center). This explains that more edges are detected using Sobel operator. Thus, Sobel's operator was selected for the rest of the algorithm.

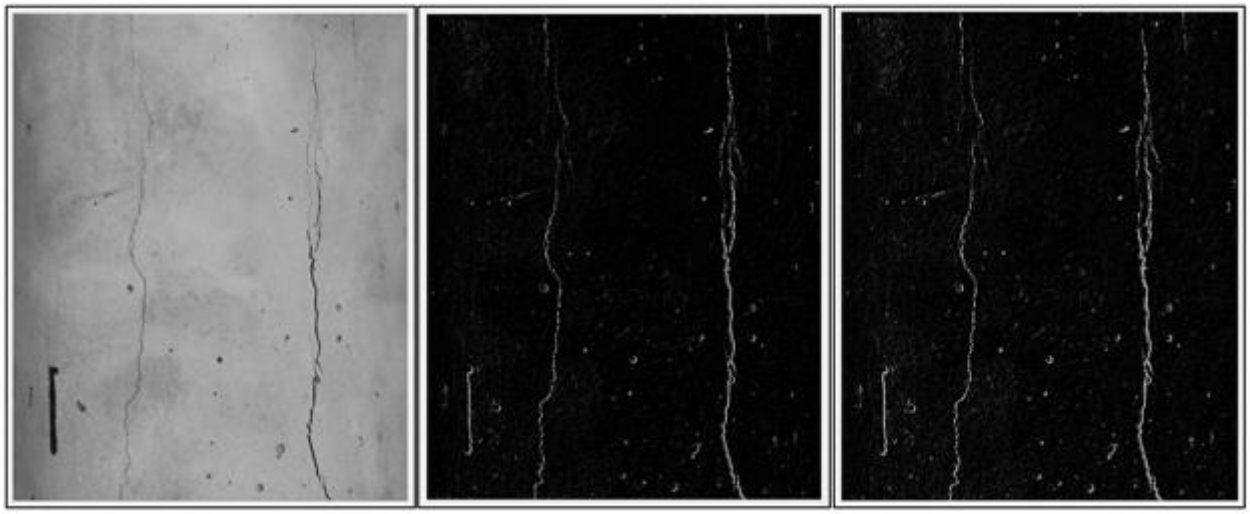

Figure 6.5.1 Processed image after using Prewit (center) and Sobel (right) operators.

As it was mentioned in previous section, Otsu's threshold value T given by MATLAB was not accurate because at the end of the calculations, many cracks were ignored and so, the obtained results were not meaningful. A factor was applied to reduce the threshold and to make cracks more visible. Different percentages were applied at each trial, starting from 10 % to 90 % and increasing by 10% intervals. Then, the results were classified based on the accuracy of the calculations. This technique was applied on four different images and the ultimate goal was to find the optimized factor to apply on T in order to be as much accurate as possible regarding the detection of cracks.

6.5.2 Visual effect of different Threshold values

This section shows the images with different factors applied to T and the corresponding results obtained after running the whole algorithm. Figure 6.5.2 and Figure 6.5.3 depicts progressively the effect of each factor. Visually, it can be observed that a factor over 30% results in loss of many cracks which indicates the threshold value is too high.

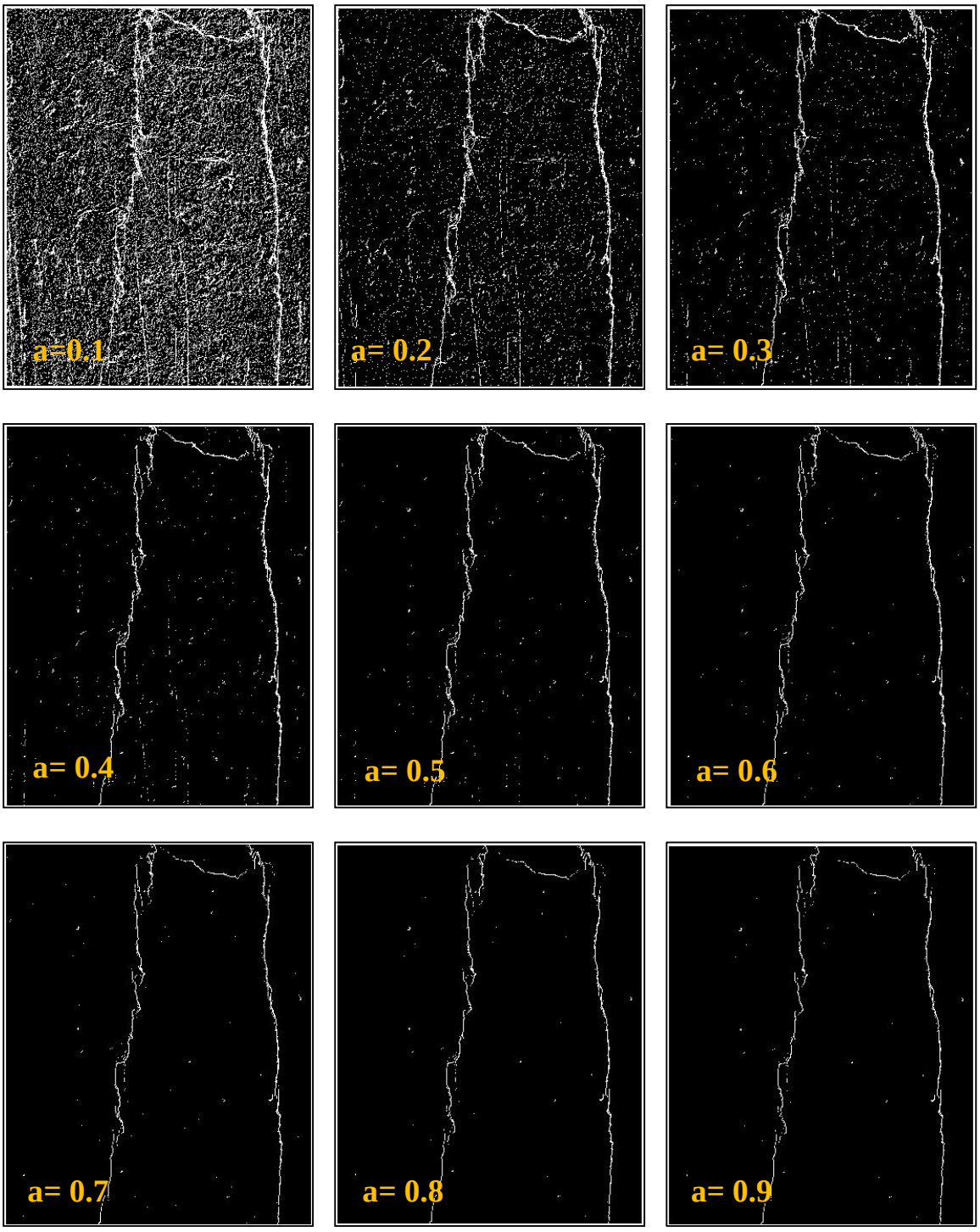

Figure 6.5.2 Different factors applied to Otsu's value

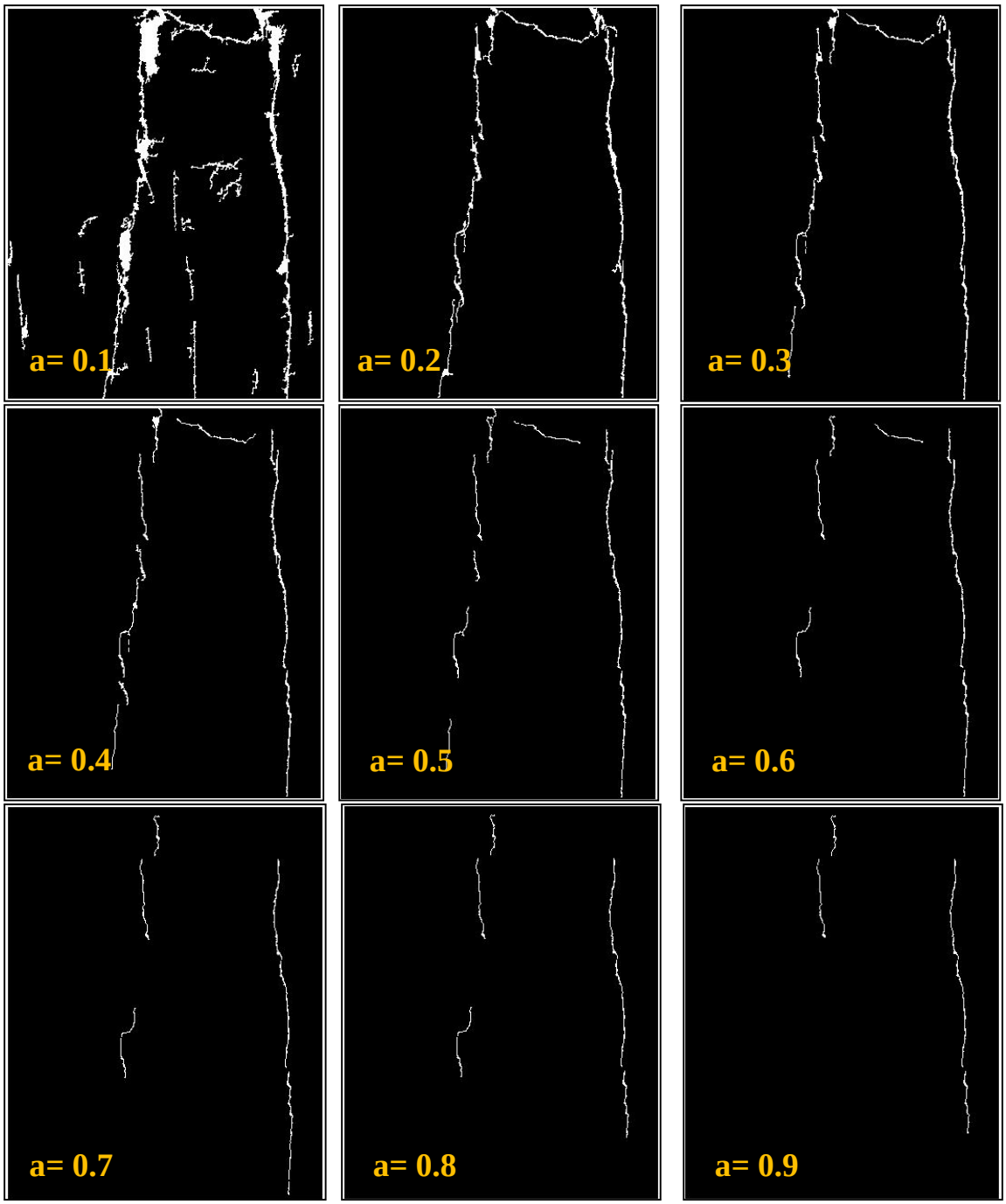

Figure 6.5.3 Results obtained at the end of the code with different factors

6.5.3 ROC analysis

As explained previously, True positive rate is the ratio of successfully detected cracks over all existing cracks. The parameter a, ranges from 0.1 to 1.0 and it was applied to the threshold value of four images from actual compressive strength test of self-consolidating concrete samples.

Table 6.5.1 and 6.5.2 show the results for image 1 and Figure 6.5.4 demonstrates the ROC curve for all four images. According to the analysis, applying parameter a = 20% of the threshold value, will result in sensitivity ranging from 69.5% to 95.9%.

Table 6.5.1 Calculated data for ROC curves (image 1 – Crack length)

% applied to T	T+	T+ rate (%)	F+	F+ rate (%)	Average Width
0.1	1410.83	0.39	1994.07	0.014	9.533
0.2	3237.28	0.90	0	0.00	8.647
0.3	2996.49	0.83	0	0.00	6.736
0.4	2760.66	0.76	0	0.00	5.38
0.5	2472.83	0.69	0	0.00	4.464
0.6	2032.19	0.56	0	0.00	4.256
0.7	1729.88	0.48	0	0.00	4.063
0.8	1544.02	0.43	0	0.00	3.958
0.9	1292.42	0.36	0	0.00	3.825
1	1082.83	0.30	0	0.00	3.563

Table 6.5.2 Calculated data for ROC curves (image 1 - area)

% applied to T	T+	T+ rate (%)	F+	F+ rate (%)
0.1	56582	288.01	14657	1.05
0.2	25471	129.65	0	0.00
0.3	18769	95.54	0	0.00
0.4	14643	74.53	0	0.00
0.5	11249	57.26	0	0.00
0.6	8776	44.67	0	0.00
0.7	7055	35.91	0	0.00
0.8	6090	31.00	0	0.00
0.9	4898	24.93	0	0.00
1	3821	19.45	0	0.00

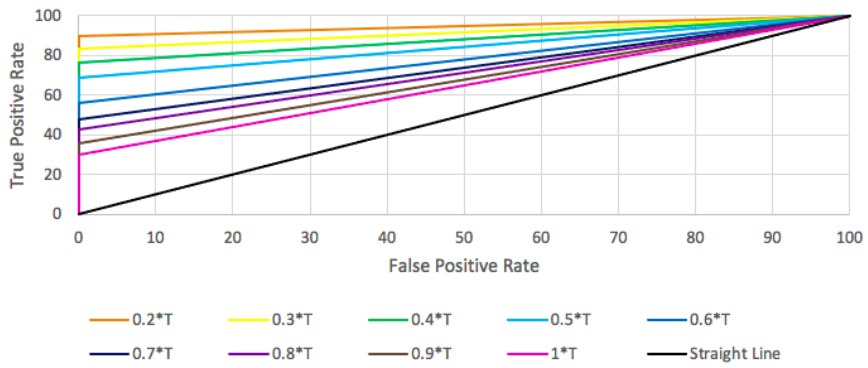

Figure 6.5.4 Sample ROC curves for estimation of crack length

The same process has performed for the detected crack's area of four images. Table 6.5.3 shows that when applying a factor of 10% and 20%, the code detects more surfaces of cracks than there truly are. In both situations, big white areas were visible due to the presence of holes on the sample's surface. With a factor of 30%, the code detects over 95% of true positive areas in image 1. Figure 6.5.5 represents all the plots.

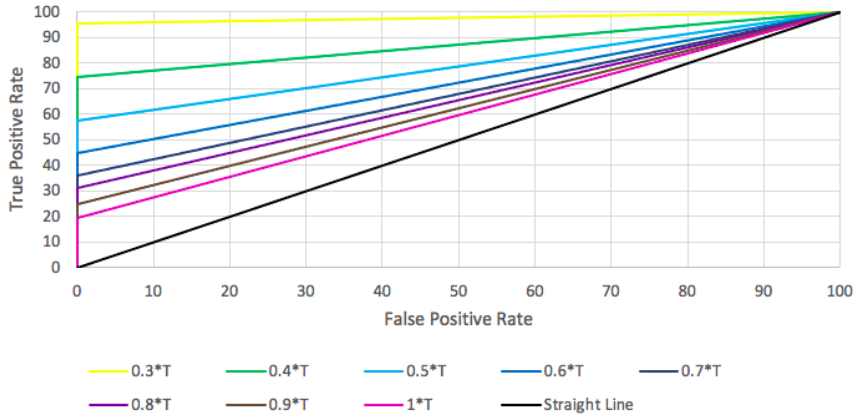

Figure 6.5.5 Sample ROC curves for the area calculation

In general, the proposed algorithm detects less cracks than the actual numbers are on the images. As some of the cracks are very close, the algorithm simply connects them together. Indeed, using the morphological operation 'majority' sets a pixel to 1 if five or more pixels in its 3-by-3 neighborhood are 1s; otherwise, it sets the pixel to 0. It was attempted once to remove that function, but resulted in losing many cracks. One solution could be taking the pictures from a closer distance.

6.6 Discussion

Digital image processing can eliminate the need of direct human measurement and the objection in crack assessments. However, reaching this point requires algorithm improvements. On the other side, increasing the complexity of the algorithms, increases the computing time and costs.

Therefore, developing a method on low-cost devices that can perform the crack detection task is beneficial for maintenance agencies. This study has proposed a simple technique that has the potential of crack recognition and crack feature extraction. This algorithm showed that factorizing Otsu can result in more accurate crack detection and hence feature extraction. ROC ranking system helped to analyze the proposed method and choose the optimized fraction for the threshold value that Otsu produced.

- In the comparison performed between Sobel and Prewitt operators, cracks were brighter and more connected in the algorithm consisting Sobel edge detector.
- Results from this study indicate that the Otsu's threshold value calculated by MATLAB might not be necessarily the optimized value for object detection.
- Applying a parameter to factorize the calculated threshold has both the simplicity and optimizing effect on the algorithm.
- The visual assessment of the images after running the whole algorithm showed a factor over 30% of the threshold value could result in loss of cracks and lower accuracy.
- ROC curves for length calculation of four images demonstrate that the true positive ratio can vary from 69.5% to 95.9%.
- In crack's area analysis, a factor of 20% detects more surface area than the actual value. ROC curves for area

The obtained results show that using a factor of 20% to the Otsu's threshold value given by the algorithm, offers accurate results for length measurements. The average of TPR for the four images is equal to 84.125%, while the average of FPR is equaled to 0.125%. Although the length of the cracks plays the main role in condition surveying, it was attempted to measure the area and width of the cracks as well. As it was shown in result sections, the accuracy of the area detection is lower than length due to the fact that cavities may be connecting to the cracks or areas of blurs may be considering during the process. It is notable that the surface of the samples is also a critical aspect and the more even the surface is, the better the crack detection would be. Holes, blurs and color variations can impact the accuracy of the algorithm.

REFERENCES

- Abbasi, A. M., Zadeh, A. A. J., Ghodss, M., & Engineering, C. (1999). Application of Self Consolidating Concrete, pp 3–8.
- Abdel-Qader, I., Abudayyeh, O., Kelly, M. E. (2003). Analysis of Edge-Detection Techniques for Crack Identification in Bridges. Journal of Computing in Civil Engineering, 2003. Volume 17 Issue 4
- Akihama, S., Suenaga, T., & Banno, T. (1986). Mechanical properties of carbon fibre reinforced cement composites. International Journal of Cement Composites and Lightweight Concrete, 8(1), 21–33. https://doi.org/10.1016/0262-5075(86)90021-7
- Alhozaimy, A., Soroushian, P., Mirza, F. (1996). Mechanical properties of polypropylene fiber reinforced concrete and the effects of pozzolanic materials, Cement and Concrete Composites, vol: 18 (2) pp: 85-92.
- ASTM C150 / C150M-19a, Standard Specification for Portland Cement, ASTM International, West Conshohocken, PA, 2019, www.astm.org
- ASTM C39/C39M (2018). Standard Test Method for Compressive Strength of Cylindrical Concrete Specimens. ASTM International, 2018. West Conshohocken, PA.
- Bamonte, P., & Gambarova, P. G. (2012). A study on the mechanical properties of self-compacting concrete at high temperature and after cooling. Materials and Structures, 45(9), 1375–1387.
- Banyhussan, Q., Yıldırım, G., Bayraktar, E., Demirhan, S., Şahmaran, M. (2016). Deflection-hardening hybrid fiber reinforced concrete: The effect of aggregate content, Construction and Building Materials, Volume 125, 2016, Pages 41-52, ISSN 0950-0618, https://doi.org/10.1016/j.conbuildmat.2016.08.020.
- Bignozzi, M.C., Sandrolini, F. (2006). Tyre Rubber Waste Recycling in Self-Compacting Concrete. Cement and Concrete Research, 36, 735-739.
- Breitenbücher, R., Meschke, G., Song, F., & Zhan, Y. (2014). Experimental, analytical and numerical analysis of the pullout behaviour of steel fibres considering different fibre types, inclinations and concrete strengths. Structural Concrete, 15(2), 126–135. https://doi-org.mimas.calstatela.edu/10.1002/suco.201300058
- BS EN 12350-10, (2019). Testing fresh concrete. Self-compacting concrete. L box tests. British Standards Institution.
- BS EN 12350-9, (2010). Testing fresh concrete. Self-compacting concrete. V-funnel test. British Standards Institution.
- Canny, J. (1986). A Computational Approach to Edge Detection. IEEE Transactions on Pattern Analysis and Machine Intelligence, 1986. Volume 8, Issue 6.
- Chen, P.-W., & Chung, D. D. . (1993). Concrete reinforced with up to 0.2 vol% of short carbon fibres. Composites, 24(1), 33–52. https://doi.org/10.1016/0010-4361(93)90261-6
- Chung, D. D. . (2000). Cement reinforced with short carbon fibers: a multifunctional material. Composites Part B: Engineering, 31(6–7), 511–526. https://doi.org/10.1016/S1359-8368(99)00071-2
- Corinaldesi, V., & Moriconi, G. (2005). Durable fiber reinforced self-compacting concrete.
- Davidovits, J. (2015). Why Alkali-Activated Materials are NOT Geopolymers? Retrieved July 25, 2017

- DMI (2017). Diversified Minerals Inc Slag (GGBFS) Technical Data Sheet.
- Domone, P. L. (2006). A review of the hardened mechanical properties of self-compacting concrete.
- Domone, P. L. (2006). Self-compacting concrete: An analysis of 11 years of case studies. Cement and Concrete Composites, 28(2), 197–208.
- Duda, R., Hart, P. (1973). Pattern Classification and Scene Analysis, John Wiley and Sons,'73, pp271-2
- Eldin, N. N., & Senouci, A. B. (1993). Rubber-Tire Particles as Concrete Aggregate. Journal of Materials in Civil Engineering, 5(4), 478–496. https://doi.org/10.1061/(ASCE)0899-1561(1993)5:4(478)
- El-Newihy, A., Azarsa, P., Gupta, R., Biparva, A., (2018) Effect of Polypropylene Fibers on Self-Healing and Dynamic Modulus of Elasticity Recovery of Fiber Reinforced Concrete. Fibers 2018, 6, 9.
- Erkel, A., Pattynama, P. (1998). Receiver operating characteristic (ROC) analysis: basic principles and applications in radiology. European Journal of Radiology, 1998. Volume 27, Issue 2, pp 88–94
- Ferrara, L., Park, Y.-D., & Shah, S. P. (2007). A method for mix-design of fiber-reinforced self-compacting concrete. Cement and Concrete Research, 37(6), 957–971.
- Fibercast 500 Micro Fibers (2018). Fibercast 500 Product Data By Propex. Retrieved from www.fibermesh.com.
- Fisher, R., Perkins, S., Walker, A., Wolfart, E. Pixel Subtraction. Image Arithmetic. Available from: https://homepages.inf.ed.ac.uk/rbf/HIPR2/pixsub.htm. Cited: July 20, 2019
- Forno, C., Brown, S., Hunt, R. A., Kearney, A. M., Oldfield, S. (1991). The measurement of deformation of a bridge by Moirè photography and photogrammetry. Strain 27.3 (1991): 83-87.
- Fujita, Y., Hamamoto, Y. (2011). A robust automatic crack detection method from noisy concrete surfaces. Machine Vision and Applications, 2011. Volume 22, Issue 2, pp245-254
- Garcia Calvo, J.L., Alonso, M.C., Fernandez Luco, L., Robles Velasco, M. (2016). Durability Performance of Sustainable Self Compacting Concretes in Precast Products due to Heat Curing. Construction and Building Materials: 111, 379-385.
- Gastineau, A., Johanson, T., Schultz, A. (2009). Bridge Health Monitoring and Inspections – A Survey of Methods. Minnesota Department of Transportation, 2009. MN/RC 2009-29
- Gongkang, F., Moosa, A. G., (2002). An optical approach to structural displacement measurement and its application. Journal of Engineering Mechanics 128.5 (2002): 511-520.
- Graham, R. K., Huang, B., Shu, X., & Burdette, E. G. (2013). Laboratory evaluation of tensile strength and energy absorbing properties of cement mortar reinforced with micro- and meso-sized carbon fibers. Construction and Building Materials, 44, 751–756. https://doi.org/10.1016/J.CONBUILDMAT.2013.03.071
- Güneyisi, E. (2010). Fresh properties of self-compacting rubberized concrete incorporated with fly ash. Materials and Structures, 43(8), 1037–1048.
- Hameed, R., Turatsinze, A., Frederic, D., Sellier, A. (2009). Metallic Fiber Reinforced Concrete: Effect of Aspect Ratio of Flexural Properties. ARPN Journal of Applied Sciences: 4(5), 67-72.

- Hardjito, D., Wallah, S. E., Sumajouw, D. M., & Rangan, B. V. (2004). On the Development of Fly Ash-Based Geopolymer Concrete. ACI Materials Journal, 101(6), 467-472.
- Herbert, B., Ess, A., Tuytelaars, T., & Van Gool, L. (2008). Speeded-up robust features (SURF). Computer vision and image understanding, 110(3), 346-359.Pan et al. 2009
- Herbert, B., Tuytelaars, T., Van Gool, L. (2006). Surf: Speeded up robust features." European conference on computer vision. Springer, Berlin, Heidelberg, 2006.
- Hoang, N. (2018). Detection of Surface Crack in Building Structures Using Image Processing Technique with an Improved Otsu Method for Image Thresholding. Advances in Civil Engineering, 2018. Article ID 3924120
- Holschmacher, K., & Klug, Y. (2002). A Database for the Evaluation of Hardened Properties of SCC. Lacer, 123–134.
- Hossain, M. Z., & Awal, A. S. M. A. (2011). Flexural response of hybrid carbon fiber thin cement composites. Construction and Building Materials, 25(2), 670–677. https://doi.org/10.1016/J.CONBUILDMAT.2010.07.022
- Howarth, J., Mareddy, S. S. R., & Mativenga, P. T. (2014). Energy intensity and environmental analysis of mechanical recycling of carbon fibre composite. Journal of Cleaner Production, 81, 46–50. https://doi.org/10.1016/J.JCLEPRO.2014.06.023
- Hsie, M., Tu, C., Song, P. (2008). Mechanical properties of polypropylene hybrid fiber-reinforced concrete. Materials Science and Engineering: A 2008 vol: 494 (1-2) pp: 153-157
- Huang, B., Li, G., Pang, S. S., & Eggers, J. (2004). Investigation into waste tire rubber-filled concrete. Journal of Materials in Civil Engineering, 16(3), 187–194. https://doi.org/10.1061/(ASCE)0899-1561(2004)16:3(187)
- Hulin, L.R., Denis, P.E., Petit, F, Boutillon, L., Linger, L., Lefebvre, D. (2011). Tunnel Lining with Self Compacting Concrete (SCC) Segments Made with an Innovative Method of Casting Including an Adapted Mould, Proceedings of fib symposium, Prague.
- Jin, H., Lu, W. Y., & Korellis, J. (2008). Micro-scale deformation measurement using the digital image correlation technique and scanning electron microscope imaging. The Journal of Strain Analysis for Engineering Design, 43(8), 719-728.
- Karahan, O., Duran Atis, C. (2011). The durability properties of polypropylene fiber reinforced fly ash concrete. Materials and Design. 32, 2, 2.
- Khaloo, A., Raisi, E. M., Hosseini, P., & Tahsiri, H. (2014). Mechanical performance of self-compacting concrete reinforced with steel fibers. Construction and Building Materials, 51, 179–186.
- Khatib, Z. K., & Bayomy, F. M. (1999). Rubberized Portland cement concrete. Journal of Materials in Civil Engineering, 11(3), 206–213. https://doi.org/10.1061/(ASCE)0899-1561(1999)11:3(206)
- Khayat, K. H., & Taylor, P. (2007). SCC Formwork Pressure Task 1: Capturing Existing Knowledge on Formwork Pressure Exerted By SCC Phase I -Executive Summary.
- Kim, J. K., Moon, Y. H., Eo, S.H. Compressive Strength Development of Concrete with Different Curing Time and Temperature (1998). Cement and Concrete Research: 28(12), 1761-1773. https://doi.org/10.1016/S0008-8846(98)00164-1

- Lee, B., Y., Kim, Y., Y., Yi, S., Kim, J. (2013). Automated image processing technique for detecting and analyzing concrete surface cracks. Journal Structure and Infrastructure Engineering, 2013. Volume 9, Issue 6.
- Leendertz, J. A. (1970). Interferometric displacement measurement on scattering surfaces utilizing speckle effect, Journal of Physics E: Scientific Instruments, 3(3), 214.
- Leutenegger, S., Chli, M., Siegwart, R. Y. (2011) BRISK: Binary robust invariant scalable keypoints. Computer Vision (ICCV), 2011 IEEE International Conference on. IEEE, 2011.
- Li, L., Wang, Q., Zhang, G., Shi, L., Dong, J., Jia, P. (2018). A method of detecting the cracks of concrete undergo high-temperature, Construction and Building Materials, 2018, Volume 162, pp 345-358,
- Li, M., Yang, Y., Liu, M., Guo, X., & Zhou, S. (2015). Hybrid effect of calcium carbonate whisker and carbon fiber on the mechanical properties and microstructure of oil well cement. Construction and Building Materials, 93, 995–1002. https://doi.org/10.1016/J.CONBUILDMAT.2015.05.056
- Liu, Y., Farnsworth, M., & Tiwari, A. (2017). A review of optimisation techniques used in the composite recycling area: State-of-the-art and steps towards a research agenda. Journal of Cleaner Production, 140, 1775–1781. https://doi.org/10.1016/j.jclepro.2016.08.038
- Lou, Q., Ge, B., Tian, Q. (2019). A fast adaptive crack detection algorithm based on a double-edge extraction operator of FSM. Construction and Building Materials, 2019. Volume 204, pp 244-254
- Mathworks (2019). medfilt2, Help Center Documentation, Mathworks. Available from: https://www.mathworks.com/help/images/ref/medfilt2.html. Cited by July 20, 2019
- McCormick, N., Lord, J. (2010). Digital image correlation, Materials today 13.12 (2010): 52-54.
- Mohan, A., Poobal, S. (2018). Crack detection using image processing: A critical review and analysis. Alexandria Engineering Journal, 2018. Volume 57, Issue 2, pp 787-798
- Morcous, G., Wang, K., Taylor, P.C., Shah, S.P. (2016). Self-Consolidating Concrete for Cast-in-Place Bridge Components. NCHRP Report 819.
- Moutassem, Fayez (2016). Assessment of Packing Density Models and Optimizing Concrete Mixtures. International Journal of Civil, Mechanical and Energy Science (UCMES), 2(4): 29-36.
- Nitschke, A. G., Gall, V., Pyakurel, S., Mazzoni, D., & Becker, J. (2005). Self-Bearing Shotcrete in Lieu of Self-Consolidating Concrete for Tunnel Rehabilitation, (3), 365–373.
- Okamura, H., & Ouchi, M. (2003). Self-Compacting Concrete. Journal of Advanced Concrete Technology, 1(1), 5–15.
- Oliveux, G., Dandy, L. O., & Leeke, G. A. (2015). Current status of recycling of fibre reinforced polymers: Review of technologies, reuse and resulting properties. Progress in Materials Science, 72, 61–99. https://doi.org/10.1016/J.PMATSCI.2015.01.004
- Otsu, N. (1979) A Threshold Selection Method from Gray-Level Histograms. IEEE Transactions on Systems, Man, and Cybernetics, 1979. Volume 9, Issue 1, pp 62-66
- Ouchi, M., Aki, S., Osterberg, T., Hallberg, S.-E., & Lwin, M. (2003). Applications of Self-Compacting Concrete in Japan, Europe and the United States. Federal Highway Administration, 1–20.

- Park, S. B., Lee, B. I., & Lim, Y. S. (1991). Experimental study on the engineering properties of carbon fiber reinforced cement composites. Cement and Concrete Research, 21(4), 589–600. https://doi.org/10.1016/0008-8846(91)90110-4
- Persson, Bertil. (2001). A Comparison Between Mechanical Properties of Self-Compacting Concrete and the Corresponding Properties of Normal Concrete. Cement and Concrete Research: 193-198.
- Pintado, X., & Barragán, B. E. (2009). Homogeneity of self-compacting concretes used in tunnel strengthening – A case study. Tunnelling and Underground Space Technology, 24(6), 647–653.
- Ramujee, K., & PothaRaju, M. (2017). Mechanical Properties of Geopolymer Concrete Composites. Materials Today: Proceedings, 4(2), 2937–2945.
- Rangan, B. V. (2008). Low-Calcium, Fly-Ash-Based Geopolymer Concrete. Concrete Construction Engineering Handbook, 1-44.
- Rangelov, M., Nassiri, S., Haselbach, L., & Englund, K. (2016). Using carbon fiber composites for reinforcing pervious concrete. Construction and Building Materials, 126, 875–885. https://doi.org/10.1016/j.conbuildmat.2016.06.035
- Repository, I. (2003). Development of self-compacting concrete.
- Richard-, L. (2011). Tunnel Lining with Self-Compacting Concrete (SCC) Segments Made With an Innovative Method, (January 2011), 667–670.
- Saccani, A., Manzi, S., Lancellotti, I., & Lipparini, L. (2019). Composites obtained by recycling carbon fibre/epoxy composite wastes in building materials. Construction and Building Materials, 204, 296–302. https://doi.org/10.1016/J.CONBUILDMAT.2019.01.216
- Sadana, H.A., Marquez Aguilar, P.A., Molina, O.A. (2015). Concrete Stress-Strain Characterization by Digital Image Correlation, J Appl Mech Eng 4: 189
- Shu, X., Graham, R. K., Huang, B., & Burdette, E. G. (2015). Hybrid effects of carbon fibers on mechanical properties of Portland cement mortar. Materials & Design (1980-2015), 65, 1222–1228. https://doi.org/10.1016/J.MATDES.2014.10.015
- Singh, B., Ishwarya, G., Gupta, M., & Bhattacharyya, S. K. (2015). Geopolymer concrete: A review of some recent developments. Construction and Building Materials, 85, 78–90.
- Song, P., Hwang, S., Sheu, B. (2005). Strength properties of nylon- and polypropylene-fiber-reinforced concretes. Cement and Concrete Research. Vol: 35 (8) pp: 1546-1550
- Song, W., & Yin, J. (2016). Hybrid effect evaluation of steel fiber and carbon fiber on the performance of the fiber reinforced concrete. Materials, 9(8), 704.
- Structural Health Monitoring Solutions. SC Solutions. Available from: https://www.scsolutions.com/structural/products-and-solutions/structural-health-monitoring-solutions/. Cited July 20, 2019
- Toutanji, H. A., El-Korchi, T., & Katz, R. N. (1994). Strength and reliability of carbon-fiber-reinforced cement composites. Cement and Concrete Composites, 16(1), 15–21. https://doi.org/10.1016/0958-9465(94)90026-4
- USTMA. (2017). U.S. Scrap Tire Management Summary. U.S. Tire Manufacturers Association. Accessed on Nov 2019, from https://www.ustires.org/system/files/USTMA_scraptire_summ_2017_072018.pdf

- Weimin, S., Jian, Y. (2016). Hybrid Effect Evaluation of Steel Fiber and Carbon Fiber on the Performance of the Fiber Reinforced Concrete. Materials (1996-1944), 9(8), 1–12. https://doi-org.mimas.calstatela.edu/10.3390/ma9080704
- Wood, K. (2019). Carbon fiber reclamation: Going commercial: Composites World. Retrieved August 27, 2019, from https://www.compositesworld.com/articles/carbon-fiber-reclamation-going-commercial
- Xu, L., Li, B., Chi, Y., Li, C., Huang, B., & Shi, Y. (2018). Stress-Strain Relation of Steel-Polypropylene-Blended Fiber-Reinforced Concrete under Uniaxial Cyclic Compression. Advances in Materials Science & Engineering, 1–19. https://doi-org.mimas.calstatela.edu/10.1155/2018/9174943
- Zhang, K. (2014). Digital Image Correlation Analysis of Alkali Silica Reaction in Concrete with Recycled Glass Aggregate, Master Thesis, University of Illinois at Urbana-Champaign.
- Zhu, W., Bartos, P. (2003). Permeation Properties of Self-Compacting Concrete. Cement and Concrete Research: 33, 921-926.
-

APPENDIX A – TECHNOLOGY TRANSFER ACTIVITIES

1 Accomplishments

The results of this project were disseminated through a webinar, hosted jointly by UTC-UTI and TranSET UTC, and in collaboration with Texas A&M and Virginia DOT, in July 2018 (see Figure A.1). The other outcomes also published and presented at Transportation Research Board (TRB) annual meeting through Eisenhower Transportation Fellowship as well as ASCE conferences. Please see section 3 for the list of publications from this project.

Figure A.1. Technology Transfer Webinar hosted by UTC-UTI and TranSET UTC

2 Participants and Collaborating Organizations

We would like to acknowledge the support from the following partners in this project:

- Euclid chemical
- Crumb Rubber Mfg. (CRM)
- Diversified Minerals Inc.
- BASF

3 Outputs

Presentations/Publications

- UTC-UTI symposium in Colorado School of Mines
- ASCE International Conference on Transportation and Development in Pittsburg, Pennsylvania
- Annual Research Symposium at Cal State LA
- University of Southern California Research Seminar,
- Hispanic Engineer National Achievement Awards Corporation (HENAAC) Conference

4 Outcomes

The outcomes of this project published in the form of this final project and other publications/presentation in technical conferences.

Publications

- Marquez, D., Ojeda, F., Cruz, H., NG, J., Mazari, M. (2019) "Evaluating Fresh and Hardened Properties of Fiber Reinforced Self-Consolidating Concrete for Transportation Infrastructure Applications," Transportation Research Board Annual Meeting, Washington, D.C.
- Lim, J. S., Cruz, H., Pourhomayoun, M., & Mazari, M. (2018). Application of IoT for Concrete Structural Health Monitoring. In 2018 International Conference on Computational Science and Computational Intelligence (CSCI) (pp. 1479-1482). IEEE.

Presentations

- UTC-UTI symposium at Colorado School of Mines
- ASCE International Conference on Transportation and Development in Pittsburg, Pennsylvania
- Annual Research Symposium at Cal State LA
- Annual Urban Sustainability Symposium hosted by Sikand SITI Center at Cal State LA
- Leval Lund Symposium at the University of Southern California

5 Impacts

This project helped support graduate and undergraduate students at Cal State LA as well as providing the opportunity for outreach activities for K-12 students. The project also helped Cal State LA to collaborate with industry and local agency partners.

APPENDIX B - DATA FROM THE PROJECT

Relative density of sand

				TYPE	Fines aggregates = all sizes			
Relative density for fine aggregates								
Sand n°	S	A	B	C	Relative density (OD)	Relative density (SSD)	Apparent relative density	Absorption relative density
1	500	482	645,1	797,1	1,39	1,44	1,46	3,73
2	400	364,3	645,1	871,1	2,09	2,30	2,63	9,80
3	500	485,1	645,1	787,5	1,36	1,40	1,42	3,07
					Gsb	GSSD	Gsa	%
					1,73	1,85	2,02	6,44

				TYPE	Fines aggregates = all sizes			
Relative density for fine aggregates								
Sand n°	S	A	B	C	Relative density (OD)	Relative density (SSD)	Apparent relative density	Absorption relative density
1	400	392,5	646,7	896,9	2,62	2,67	2,76	1,91
2	400	395,3	646,7	896,7	2,64	2,67	2,72	1,19
					Gsb	GSSD	Gsa	%
					2,63	2,67	2,74	1,55

				TYPE	Fines aggregates <=1.16 mm			
Relative density for fine aggregates								
Sand No.	S	A	B	C	Relative density (OD)	Relative density (SSD)	Apparent relative density	Absorption relative density
1	400	384,3	647,3	890	2,44	2,54	2,71	4,09
2	400	386,8	647,2	890,3	2,47	2,55	2,69	3,41
					Gsb	GSSD	Gsa	%
					2,45	2,55	2,70	3,75

Relative density of coarse aggregates

Relative density for fine aggregates								
Sand n°	S	A	B	C	Relative density	Relative density (SSD)	Apparent relative density	Absorption relative density
A	1500	1427,4	1462,1	942	2,74	2,81	2,94	2,43
B	2000	1883	1942,6	1174,1	2,45	2,53	2,66	3,17
C	1500	1417,9	1455,7	894,2	2,53	2,59	2,71	2,67
					Gsb	GSSD	Gsa	%
					2,57	2,64	2,77	2,92

Properties of different fiber types

Type of fiber	Length (mm)	Aspect ratio	Shape	Tensile strength (MPa)
Steel	30	65	Hooked end	1100
Carbon	5	150	straight	3 500
Polypropylene	12	140	straight	300
Macro synthetic	56	74	flexible	600
Recycled waste tire (Type I)	34	60-135	irregular	NA
Recycled waste tire (Type II)	10	30	irregular	NA
Homopolymer polypropylene	6	NA	straight	660

Compressive strength test data

Sample Area (m^2)=	0.00810732	Peak Load (N)						Compressive Strength (MPa)									
Day		7			28			7			28			Average		STD	
Mix #	Mix ID	S1	S2	S3	S1	S2	S3	S1	S2	S3	S1	S2	S3	7	28	7	28
001	Control	30000	10000	10000	10000	10000	10000	3.7	1.2	1.2	1.2	1.2	1.2	2.1	1.2	1.4	0.0
002	Control	115609	156310	105244	153508	178507	143766	14.4	19.3	13.1	19.0	22.0	17.5	15.6	19.5	3.3	2.3
003	recycled tire I	195988	156755	126729	208132	164673	159290	24.5	19.4	15.4	25.4	19.7	19.4	19.7	21.5	4.6	3.4
006	Control	120000	125000	131178	185891	134736	151951	14.4	15.4	16.2	22.8	16.7	18.8	15.3	19.5	0.9	3.1
007	recycled tire I	132379	140252	157956	214092	213986	150438	16.4	17.4	19.6	26.4	26.4	18.6	17.8	23.8	1.7	4.5
008	recycled tire II	109070	104132	105912	193052	270407	345404	13.3	12.7	13.0	23.7	33.4	42.7	13.0	33.3	0.3	9.5
011	Fibers	191273	143455	90387	120000	132900	180108	23.7	17.7	11.1	14.6	16.2	22.2	17.5	17.7	6.3	4.0
014	CTRL	128464	112762	108670	358927	378499	366577	15.2	13.8	13.3	44.0	46.5	45.0	14.1	45.2	1.0	1.2
015	RTS	134425	105200	145012	317113	340466	353678	16.6	13.0	17.9	38.6	41.8	43.6	15.8	41.3	2.5	2.5
016	RTT	131355	108269	130243	355235	370047	357948	16.2	13.3	16.1	42.8	45.5	44.1	15.2	44.1	1.7	1.4
017	RCF	156177	161826	162315	311909	319382	301500	19.3	20.0	20.2	38.4	39.4	36.7	19.8	38.2	0.5	1.4
018	HPF	124639	136560	118055	312976	314177		15.5	16.9	14.7	38.4	38.7		15.7	38.5	1.1	0.2
019	MSF	124105	176460	155954	344114	363686	366711	15.3	21.9	19.2	40.8	44.4	43.9	18.8	43.0	3.3	2.0
020	MFP	127886	153016	126462	348073	314578	311953	15.9	19.0	15.6	42.0	38.3	37.7	16.8	39.4	1.9	2.3
021	SHF	135457	142930	149935	361640	358304	332238	16.6	17.4	18.1	44.6	44.2	41.0	17.4	43.3	0.7	2.0
014-6	CTRL				336694	128509	143944	0.0	0.0	0.0	16.9	15.9	17.8	0.0	16.8	0.0	1.0
022	RCF+RTT				303591	318181		0.0	0.0	0.0	37.4	39.2		0.0	38.3	0.0	1.3
022-2	RCF+RTT	153342	150894	140738	296652	336197		18.9	18.6	17.4	36.6	41.5		18.3	39.0	0.8	3.4
023-1	RCF+RTS	141989	148003	144375	394780	314178	375652	17.5	18.3	17.8	48.7	38.8	46.3	17.9	44.6	0.4	5.2
023-2	RCF+RTS	239759	235355	262979	348518	344826	351943	29.6	29.0	32.4	43.0	42.5	43.4	30.3	43.0	1.8	0.4

Split Tensile Test Results

Sample Area (m^2)=	0.00810732	Peak Load (N)			Split Tensile Strength (Mpa)				
Day		28			28			Avg	STD
Analysis with removal of outliers									
014	CTRL	99596	97594		3.1	3.0		3.0	0.0
015	RTS	66501	86607		2.1	2.7		2.4	0.4
016	RTT	67168	59695	81225	2.1	1.8	2.5	2.1	0.3
017	RCF	110271	103243	98973	3.4	3.2	3.1	3.2	0.2
018	HPF	89365	83716		2.8	2.6		2.7	0.1
019	MSF	90610		108047	2.8		3.3	3.1	0.4
020	MFP	74864	75442	71394	2.3	2.3	2.2	2.3	0.1
021	SHF	90000	103243	88000	2.8	3.2	2.7	2.9	0.3
022	RCF+RTT	100542	88397	91589	3.1	2.7	2.8	2.9	0.2
023	RCF+RTS	112718	105779	92212	3.5	3.3	2.8	3.2	0.3

Absorption Test Results

Sample	No.	A - Oven Dry Mass (g)	B - SSD after 48 hr (g)	C - SSD after boiling (g)	C-B	D - Immerse Apparent Mass (g)	Absorption after 48 hrs (%)	Asorption After Boiling (%)	Bulk Density (dry)	Bulk Density (immersion)	Bulk Density (boil)	Apparent Density	Voids (%)	Voids avg
14	1	1300.0	1362.3	1364.3	2.0	781.0	4.8	4.9	2228.70	2335.50	2338.93	2504.82	11.0	
14	2	1520.0	1593.3	1596.1	2.8	918.0	4.8	5.0	2241.56	2349.65	2353.78	2524.92	11.2	11.5
14	3	1280.0	1348.1	1350.0	1.9	776.0	5.3	5.5	2229.97	2348.61	2351.92	2539.68	12.2	
15	1	1317.1	1380.7	1381.0	0.3	770.0	4.8	4.9	2155.65	2259.74	2260.23	2407.42	10.5	
15	2	1388.1	1374.7	1462.0	87.3	815.4	-1.0	5.3	2146.77	2126.04	2261.06	2423.78	11.4	11.1
15	3	1292.6	1360.4	1360.7	0.3	760.0	5.2	5.3	2151.82	2264.69	2265.19	2426.96	11.3	
16	1	1266.9	1332.7	1331.7	-1.0	756.4	5.2	5.1	2202.16	2316.53	2314.79	2481.68	11.3	
16	2	1301.7	1462.3	1372.9	-89.4	776.6	12.3	5.5	2182.96	2452.29	2302.36	2478.96	11.9	11.4
16	3	1383.0	1452.2	1451.2	-1.0	825.0	5.0	4.9	2208.56	2319.07	2317.47	2478.49	10.9	
17	1	1261.4	1341.1	1340.0	-1.1	730.0	6.3	6.2	2067.87	2198.52	2196.72	2373.73	12.9	
17	2	1269.0	1351.8	1350.9	-0.9	740.0	6.5	6.5	2077.26	2212.80	2211.33	2398.87	13.4	13.4
17	3	1168.0	1246.0	1246.0	0.0	683.0	6.7	6.7	2074.60	2213.14	2213.14	2408.25	13.9	
18	1	1345.5	1427.6	1430.8	3.2	792.1	6.1	6.3	2106.62	2235.17	2240.18	2431.33	13.4	
18	2	1189.4	1264.2	1265.1	0.9	700.0	6.3	6.4	2104.76	2237.13	2238.72	2430.32	13.4	13.4
18	3	1247.2			0.0									
19	1	1251.9	1344.2	1349.6	5.4	752.9	7.4	7.8	2098.04	2252.72	2261.77	2508.82	16.4	
19	2	1286.7	1376.5	1380.3	3.8	774.8	7.0	7.3	2125.02	2273.33	2279.60	2513.58	15.5	15.8
19	3	1354.0	1447.1	1453.2	6.1	810.5	6.9	7.3	2106.74	2251.59	2261.09	2491.26	15.4	
20	1	1300.4	1389.5	1395.4	5.9	771.8	6.9	7.3	2085.31	2228.19	2237.65	2460.08	15.2	
20	2	1190.0	1275.1	1281.6	6.5	710.6	7.2	7.7	2084.06	2233.10	2244.48	2482.27	16.0	15.6
20	3	1460.0	1559.7	1568.1	8.4	867.8	6.8	7.4	2084.82	2227.19	2239.18	2465.38	15.4	
21	1	1300.4	1381.5	1388.3	6.8	775.3	6.2	6.8	2121.37	2253.67	2264.76	2476.48	14.3	
21	2	1318.7	1400.3	1408.5	8.2	785.7	6.2	6.8	2117.37	2248.39	2261.56	2474.11	14.4	14.2
21	3	1179.5	1250.7	1255.7	5.0	703.2	6.0	6.5	2134.84	2263.71	2272.76	2476.38	13.8	
22	1	877.8	938.6	940.7	2.1	696.5	6.9	7.2	3594.59	3843.57	3852.17	4841.70	25.8	
22	2	1237.2	1311.5	1314.6	3.1	705.0	6.0	6.3	2029.53	2151.41	2156.50	2324.69	12.7	17.3
22	3	1116.0	1188.2	1190.7	2.5	637.8	6.5	6.7	2018.45	2149.03	2153.55	2333.75	13.5	
23	1	1080.4	1138.4	1142.7	4.3	528.1	5.4	5.8	1757.89	1852.26	1859.26	1956.18	10.1	
23	2	1253.0	1321.1	1326.4	5.3	609.9	5.4	5.9	1748.78	1843.82	1851.22	1948.38	10.2	13.3
23	3	939.9	990.2	995.4	5.2	712.3	5.4	5.9	3320.03	3497.70	3516.07	4129.61	19.6	
22-2	1	1143.7	1216.6	1219.3	2.7	648.4	6.4	6.6	2003.33	2131.02	2135.75	2309.11	13.2	
22-2	2	1037.6	1106.9	1110.2	3.3	590.7	6.7	7.0	1997.31	2130.70	2137.05	2321.77	14.0	13.7
22-2	3	1210.8	1260.6	1294.7	34.1	689.8	4.1	6.9	2001.65	2083.98	2140.35	2323.99	13.9	
23-2	1	1399.2	1497.0	1497.3	0.3	803.0	7.0	7.0	2015.27	2156.13	2156.56	2346.86	14.1	
23-2	2	1154.5	1232.4	1232.6	0.2	658.7	6.7	6.8	2011.67	2147.41	2147.76	2328.56	13.6	13.9
23-2	3	1163.7	1244.0	1244.9	0.9	665.2	6.9	7.0	2007.42	2145.94	2147.49	2334.40	14.0	

Resistivity test results

	CTRL			RTS			RTT			CF			CF+RTT		
	14-1	14-2	14-3	15-1	15-2	15-3	16-1	16-2	16-3	17-1	17-2	17-3	22-1	22-2	22-3
D1 (mm)	101.44	101.74	102	101.59	101.79	102.08	101.54	101.51	102.36	101.74	102.15	101.77	100.98	102.16	101.59
D2 (mm)	102.12	101.47	101.03	101.81	101.44	101.41									
D avg	101.78	101.605	101.515	101.7	101.615	101.745	101.54	101.51	102.36	101.74	102.15	101.77	100.98	102.16	101.59
A (m^2)	0.008136	0.008108	0.008094	0.008123	0.00811	0.00813	0.008098	0.008093	0.008229	0.00813	0.008195	0.008134	0.008009	0.008197	0.008106
H1 (mm)	201.68	203.77	202.26	201.43	203.17	201.95	204.77	204.17	206.29	207.9	206.13	207.99	204.83	205.77	204.43
H2 (mm)	203.27	204.98	201.88	201.96	203.14	202.07									
Havg	202.475	204.375	202.07	201.695	203.155	202.01	204.77	204.17	206.29	207.9	206.13	207.99	204.83	205.77	204.43
Z (kOhm)	2.2	2.23	2.19	1.37	1.44	1.25	2.68	2.5	2.6	155	115	101	104	126	98.8
ϕ	1	1	1	2	2	2	1	1	1	14	14	16	13	14	14
ρ	88	88	88	55	57	50	106	99	104	6,061	4,572	3,950	4,066	5,019	3,917
		CTRL			RTS			RTT			CF			CF+RTT	
ρ_{avg} (Ω.m)		88			54			103			4,861			4,334	

SCC fresh test results

No.002			
Fresh results			Acceptable values
J-Ring	T_{500} (sec)=	9,29	3-6 (sec)
	d1 (cm)=	62	-
	d2 (cm)=	63	-
	d average=	62.5	60-75 (cm)
	h1 (cm)=	2,8	-
	h2 (cm)=	2	-
	h difference=	0,8	0-1 (cm)
Slump	T_{500} (sec)=	10.06	2-5 (sec)
	d1 (cm)=	62.5	-
	d2 (cm)=	67	-
	d average=	64.75	65-80 (cm)
	Penetration (mm)=	14	0-25 (mm)
	Segregation resistance=	Moderately	-
Blocking assessment	ds - dj (cm) =	2.25	≤ 5 (cm)
	Blocking=	no visible	-
L-Box	T500 (sec)=	3.54	3-6 (sec)
	H1 (cm)=	8	-
	H2 (cm)=	7.2	-
	H2/H1=	0.9	0,8-1
V-Funnel	T (sec)=	11.69	6-12 (sec)

Red values : over or under the acceptable values
Orange values : close to the acceptable values but not acceptable
Green values : acceptable values

No.003			
Fresh results			Acceptable values
J-Ring	T_{500} (sec)=	0	3-6 (sec)
	d1 (cm)=	44	-
	d2 (cm)=	43.5	-
	d average=	43.75	60-75 (cm)
	h1 (cm)=	5.3	-
	h2 (cm)=	2.9	-
	h difference=	2.4	0-1 (cm)
Slump	T_{500} (sec)=	0	2-5 (sec)
	d1 (cm)=	52	-
	d2 (cm)=	52	-
	d average=	52	65-80 (cm)
	Penetration (mm)=	0	0-25 (mm)
	Segregation resistance=	resistant	-
Blocking assessment	ds - dj (cm) =	8.25	≤ 5 (cm)
	Blocking=	extreme blocking	-

Red values : over or under the acceptable values
Orange values : close to the acceptable values but not acceptable
Green values : acceptable values

No.013			
Fresh results			Acceptable values
J-Ring	T_{500} (sec)=	7.39	3-6 (sec)
	d1 (cm)=	64.5	-
	d2 (cm)=	65	-
	d average=	64.75	60-75 (cm)
	h1 (cm)=	10.5	-
	h2 (cm)=	10	-
	h difference=	0.5	0-1 (cm)
Slump	T_{500} (sec)=	5.03	2-5 (sec)
	d1 (cm)=	69.9	-
	d2 (cm)=	69	-
	d average=	69.45	65-80 (cm)
	Penetration (mm)=	-	0-25 (mm)
	Segregation resistance=	-	-
Blocking assessment	ds - dj (cm) =	4.7	≤ 5 (cm)
	Blocking=	minimal blocking	-

Red values : over or under the acceptable values
Orange values : close to the acceptable values but not acceptable
Green values : acceptable values

No.014			
Fresh results			Acceptable values
J-Ring	T_{500} (sec)=	10.04	3-6 (sec)
	d1 (cm)=	60.5	-
	d2 (cm)=	61	-
	d average=	60.75	60-75 (cm)
	h1 (cm)=	10.5	-
	h2 (cm)=	10	-
	h difference=	0.5	0-1 (cm)
Slump	T_{500} (sec)=	8.87	2-5 (sec)
	d1 (cm)=	65	-
	d2 (cm)=	65	-
	d average=	65	65-80 (cm)
	Penetration (mm)=	15	0-25 (mm)
	Segregation resistance=	Moderately resistant	-
Blocking assessment	ds - dj (cm) =	4.25	≤ 5 (cm)
	Blocking=	Minimal blocking	-
L-Box	T500 (sec)=	3.68	3-6 (sec)
	H1 (cm)=	7.5	-
	H2 (cm)=	7.6	-
	H2/H1=	1.01	0.8-1
V-Funnel	T (sec)=	9.3	6-12 (sec)

No.016			
Fresh results			Acceptable values
J-Ring	T_{500} (sec)=	8	3-6 (sec)
	d1 (cm)=	61	-
	d2 (cm)=	66	-
	d average=	63.5	60-75 (cm)
	h1 (cm)=	10.2	-
	h2 (cm)=	9.5	-
	h difference=	0.7	0-1 (cm)
Slump	T_{500} (sec)=	7.36	2-5 (sec)
	d1 (cm)=	65.5	-
	d2 (cm)=	67.5	-
	d average=	66.5	65-80 (cm)
	Penetration (mm)=	13	0-25 (mm)
	Segregation resistance=	Moderately resistant	-
Blocking assessment	ds - dj (cm) =	3	≤ 5 (cm)
	Blocking=	Minimal blocking	-
L-Box	T500 (sec)=	2.13	3-6 (sec)
	H1 (cm)=	8.1	-
	H2 (cm)=	7.1	-
	H2/H1=	0.88	0.8-1
V-Funnel	T (sec)=	6.3	6-12 (sec)

Carbon fibers

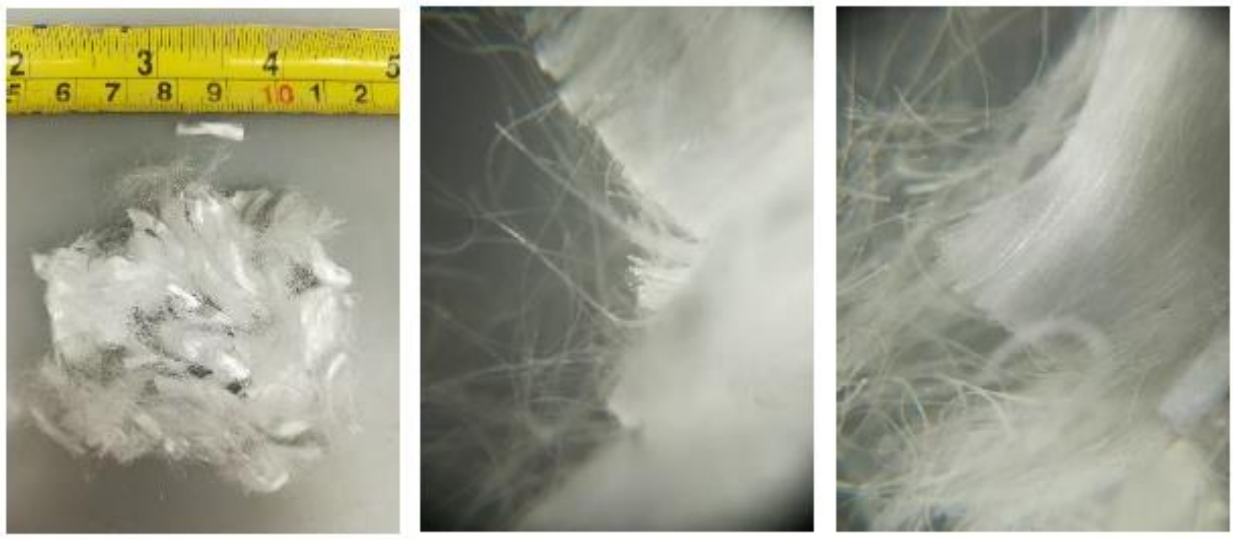

Polypropylene fibers

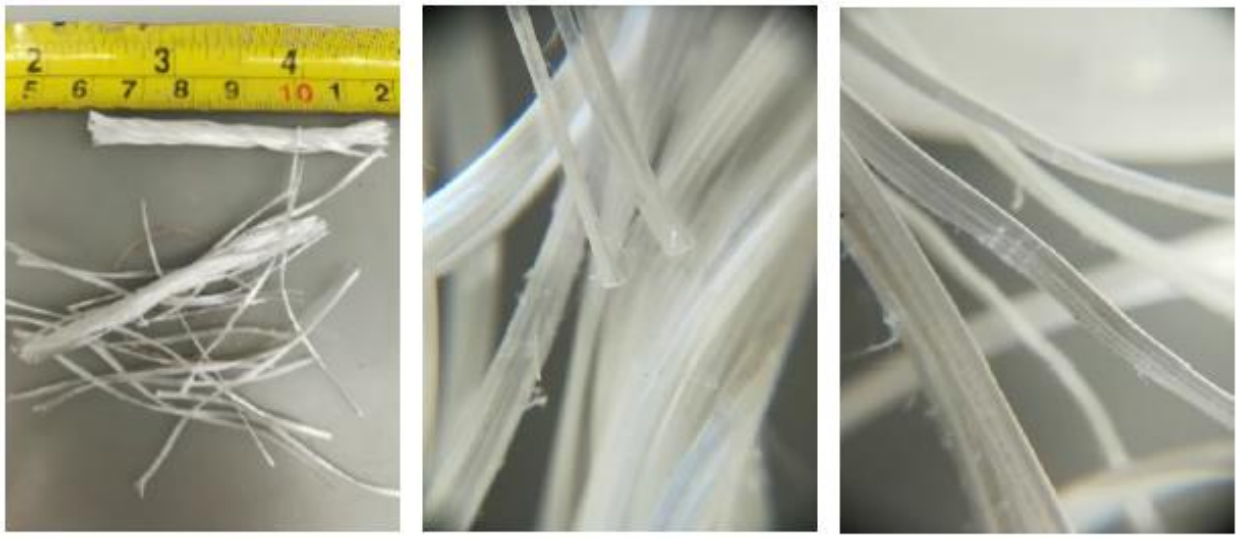

Macro synthetic fibers

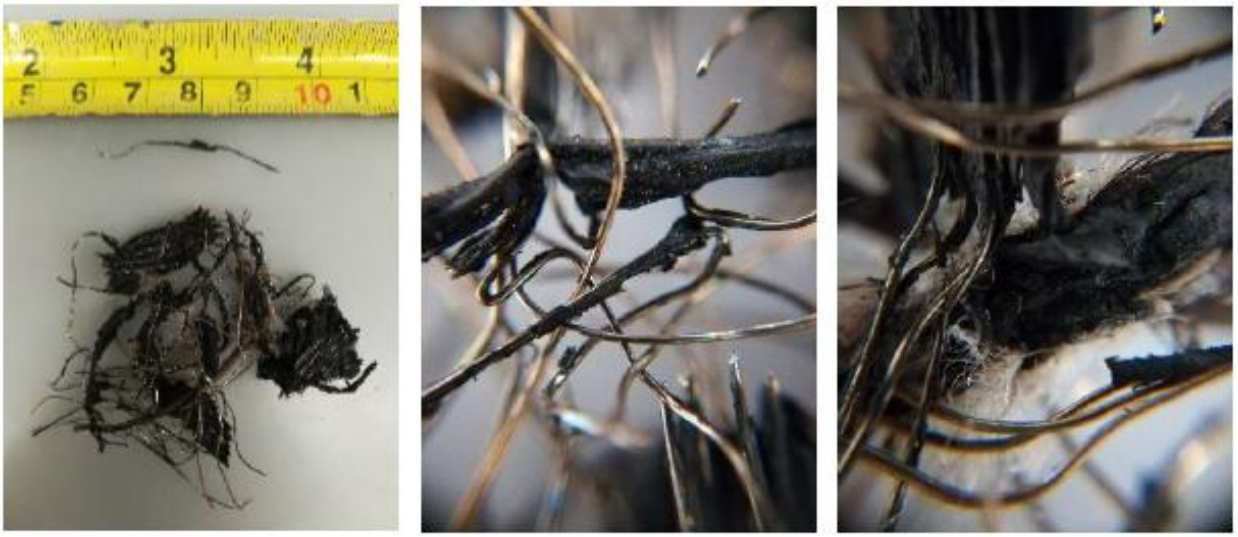

Recycled waste tire fibers type I

Recycled waste tire fibers type II

Homopolymer polypropylene fibers

Steel Fibers

Data from the visual detection of surface defects for cylindrical concrete samples

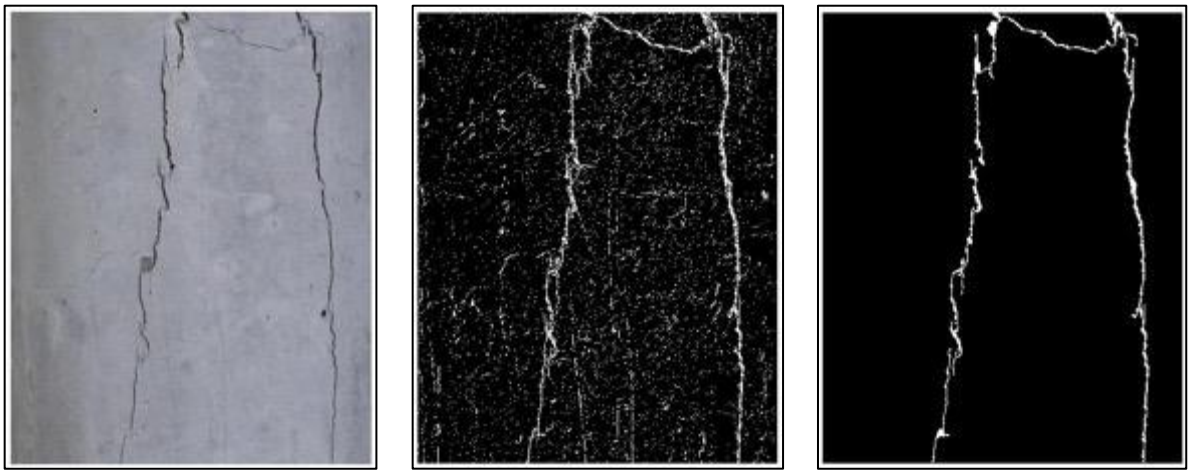

Figure 1 - Sample #1

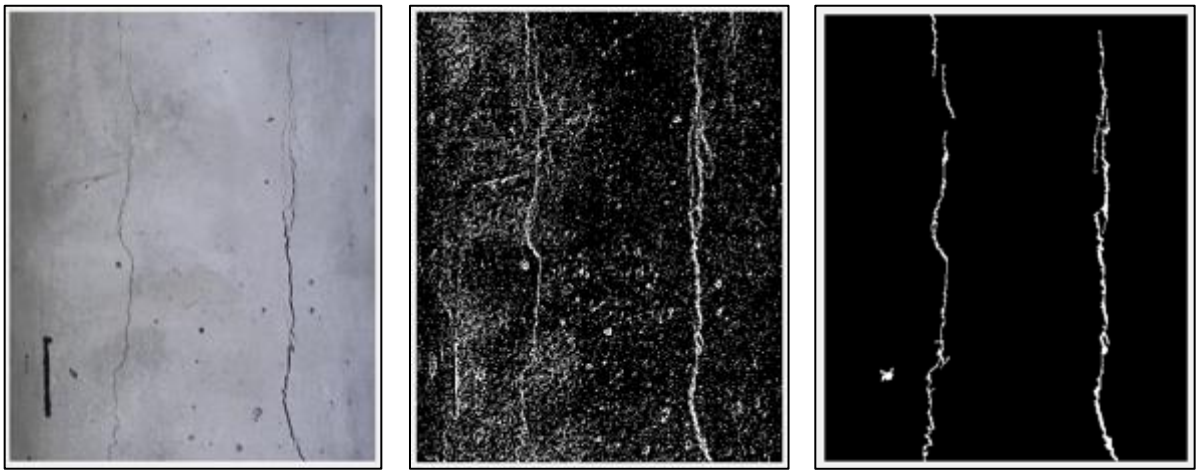

Figure 2 - Sample #2

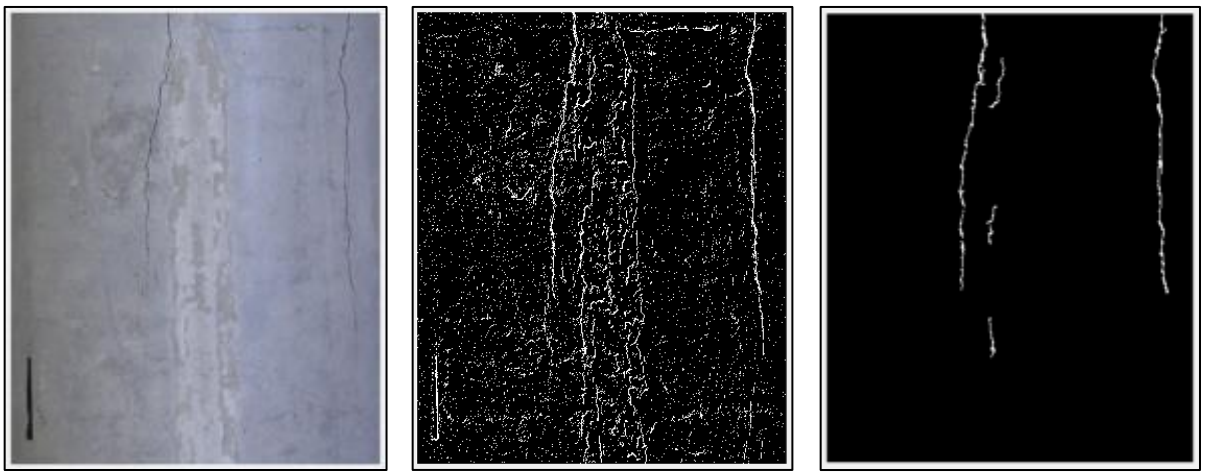

Figure 3 - Sample #3

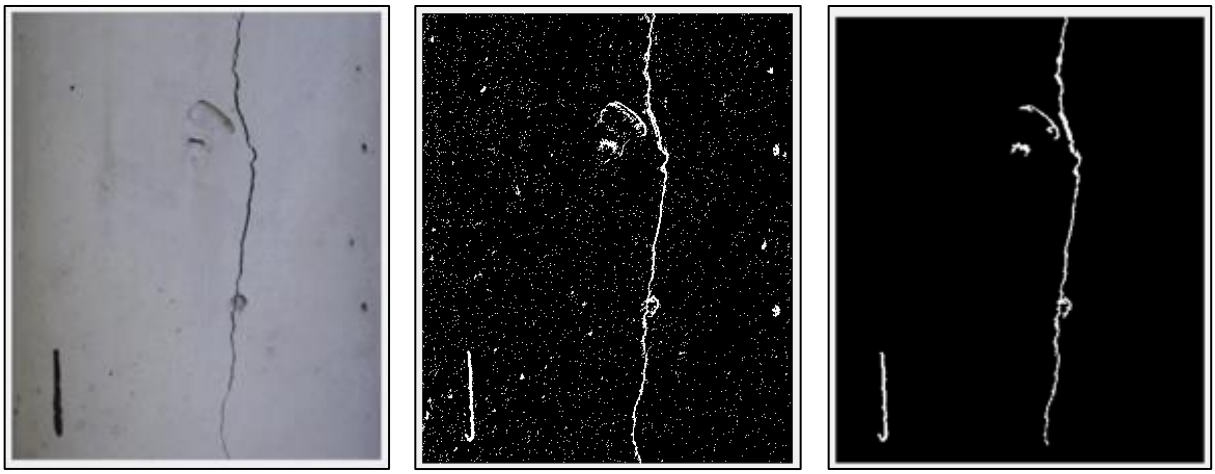

Figure 4 - Sample #4

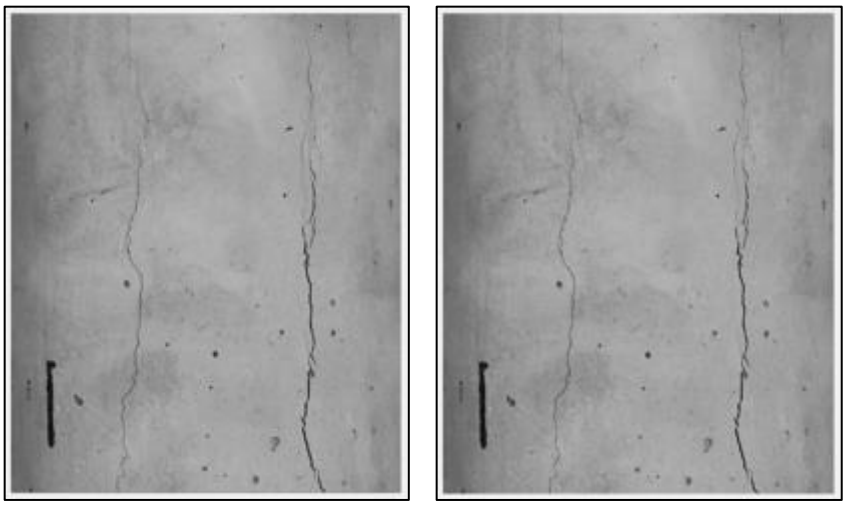

(a) (b)

Figure 5 - Application of medfilt2 function

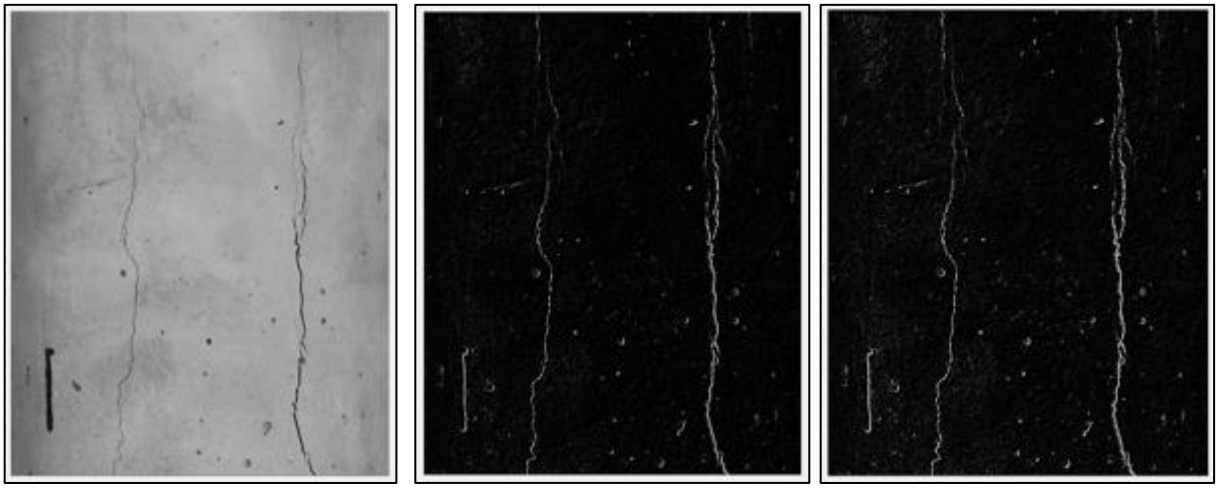

(a) (b) (c)

Figure 6 - Processed images after using Prewitt and Sobel operators

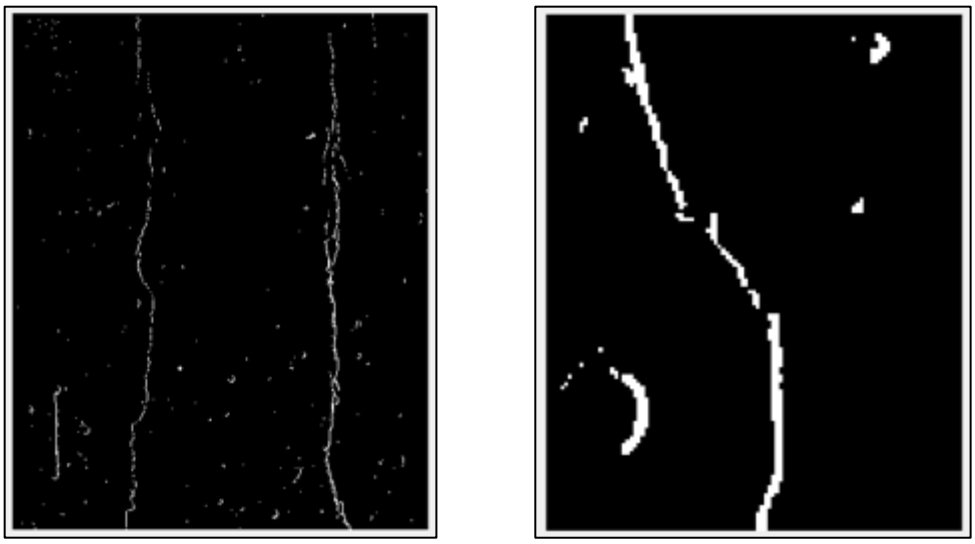

(a) (b)

Figure 7 - Unconnected cracks

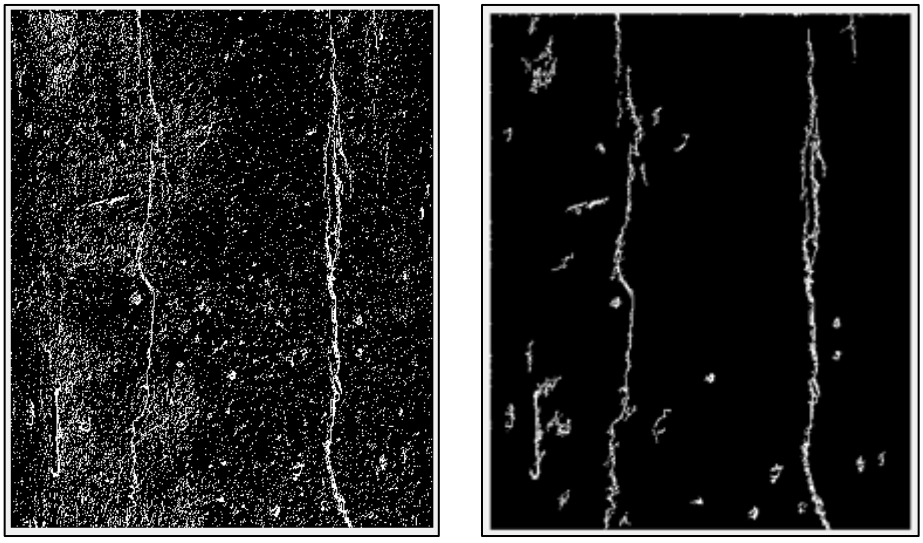

Figure 8 - Area cut-off

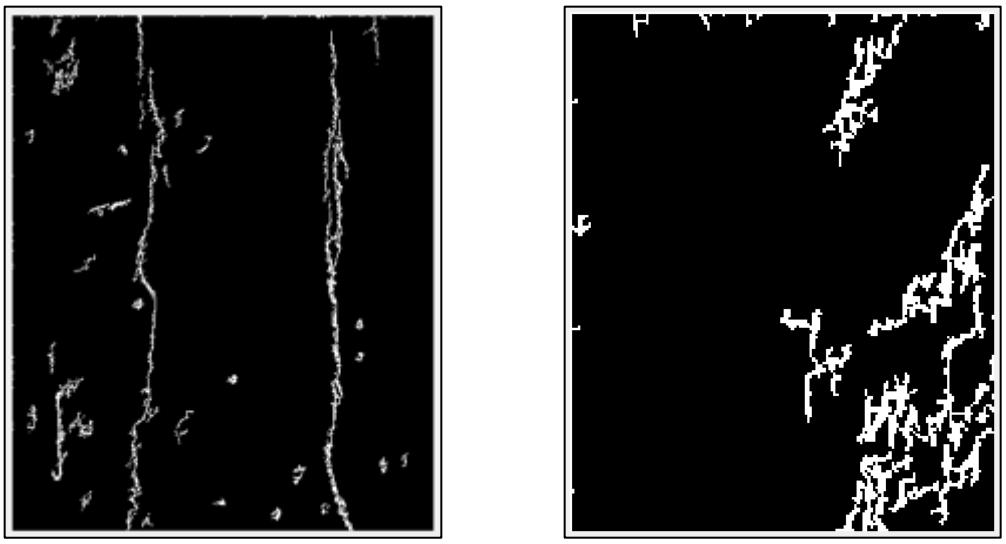

Figure 9 - Contour of the image with noise

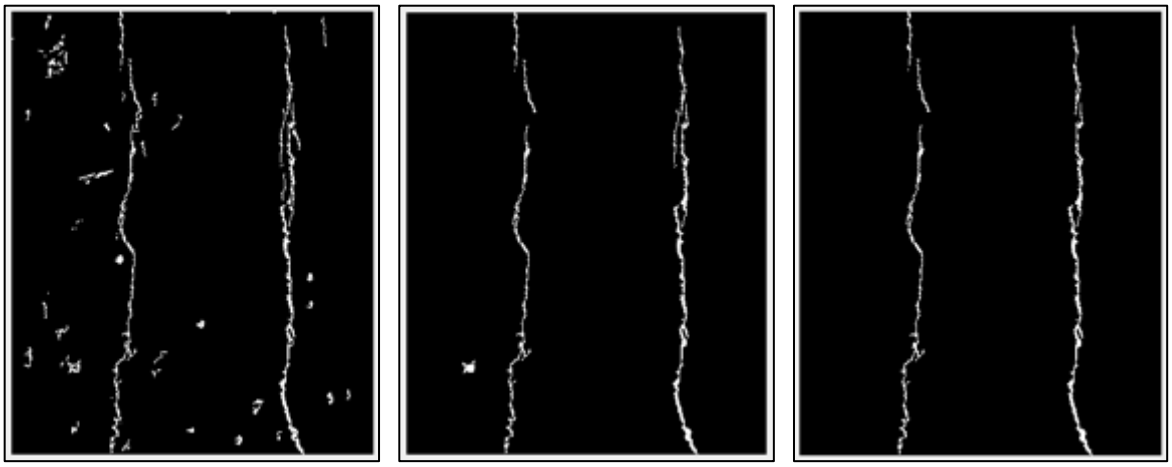

(a) (b) (c)

Figure 10 - Removing areas with less than P pixels

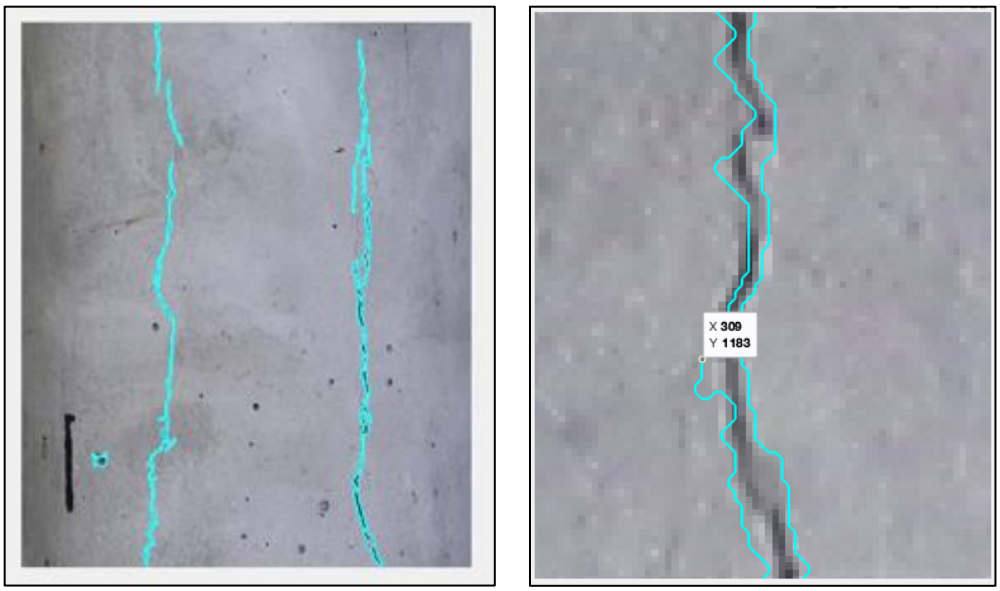

Figure 11 - Plotted boarders of all cracks

Figure 12 – Color coded surface cracks

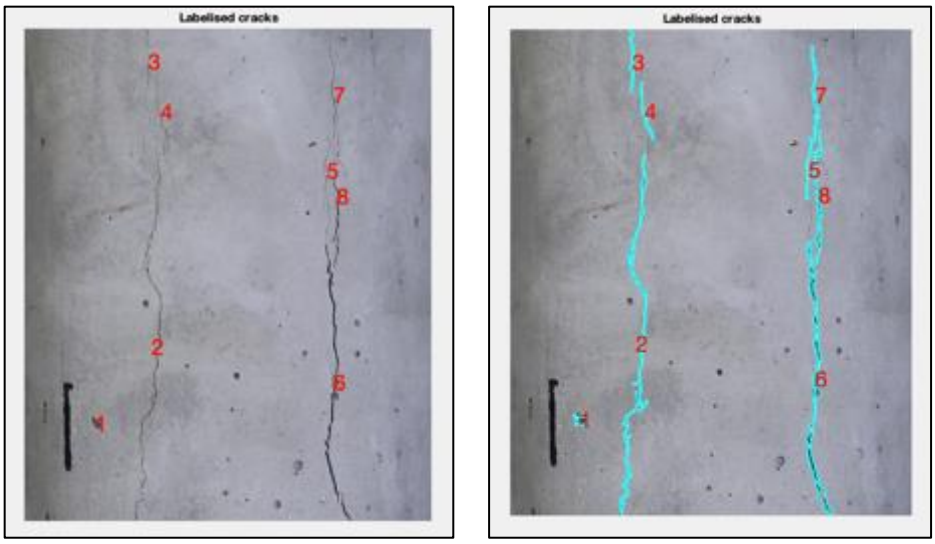

Figure 13 - Detected and labeled cracks

(a) (b) (c)

Figure 14 - Original image and surface cracks

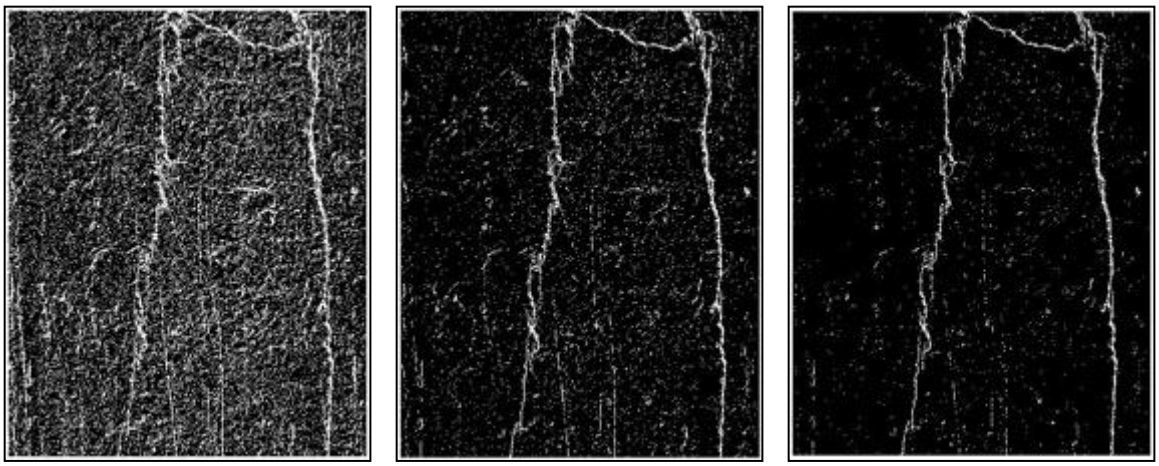

Figure 15 - Factors of 0.1, 0.2 and 0.3 applied to Otsu's value

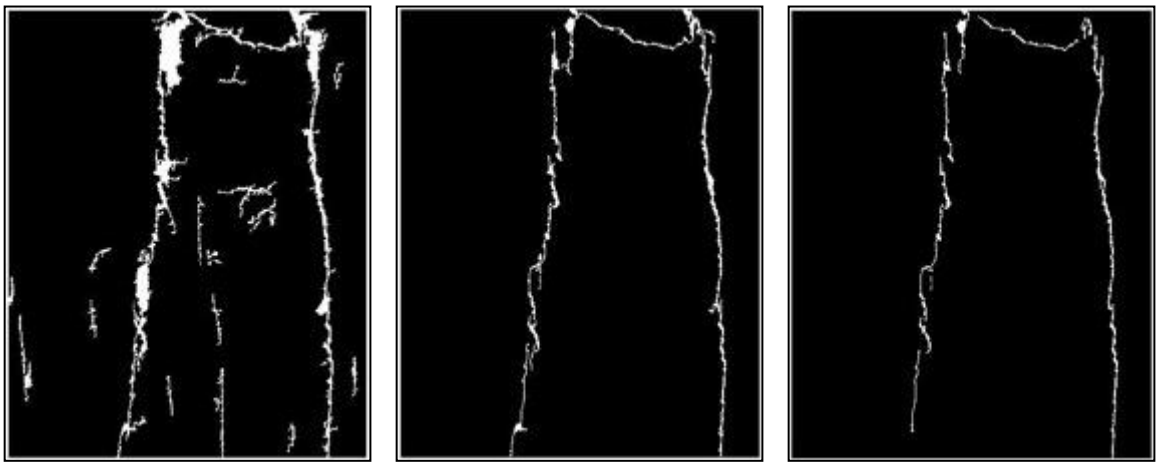

Figure 16 - Results obtained by applying the filters

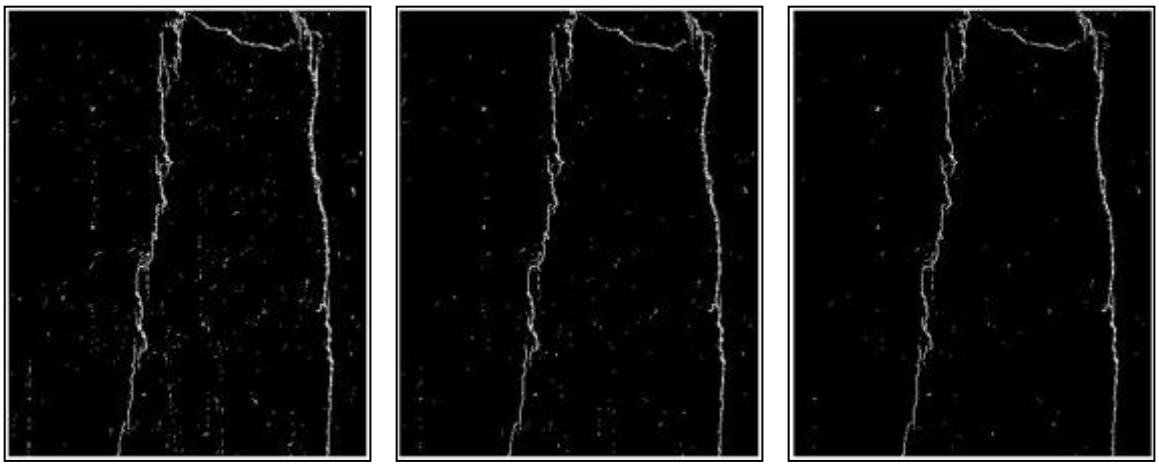

Figure 17 - Factors of 0.4, 0.5 and 0.6 applied to Otsu's value

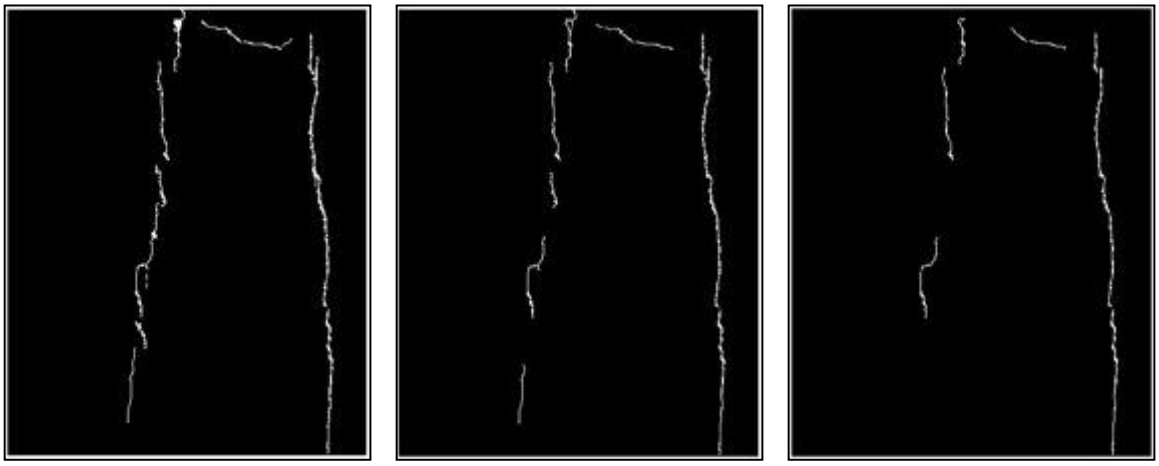

Figure 18 - Results obtained by applying the filters

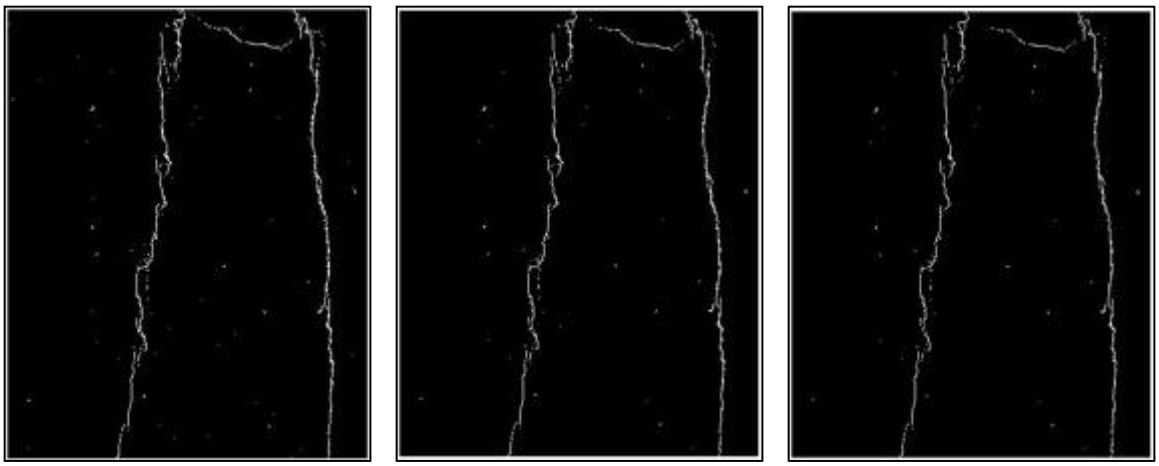

Figure 19 - Factors of 0.7, 0.8 and 0.9 applied to Otsu's value

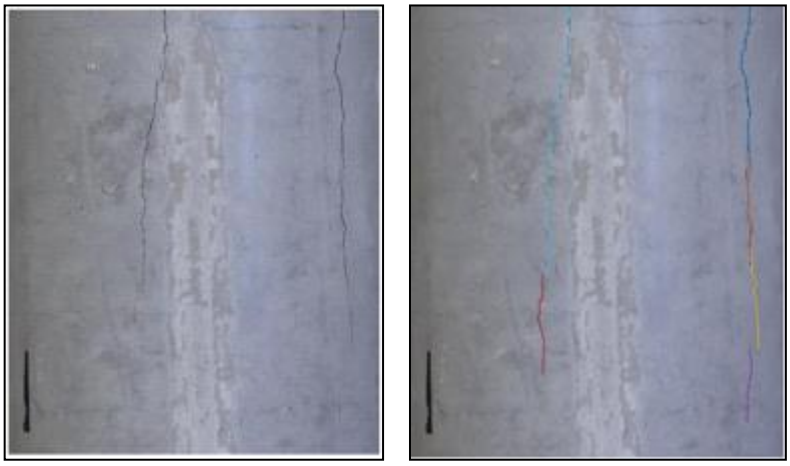

Figure 20 - Original image and surface cracks

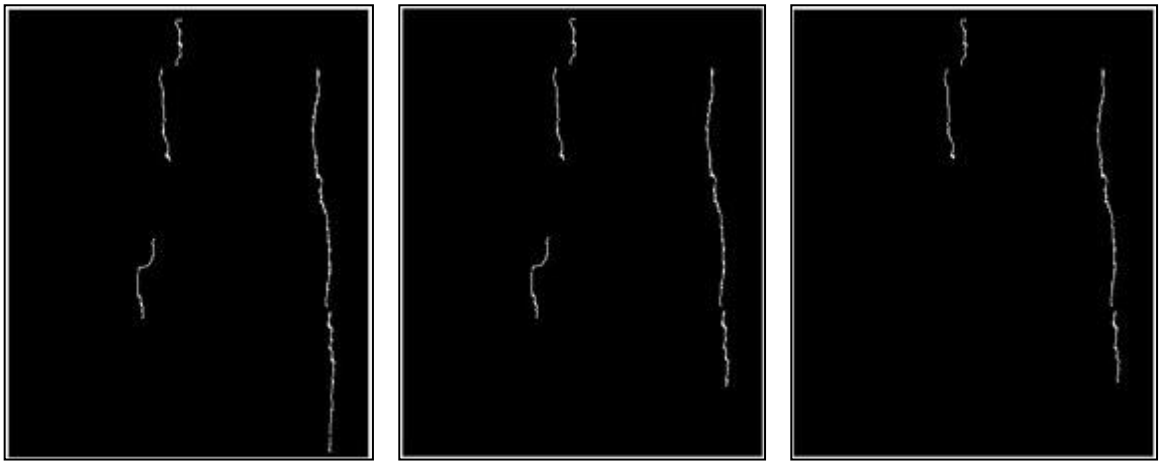

Figure 21 - Results obtained by applying the filters

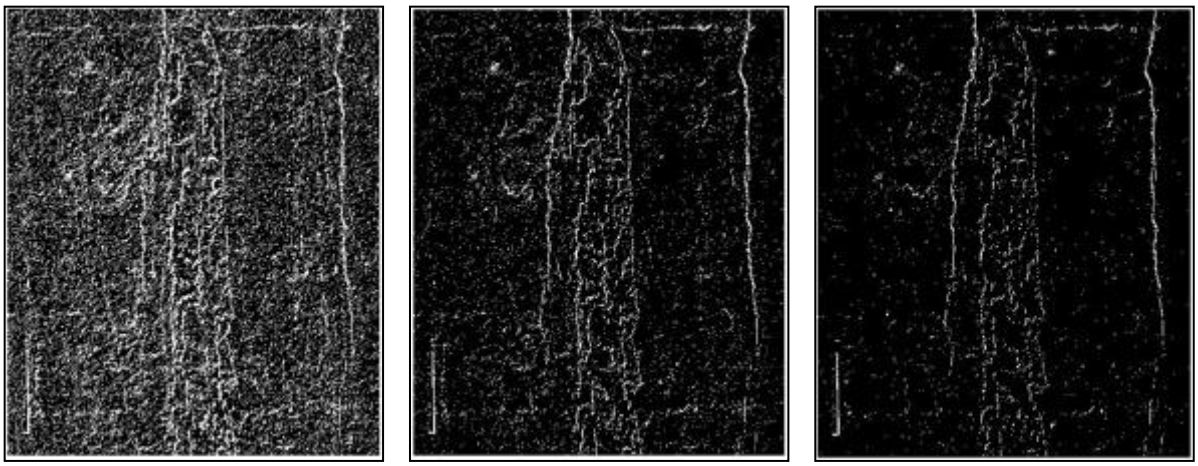

Figure 22 - Factors of 0.1, 0.2 and 0.3 applied to Otsu's value

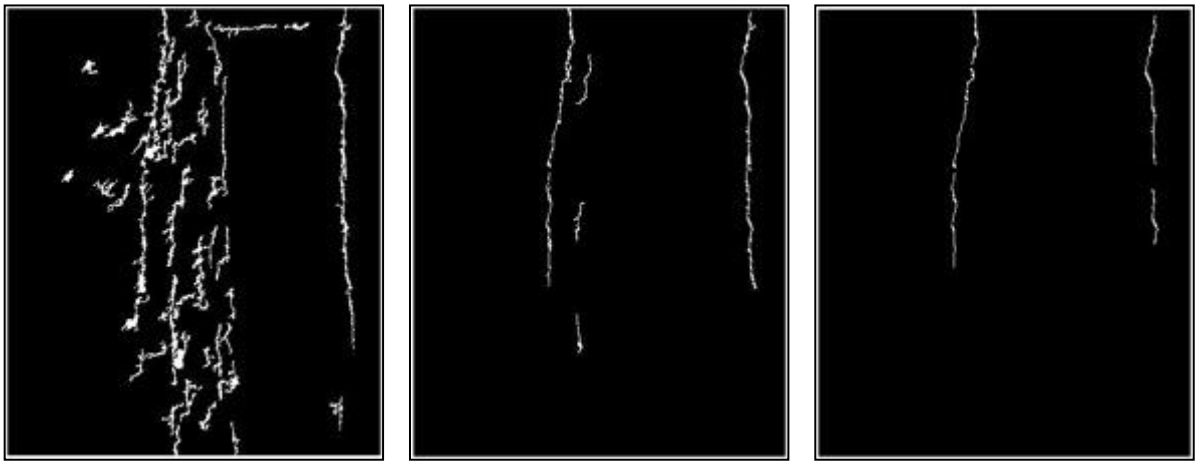

Figure 23 - Results obtained by applying the filters

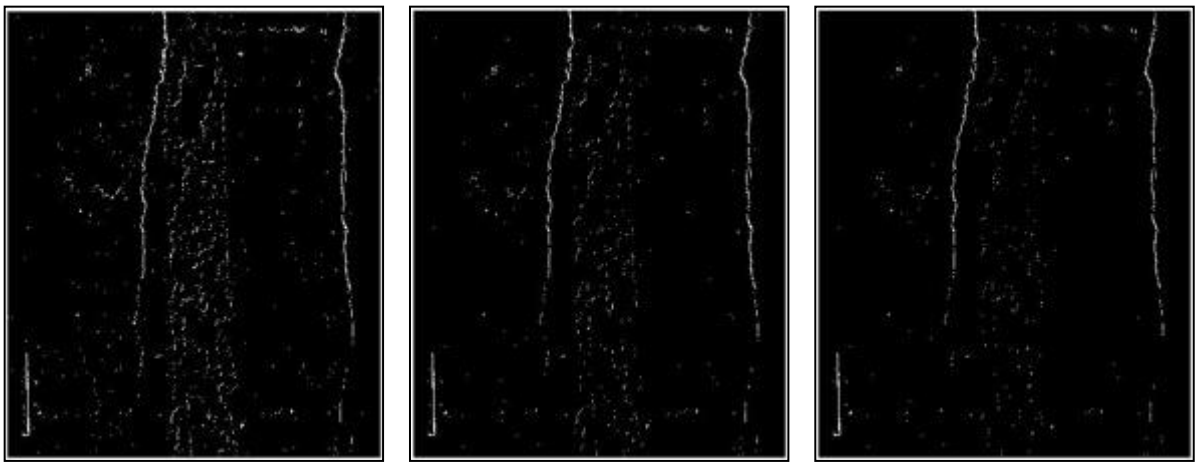

Figure 24 - Factors of 0.4, 0.5 and 0.6 applied to Otsu's value

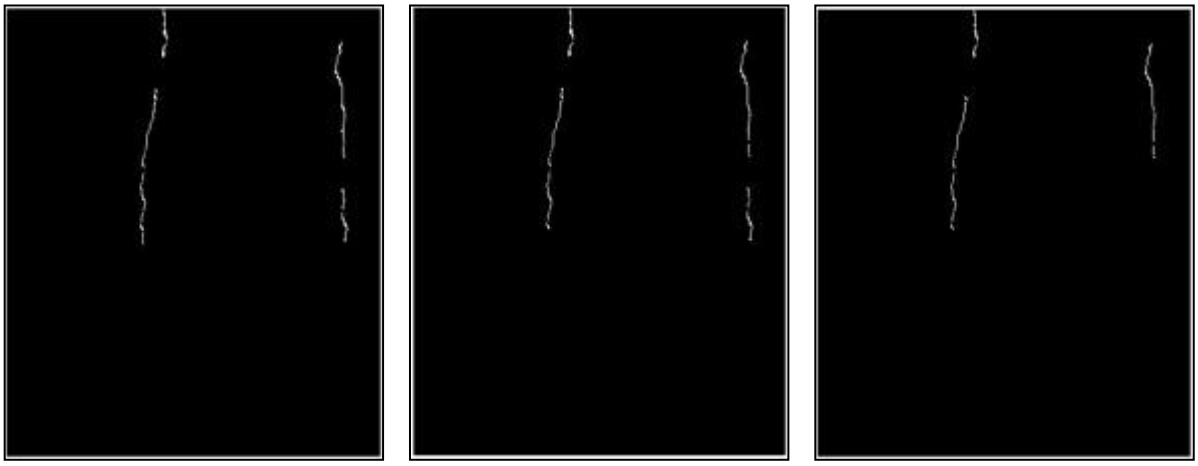

Figure 25 - Results obtained by applying the filters

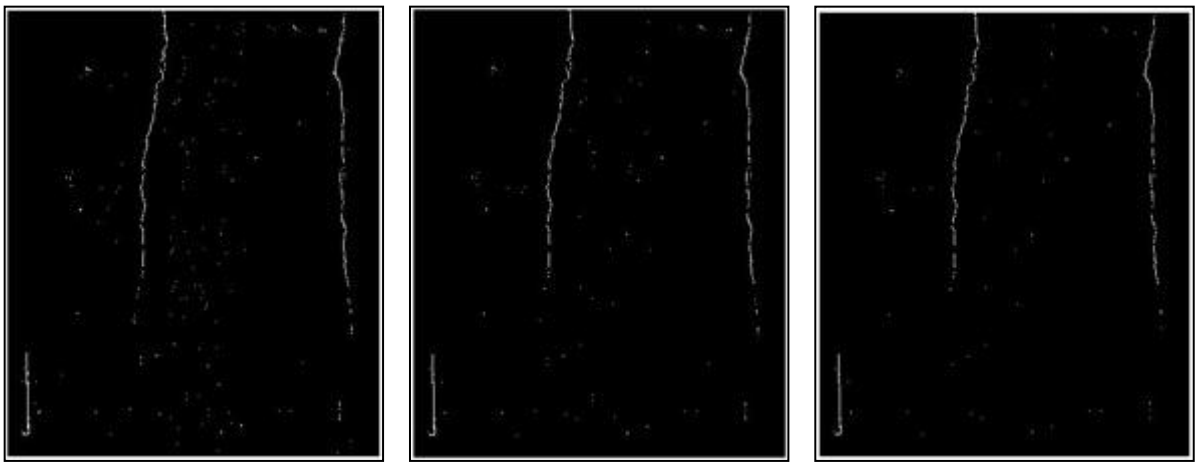

Figure 26 - Factors of 0.7, 0.8 and 0.9 applied to Otsu's value

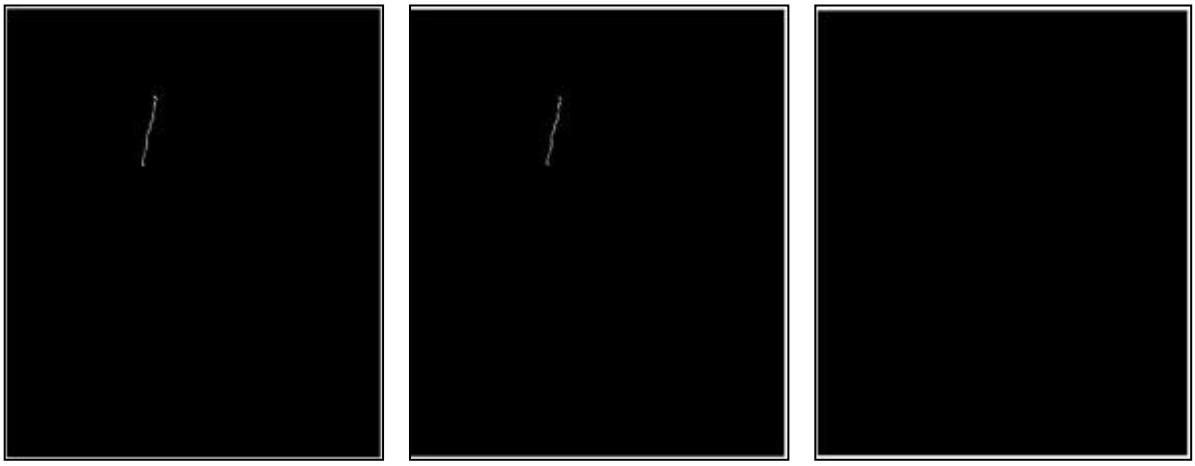

Figure 27 - Results obtained by applying the filters

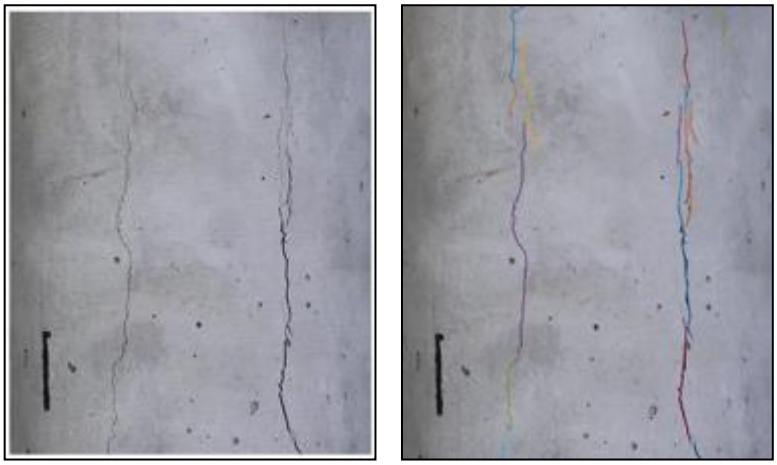

Figure 28 - Original image with surface cracks

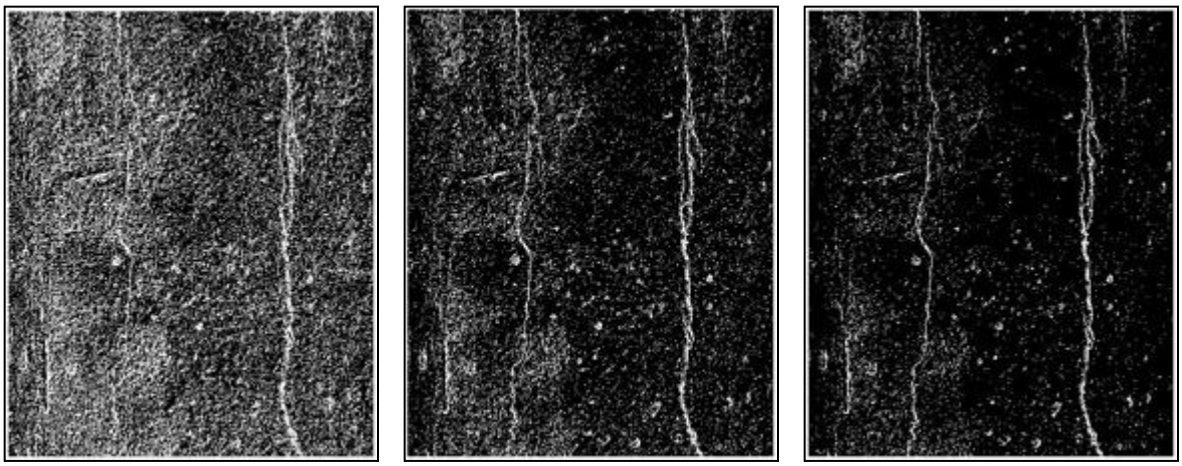

Figure 29 - Factors of 0.1, 0.2 and 0.3 applied to Otsu's value

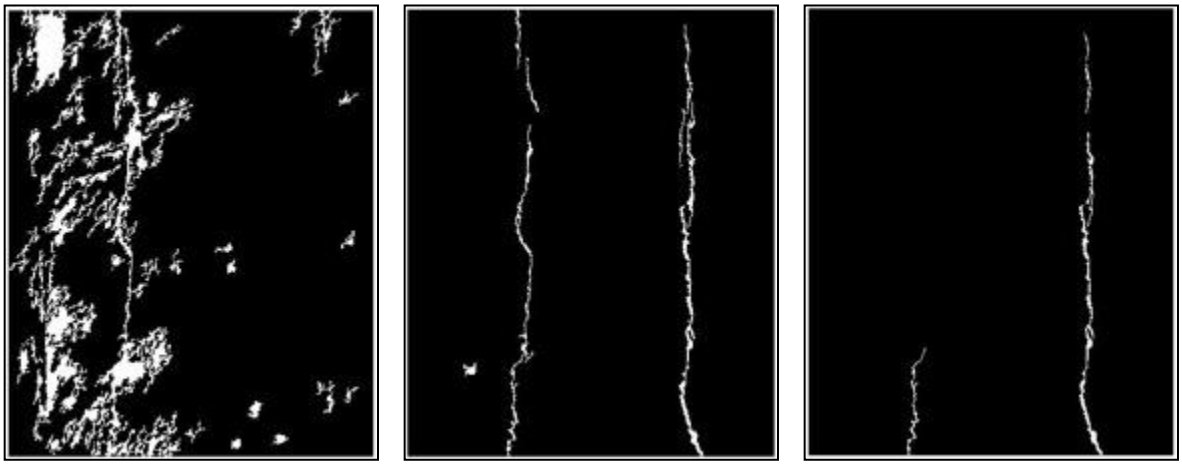

Figure 30 - Results obtained by applying the filters

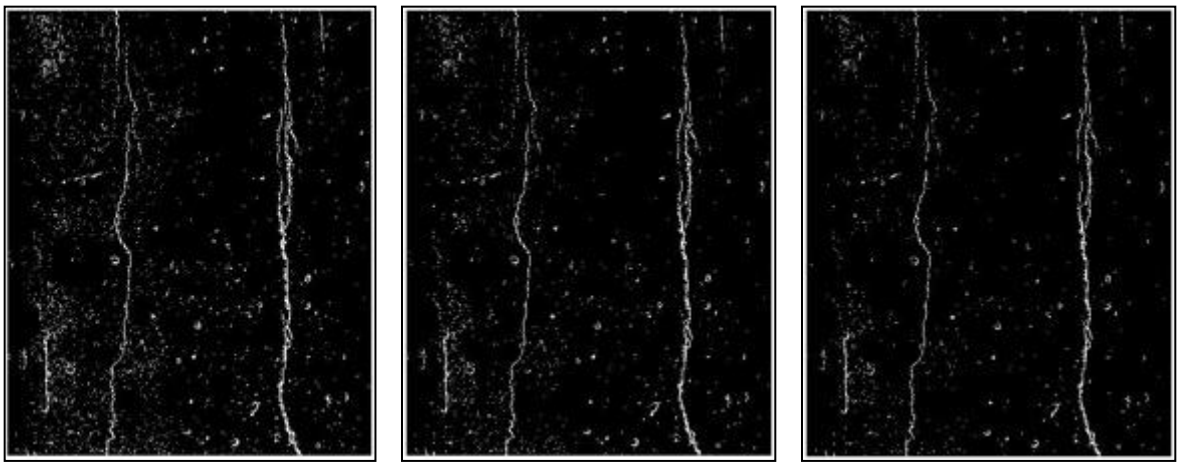

Figure 31 - Factors of 0.4, 0.5 and 0.6 applied to Otsu's value

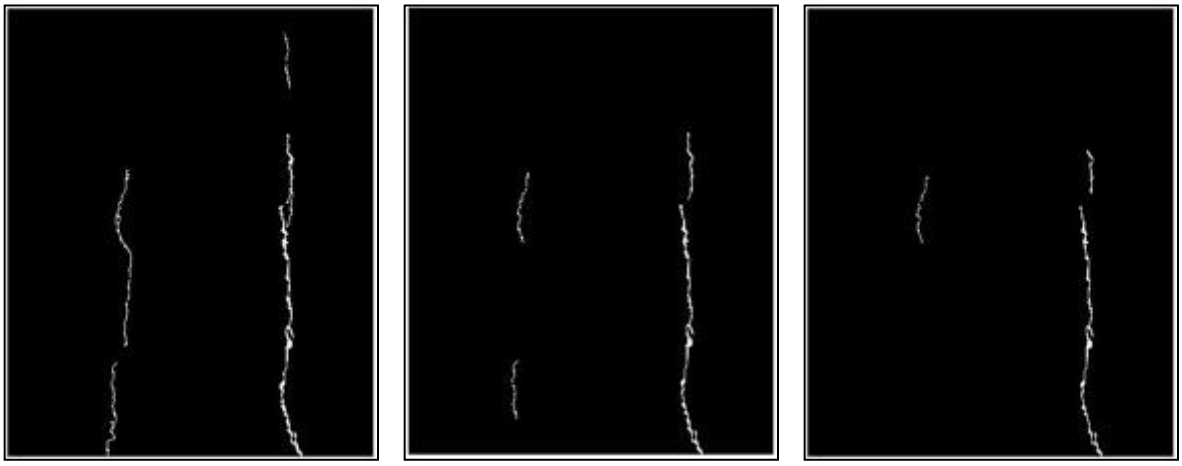

Figure 32 - Results obtained by applying the filters

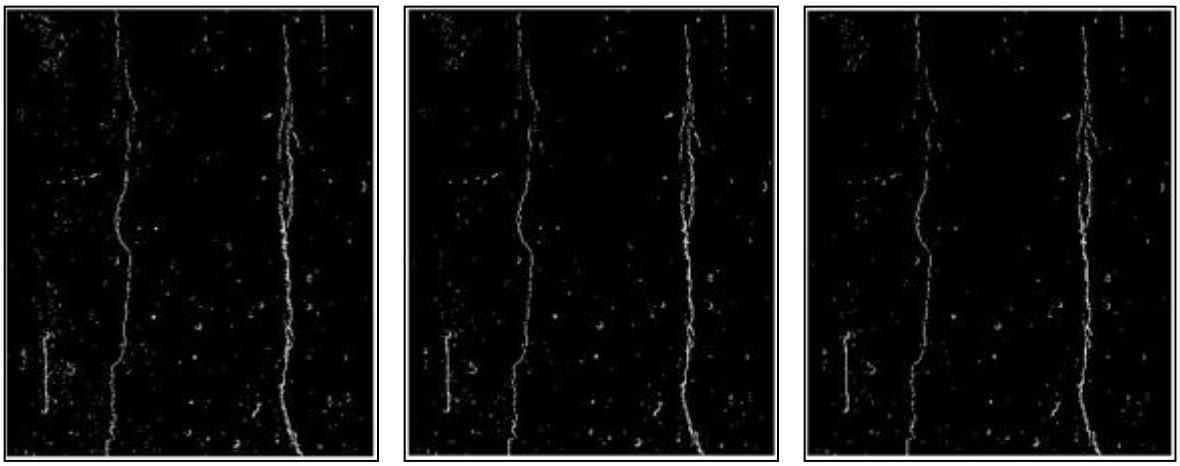

Figure 33 - Factors of 0.7, 0.8 and 0.9 applied to Otsu's value

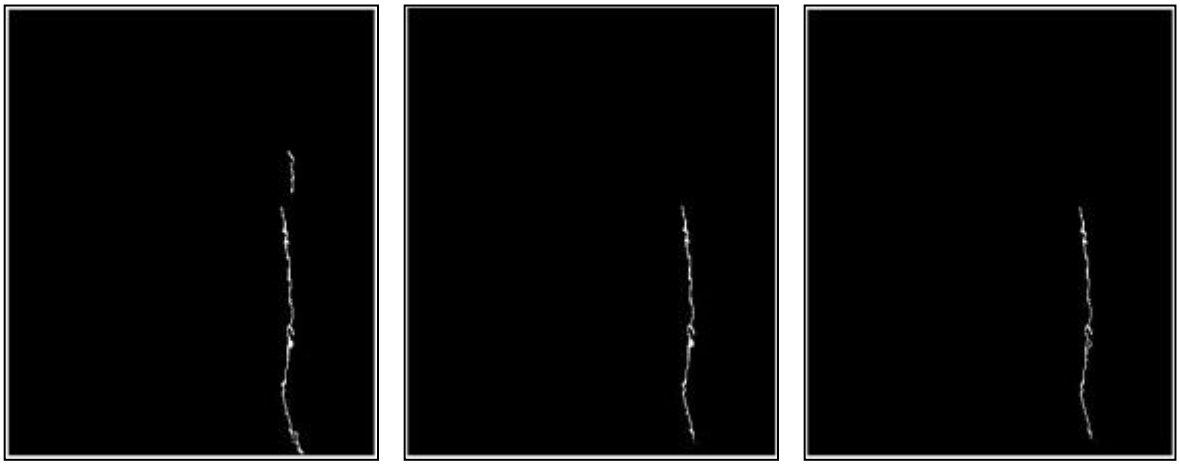

Figure 34 - Results obtained by applying the filters

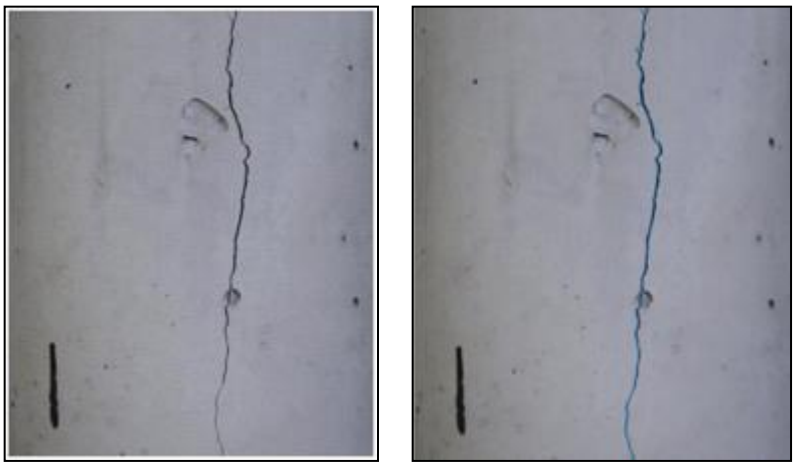

Figure 35 - Original image with surface cracks

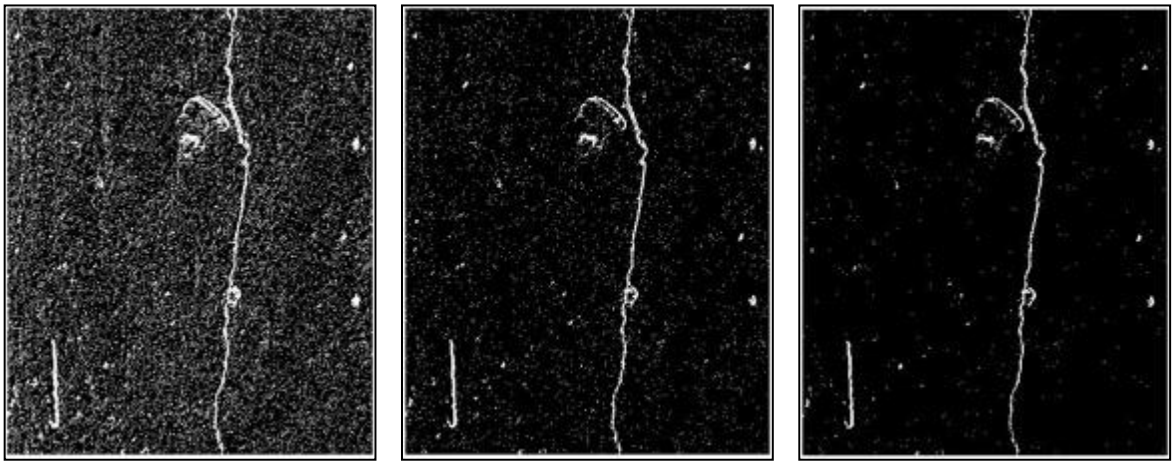

Figure 36 - Factors of 0.1, 0.2 and 0.3 applied to Otsu's value

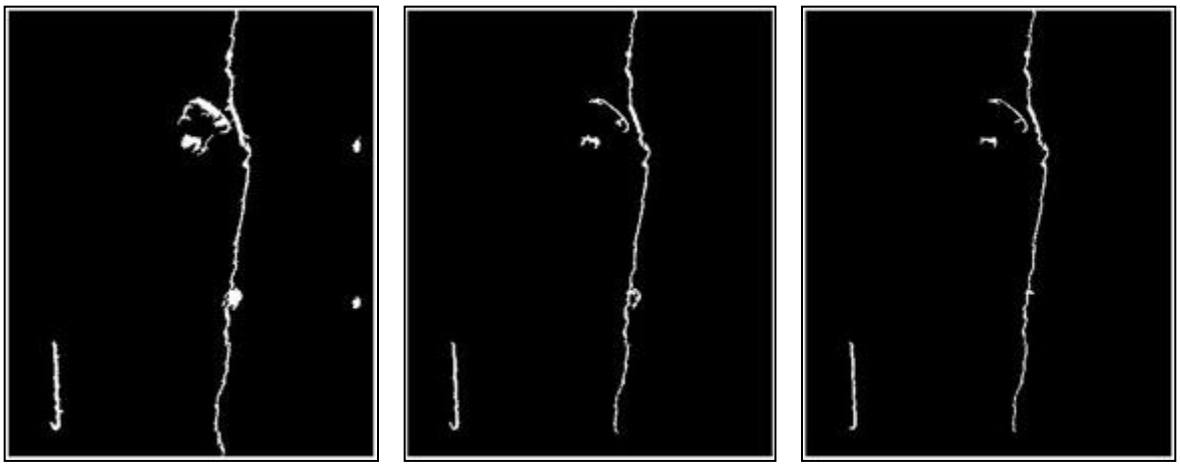

Figure 37 - Results obtained by applying the filters

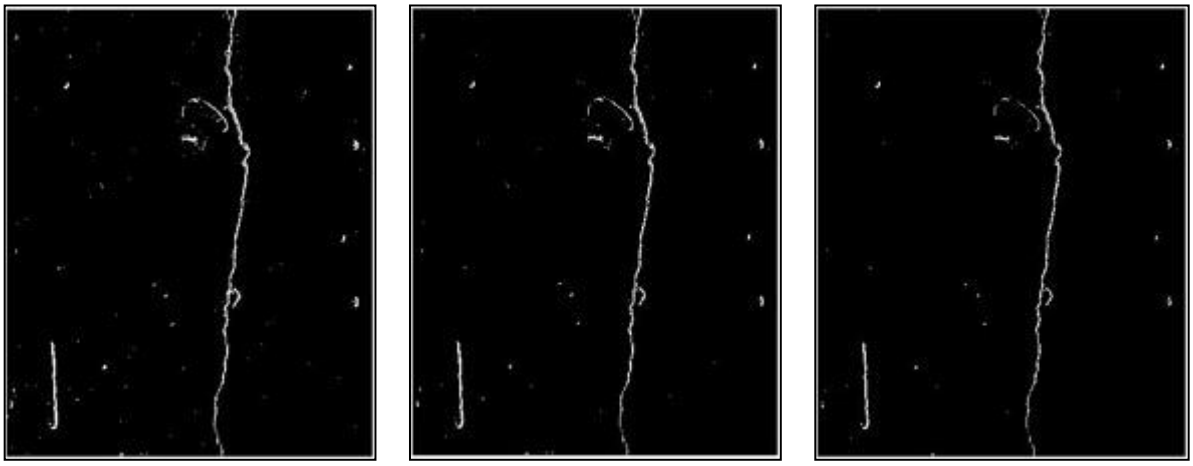

Figure 38 - Factors of 0.4, 0.5 and 0.6 applied to Otsu's value

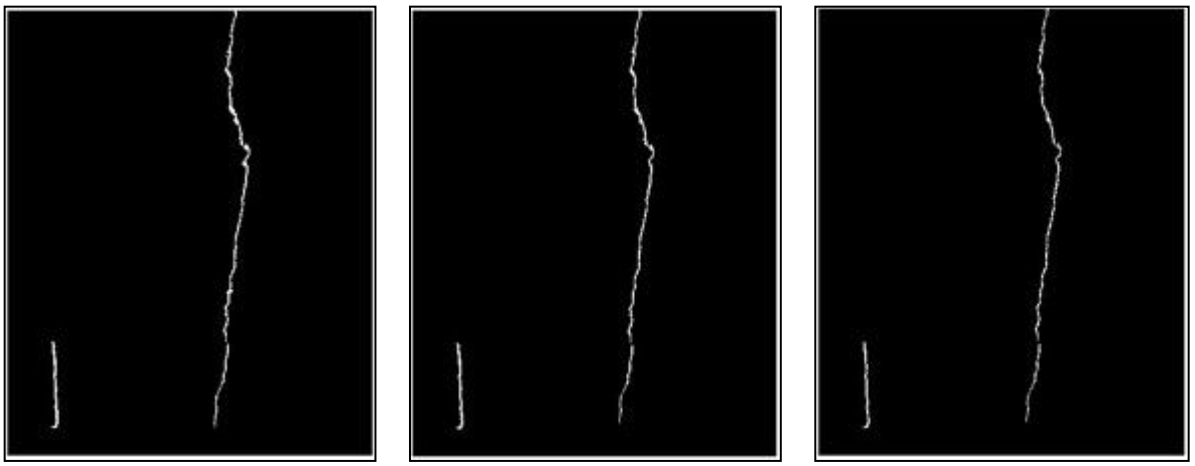

Figure 39 - Results obtained by applying the filters

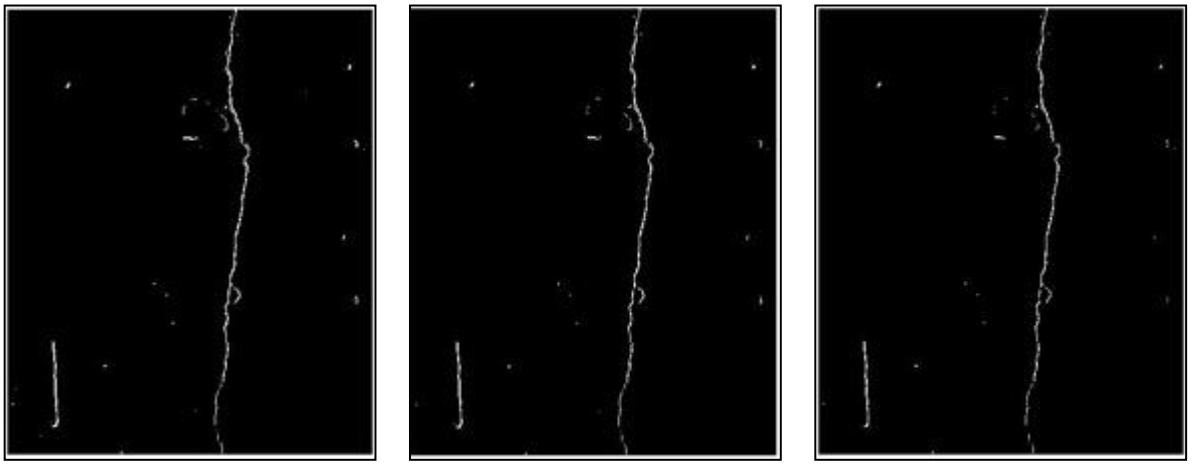

Figure 40 - Factors of 0.7, 0.8 and 0.9 applied to Otsu's value

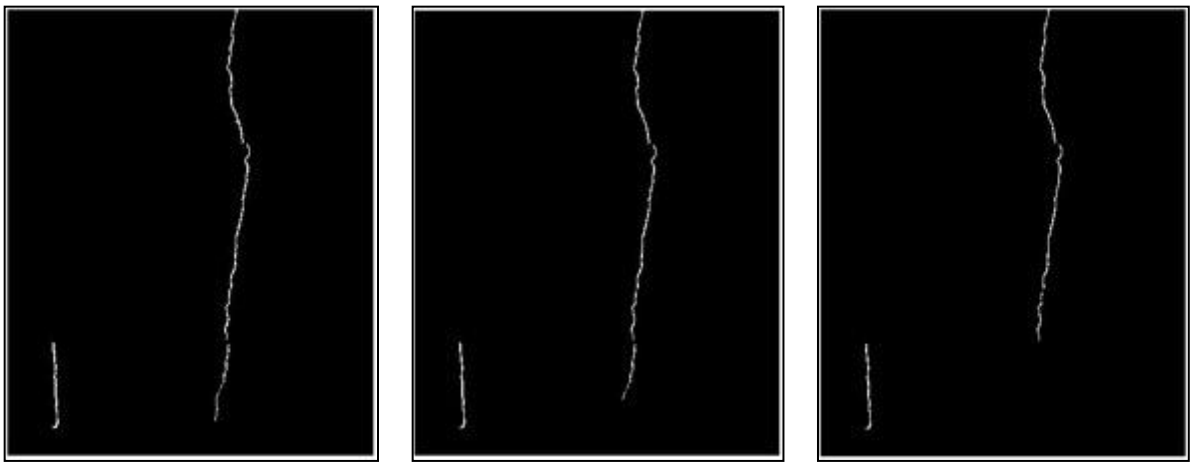

Figure 41 - Results obtained by applying the filters